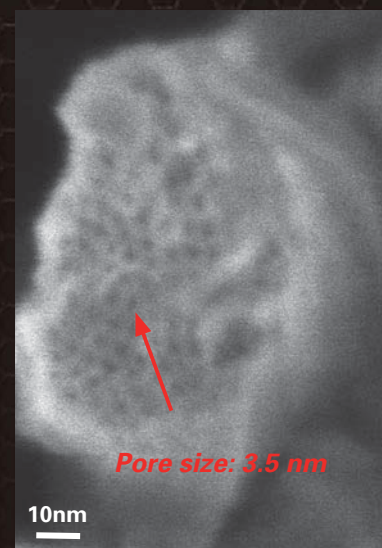
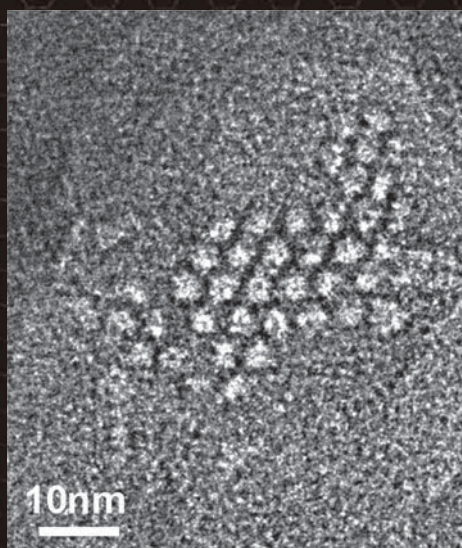
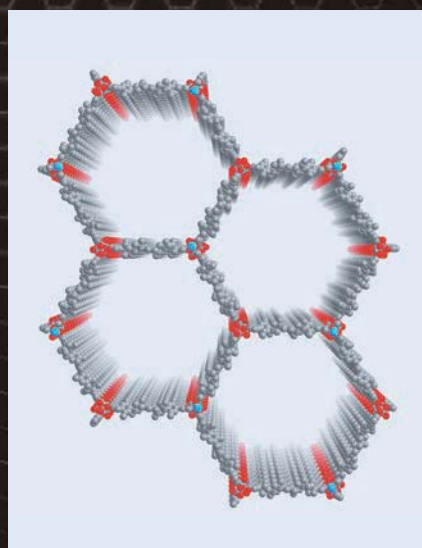


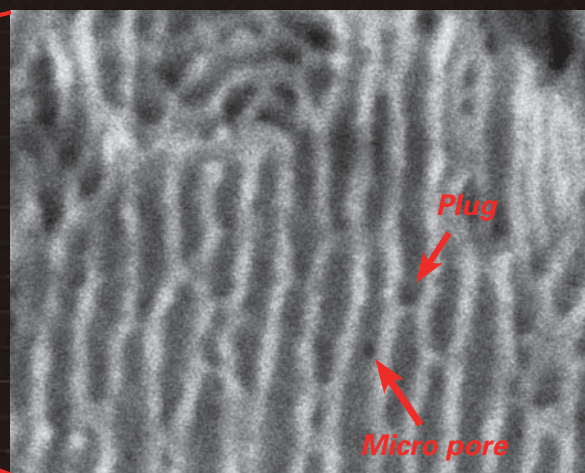
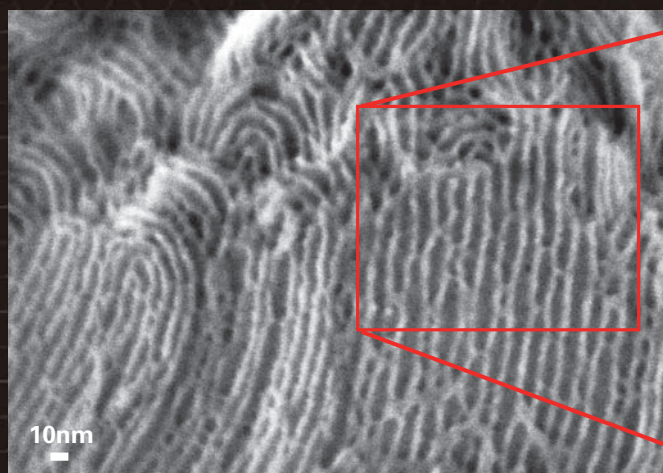
JEOL *news*

50 YEAR ANNIVERSARY

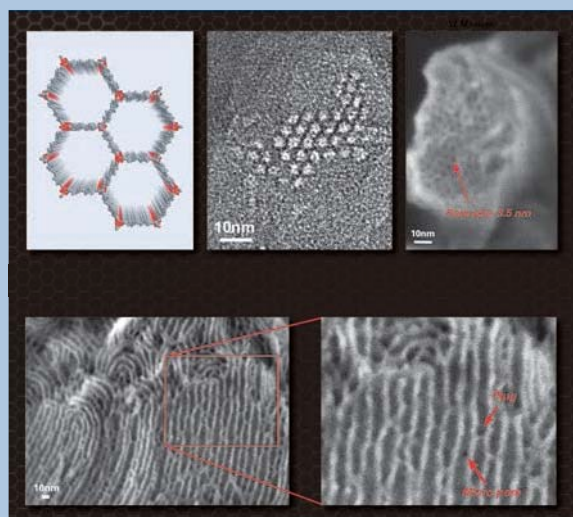
July 2013 Vol.48 No. 1



Novel Structural Characterisations of Insulating and Electron Beam Sensitive Materials Employing Low Voltage High Resolution Scanning Electron Microscopy



- Innovation in Structural Interpretation of Al-TM (Transition-metal) Decagonal Quasicrystals By Cs-corrected STEM 2
- Structural Analysis of Nanoparticles Using Scanning Transmission Electron Microscopy 11
- Novel Structural Characterisations of Insulating 21 and Electron Beam Sensitive Materials Employing Low Voltage High Resolution Scanning Electron Microscopy
- Effects of *l*-menthol on the Thermotropic Characteristics 32 of Intercellular Lipid in the Hairless Rat Stratum Corneum Evaluated by Differential Scanning Calorimetry and Electron Spin Resonance
- Introduction of New Products 39
- 50 Year Anniversary 42



Cover micrograph

On the top, from the left to the right, a schematic drawing of IRMOF-74, a HRTEM image taken by JEM-2010F equipped with a CEOS, and LVHRSEM image taken with JSM-7800F at 300 eV are shown. Metal organic frameworks (MOFs) have been known to be one of the most electron sensitive materials and therefore are difficult to be imaged with electron microscopy. Both TEM and SEM images taken from IRMOF-74 have given direct evidences that the channels are hexagonally arranged with a size of 3.5 nm and are opened to external surface, which are shown for the first time. The low-voltage high-resolution SEM (LVHRSEM) images in the bottom have been taken with JSM-7800F from silica mesoporous crystal SBA-15. The images clearly show existence of both plugs and micro pores within silica channel-walls of SBA-15.

Innovation in Structural Interpretation of Al-TM (Transition-metal) Decagonal Quasicrystals By Cs-corrected STEM

K. HIRAGA[†] and A. YASUHARA^{††}

[†] Institute for Materials Research, Tohoku University,
^{††} EM Application Group, EM Business Unit, JEOL Ltd.,

We give an overview of recent studies for structural interpretations of Al-TM (transition-metal) decagonal quasicrystals by Cs-corrected STEM with HAADF and ABF. Individual TM atoms and mixed sites (MSs) of Al and TM atoms are represented as separated bright dots in observed HAADF-STEM images, and so arrangements of TM atoms and MSs on two quasi-periodic planes of the decagonal quasicrystals can be directly determined. The derived structures are characterized as arrangements of TM atoms with a bond-orientational order (BOO), and consequently disprove previous cluster-based models characterized by BOO arrangements of large columnar clusters. In observed ABF-STEM images, Al atoms in addition to TM atoms and MSs are represented as dark dots, and the structures of well-symmetric regions can be determined. It can be concluded that Cs-corrected STEM gives us innovative interpretation for the structures of decagonal quasicrystals.

Introduction

Many kinds of decagonal quasicrystals have been found in Al-TM alloys represented by Al-Co-Ni, and their structures have been systematically investigated by HRTEM and HAADF-STEM observations [1-3]. Particularly, HAADF-STEM observations with the incident beam parallel to the periodic axis of the decagonal quasicrystals have proposed the existence of columnar atom clusters having a decagonal section with 2 nm in diameter and their two-dimensional quasiperiodic arrangements with a bond-orientational order (BOO), which is one of structural features in quasicrystals [2-4]. The decagonal atom clusters projected along the columnar axis have mainly pentagonal symmetry, and consequently there are two types of atom clusters with opposite directions in pentagonal symmetry. Therefore, the structures of Al-TM decagonal quasicrystals can be divided into two classes formed by one kind of atom clusters with the same direction and by two kinds of ones with opposite directions. The decagonal quasicrystals formed by one kind of atom clusters have pentagonal symmetry, and so they are often called pentagonal quasicrystals. On the other hand, the decagonal quasicrystals with the two kinds

of atom clusters show ordered arrangements of the two kinds of clusters and their structures are interpreted as CsCl- and NaCl-type ordered ones in body-centered and face-centered hyper-cubic lattices, respectively, in a higher-dimensional space [3].

Recent Cs-corrected STEM has a sufficient resolution to represent individual TM atoms as separated bright dots in observed images of decagonal quasicrystals, and so enables us to perform direct determination of arrangements of TM atoms [5-7]. However, previous studies by Cs-corrected STEM have discussed only the structures of the 2 nm atom clusters and have never touched on arrangements of TM atoms in full regions including atom clusters and glue areas between them [5-7]. Recently, we have extensively reexamined the structures of Al-TM decagonal quasicrystals and their crystalline approximants by Cs-corrected STEM, and proposed new structure models characterized by BOO arrangements of TM atoms [8-12], instead of the previous cluster-based models that have been widely accepted for a long time. In the present paper, we give an overview of recent examinations with three representative Al-Co-Ni decagonal quasicrystals in $\text{Al}_{71.5}\text{Co}_{25.5}\text{Ni}_3$ [8], $\text{Al}_{71}\text{Co}_{14.5}\text{Ni}_{14.5}$ [11] and $\text{Al}_{72}\text{Co}_8\text{Ni}_{20}$ [12] alloys by Cs-corrected STEM observations with a microscope of JEOL JEM-ARM200F, and demonstrate the innovative interpretations by Cs-corrected STEM for the structures of decagonal quasicrystals.

2-1-1 katahira, Aoba-ku, Sendai, 980-8577, Japan

E-mail: hiraga@imr.tohoku.ac.jp

Comparison between ordinary and Cs-corrected HAADF-STEM images of a decagonal quasicrystal

Figure 1(a) is an HAADF image of an $\text{Al}_{71.5}\text{Co}_{25.5}\text{Ni}_3$ decagonal quasicrystal, which was taken by an ordinary STEM (JEOL JEM-2010F). This decagonal quasicrystal is referred as to a pentagonal superstructure [1] and its structure has been characterized by a rhombic tiling of one kind of atom clusters with the same direction of pentagonal symmetry [2, 3]. In the image of Fig. 1(a), one can see atom clusters, formed by ten bright dots surrounding a pentagonal arrangement of bright dots, indicated by a circle, and that they are arranged with rhombic tiling with an edge-length of 2 nm. This type of HAADF-STEM images has been interpreted by the cluster-based model, in which decagonal atom clusters with 2 nm in diameter are connected by edge-shearing and arranged with rhombic tiling with an edge-length of 2 nm [2, 3].

Figure 1(b) is a Cs-corrected HAADF-STEM image of the same decagonal quasicrystal. One can easily recognize that the image of Fig. 1(b) provides a higher resolution, compared with Fig. 1(a), and shows bright dots separated with an interval of about 0.13 nm. The image clearly shows definite clusters formed by ten bright dots surrounding a pentagonal arrangement of bright dots, and no decagonal or no pentagonal symmetry for an arrangement of bright dots in a concentric circle outside the cluster, as can be seen from an arrangement of two bright dots and single ones, indicated by pairs of arrows and single ones, respectively. That is, the arrangement of bright

dots in the HAADF-STEM image shows no existence of 2 nm atom clusters with pentagonal symmetry. The cluster formed by ten bright dots surrounding a pentagonal distribution of bright dots is observed as a common structure unit in most of Al-TM decagonal quasicrystals, and so is called hereafter an 1.2 nm cluster, because of having a diameter of $1.2 (=2/\tau)$ nm.

Cs-corrected HAADF-STEM of W-(AlCoNi) crystalline approximant

Before we started the study of Al-TM decagonal quasicrystals, we observed HAADF-STEM images of crystalline approximants of W-(AlCoNi) and $\tau^2\text{-Al}_3\text{Co}$ [8, 9], which are considered to be important approximants having similar local structures to those of the Al-TM decagonal quasicrystals. **Figures 2 (a)** and **2 (b)** show arrangements of TM atoms, and mixed sites (MSs) of TM and Al atoms on A and B planes, respectively, in the W-(AlCoNi) structure, which was determined by single-crystal X-ray analysis [13]. The structure of the W-(AlCoNi) approximant has a stacking of ABA'B along the *b*-axis. Almost of TM atoms on the A and A' planes have the same arrangement, except for TM atoms indicated by red and green circles, which are on the A and A' planes, respectively, in deformed hexagonal tiles. It should be noticed here that an arrangement of TM atoms of red and green circles has a phason flip relation, as indicated by red and green lines. All TM atoms and MSs in the structure are exactly located at lattice points of a Penrose lattice with an edge-length of 0.25 nm, which is drawn by thin dashed lines in Figs. 2(a) and 2(b), and form

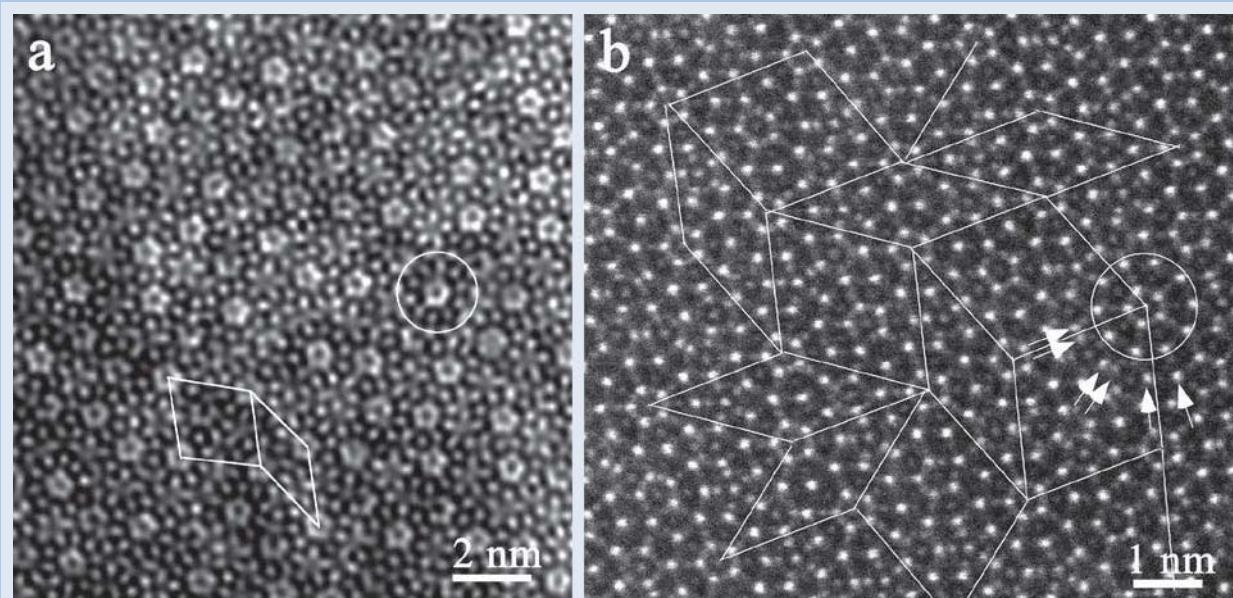


Fig. 1 Ordinary (a) and Cs-corrected (b) HAADF-STEM images of an $\text{Al}_{71.5}\text{Co}_{25.5}\text{Ni}_3$ decagonal quasicrystal, taken with the incident beam parallel to the periodic axis. Note clusters formed by ten bright dots surrounding a pentagonal distribution of bright dots and their arrangements by rhombic tiling with an edge-length of 2 nm. However, one can see no decagonal or no pentagonal symmetry for an arrangement of bright dots in a concentric circle outside the cluster, as can be seen from an arrangement of two bright dots and single ones, indicated by pairs of arrows and single ones, respectively.

pentagonal lattices with edge-lengths of 0.47 nm on the A plane and 0.76 ($=\tau \cdot 0.47$) nm on the B plane. On the other hand, Al atoms in the W-(AlCoNi) structure are known to shift from lattice points of a Penrose lattice, and are located at stable positions in the definite arrangements of TM atoms and MSs [13]. The result shows that the structures of decagonal quasicrystals should be characterized by BOO arrangements of TM atoms and MSs.

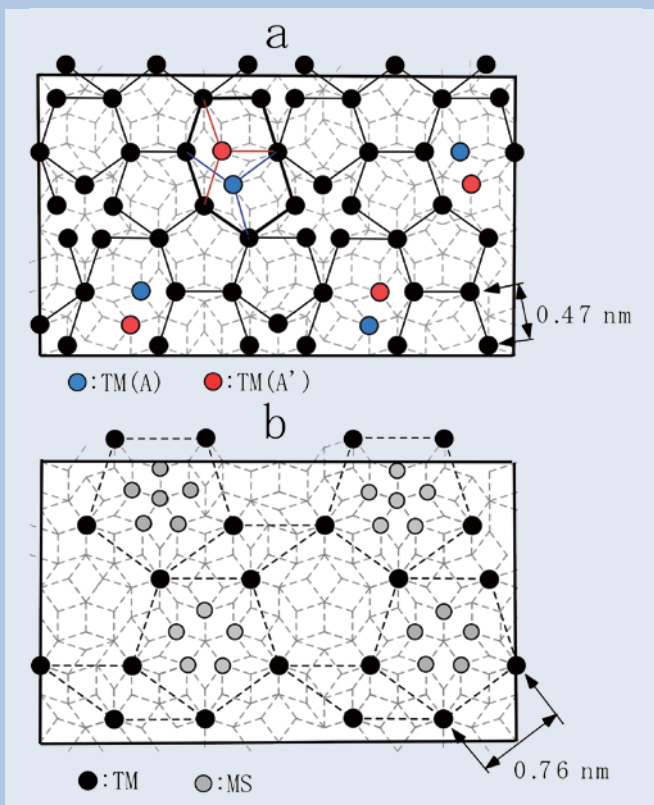
Figure 3 shows HAADF-STEM images of the W-(AlCoNi) approximant, taken with the incident beam parallel to the *b*-axis. In Fig. 3(a), one can see that the 1.2 nm clusters with the same direction of pentagonal symmetry, indicated by a white circle, are arranged with thin rhombic tiling with an edge-length of 2 nm, as indicated by red lines. Almost of bright dots in the HAADF-STEM image can be connected by lines with lengths of 0.47 nm and 0.76 nm, which are indicated by white solid and dashed lines, respectively, as shown in Figs. 3(b) and 3(c). The bright dots at lattice points of pentagonal lattices with an edge-lengths of 0.47 nm and 0.76 nm correspond to TM atoms in the A and B planes of Figs. 2(a) and 2(b), respectively. The weak bright dots indicated by red and green circles in Fig. 3(b) correspond to the TM atoms of red and green circles in Fig. 2(a), and they have one atom in the projection of the unit cell, but the other TM positions have two atoms in the unit cell. Therefore, the bright dots indicated by red and green circles in Fig. 3(b) show weak intensity with $1/4$ brightness in the HAADF-STEM image forming Z^2 (Z =atomic number) contrast, compared with the other bright dots. If the TM atoms indicated by red and green circles are ignored, this structure can be described by arrangements of TM

atoms of two atomic planes of A and B. In Fig. 3(c), it should be noted that double pentagonal arrangements of bright dots, which are composed with pairs of bright dots along fivefold rotational directions, are always placed in downward pentagonal frames with edge-length of 0.76 nm. Outside five dots of the double pentagonal distribution correspond to TM atoms on the A plane, as can be seen in Fig. 3(d), and inner dots with relatively weak intensity show MSs in the B plane. Also, in upward pentagonal frames in Fig. 3(c), pentagonal distributions of bright dots corresponding to TM atoms on the A plane are always observed. The above characteristic distributions of bright dots in pentagonal frames with an edge-length of 0.76 nm are observed in most of HAADF-STEM images of Al-TM decagonal quasicrystals, as will be mentioned later. It should be noticed here that relatively strong dots at the centers of the double pentagonal distributions, indicated by a red arrow, correspond to MSs, and weak dots indicated by a blue arrow correspond to Al atoms in the B plane. In addition to bright dots corresponding to TM atoms and MSs, also, weak dots corresponding to Al atoms are faintly observed in the HAADF-STEM image.

The structures of three types of decagonal quasicrystals obtained by Cs-corrected STEM

Figures 4(a) and **4(b)** show enlarged HAADF-STEM images of a part of Fig. 1(b), including two fat and one thin rhombic frames of an edge-length of 2 nm. As the same as Fig. 3, bright dots in the images can

Fig. 2 Arrangements of TM atoms in the W-(AlCoNi) structure. TM atoms are arranged with pentagonal tiling of an edge-length of 0.47 nm on A (a) and 0.76 nm on B (b) planes, and pentagonal distributions of MSs are placed in downward pentagons with an edge-length of 0.76 nm in (b). All TM atoms and MSs are exactly located at lattice points of a Penrose lattice of 0.25 nm.



be connected by lines with lengths of 0.47 nm and 0.76 nm, as indicated by solid lines in Fig. 4(a) and dashed ones in Fig. 4(b), respectively, and also double pentagonal distributions and pentagonal ones of bright dots which are placed in all downward and upward pentagonal frames with an edge-length of 0.76 nm, respectively, are observed in Fig. 3(b). This feature is the same as that of W-(AlCoNi) approximant, as can be seen in Fig. 3(c). From the images of Figs. 4(a) and 4(b), arrangements of TM atoms and MSs in the A and B planes can be directly derived, as shown in Figs. 4(c) and 4(d), respectively. This quasicrystal has actually the structure of four atomic planes, and the four layer structure is considered to result from the atoms indicated by red and green circles in Fig. 4(a), which

are located on A and A' planes, from an analogy with the W-(AlCoNi) structure. It should be noticed that the difference between the structures of this decagonal quasicrystal and W-(AlCoNi) approximant results from only different pentagonal tiling of arrangements of TM atoms.

Figures 5(a) and 5(b) are HAADF-STEM images of an $\text{Al}_{71}\text{Co}_{14.5}\text{Ni}_{14.5}$ decagonal quasicrystal, which was referred as to type-I superstructure [1]. This decagonal quasicrystal has been characterized as an ordered arrangement of two kinds of columnar clusters with different orientations of decagonal symmetry [2, 3]. A fundamental lattice constructed by connecting the clusters is a rhombic lattice with an edge-length of 2 nm. The ordered arrangement of the two kinds of the clusters

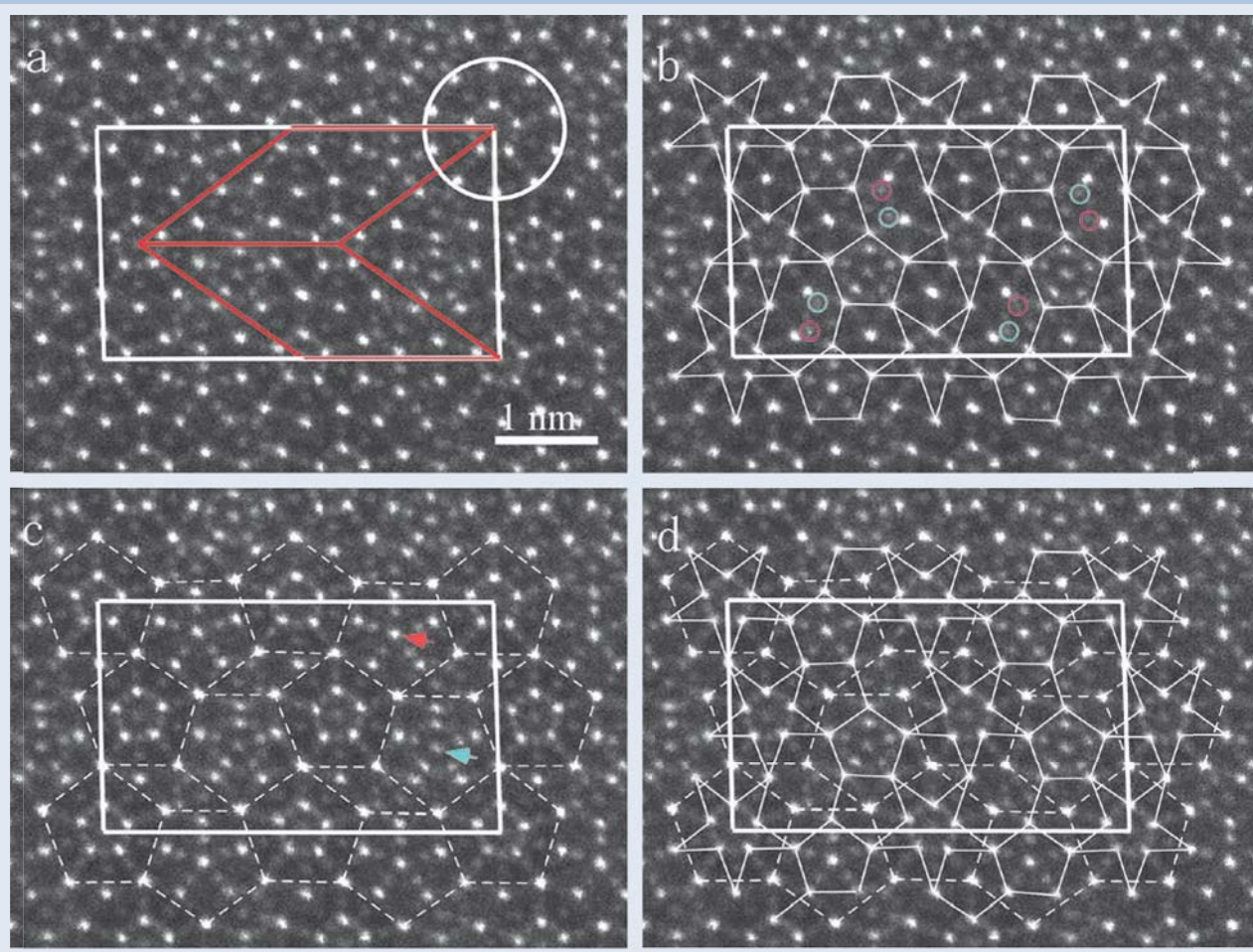


Fig. 3 HAADF-STEM images of the W-(AlCoNi) approximant, taken with the incident beam parallel to the *b*-axis. The 1.2 nm clusters formed by ten bright dots surrounding a pentagonal arrangement of bright dots are located at corners of thin rhombic frames with an edge-length of 2 nm, indicated by red lines in (a). Bright dots connected by lines with lengths of 0.47 nm in (b) and 0.76 nm in (c) correspond to TM atoms on the A and B planes of Fig. 2, respectively. Double pentagonal distributions of bright dots, which are composed with pairs of bright dots along fivefold rotational directions, are observed inside of downward pentagonal frames, and pentagonal arrangements of bright dots in upward pentagonal frames in (c). Outside five bright dots in the double pentagonal distribution correspond to TM atoms in the A plane, and inside five dots are MSs in the B plane, as can be seen in (d). Central dots indicated by a red arrow and weak dots indicated by a blue arrow correspond to MS and Al atom, respectively, as can be seen from Fig. 2. Deformed rectangles of the unit cell result from the sample drift during beam scanning.

has been interpreted by a NaCl-type face-centered hypercubic lattice in a five-dimensional space [2, 3]. In the images, one can see two kinds of 1.2 nm clusters with different orientations of central pentagonal arrangements of bright dots, as indicated by solid and dashed circles in Fig. 5(b). Two clusters connected by bonds of a length of 2 nm always have different orientations of central pentagons. Most of bright dots in the HAADF-STEM images can be connected by lines with a length of 0.76 nm, as shown in Figs. 5(a) and 5(b). The structure of this decagonal quasicrystal is formed by two planes of A and B stacking along the periodic axis [2], and so the bright dots connected by the solid lines in Figs. 5(a) and 5(b) lines correspond to TM atoms on the A and B planes, respectively. In Figs. 5(a)

and 5(b), one can see double pentagonal distributions of bright dots in rightward pentagonal frames in Fig. 5(a) and leftward ones in Fig. 5(b), whereas in the leftward pentagonal frames in Fig. 5(a) and rightward ones in Fig. 5(b), pentagonal distributions of bright dots are observed. The above characteristic feature is similar to those of Fig. 3(c) and 4(b). Outside five dots of the double pentagonal distribution correspond to TM atoms and/or MSs on a different plane from the tiling plane, and inside five dots correspond to MSs on the tiling plane. From the observed HAADF-STEM images of Figs. 5(a) and 5(b), arrangements of TM atoms and MSs on the A and B planes can be directly determined, as shown in Figs. 5(c) and 5(d).

From the structures of $\text{Al}_{71.5}\text{Co}_{25.5}\text{Ni}_3$ and

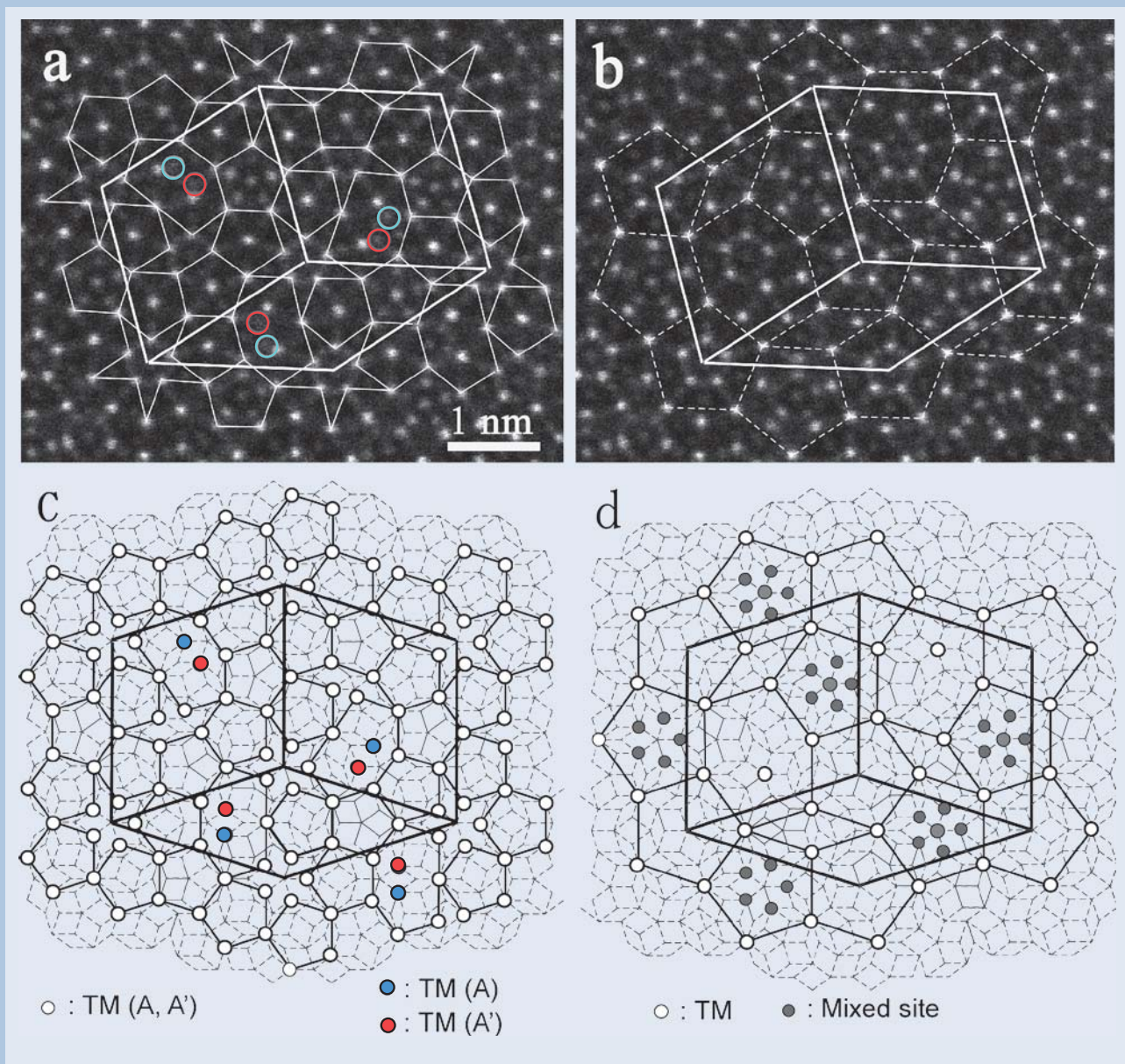


Fig. 4 HAADF-STEM images (a, b) of an $\text{Al}_{71.5}\text{Co}_{25.5}\text{Ni}_3$ decagonal quasicrystal and arrangements of TM atoms (c, d) on the A and B planes, which were derived from arrangements of bright dots in (a) and (c). Most of bright dots in the image can be connected by lines with lengths of 0.47 nm and 0.76 nm, as shown in (a) and (b). Note double pentagonal distributions of bright dots in downward pentagonal frames and pentagonal arrangements of bright dots in upward ones in (b).

$\text{Al}_{71}\text{Co}_{14.5}\text{Ni}_{14.5}$ decagonal quasicrystals, it can be concluded that the arrangements of TM atoms in decagonal quasicrystals formed by BOO arrangements of one kind of 1.2 nm clusters are characterized as two planes with different tilings of lengths of 0.47 nm and 0.76 nm, whereas those in decagonal quasicrystals with arrangement of two kinds of the clusters have two planes with pentagonal tilings of the same length of 0.76 nm. Therefore, the former has different atomic density in the A and B planes, and the latter has the same atomic density in the both planes. This difference can be easily noticed in diffraction patterns taken with the incident beam perpendicular to the periodic

axis. That is, diffraction spots resulting from different atom density of A and B planes appear in decagonal quasicrystals formed by one kind of atom clusters, and the diffraction spots are absent in diffraction patterns of decagonal quasicrystals with two kinds of clusters [2].

Figures 6(a) and 6(b) are HAADF-STEM images of an $\text{Al}_{72}\text{Co}_8\text{Ni}_{20}$ decagonal quasicrystal. This decagonal quasicrystal referred as to Ni-rich basic structure [1] is known to be one of highly ordered quasicrystals, and so has been extensively studied. In a previous paper, the existence of large columnar atom clusters with 3.2 ($=2 \cdot \tau$) nm in diameter has been proposed from HAADF-STEM observations [14],

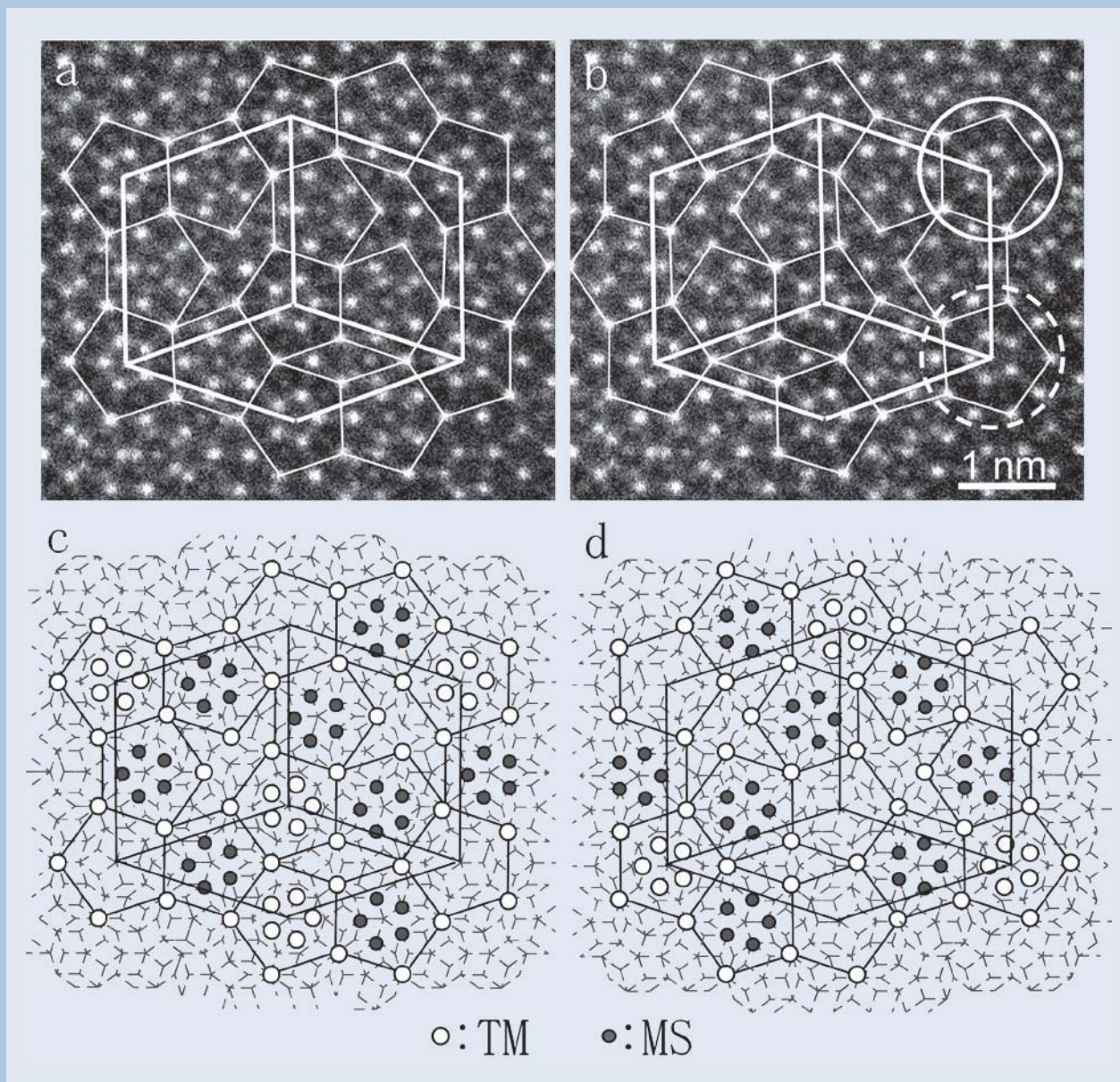


Fig. 5 HAADF-STEM images (a, b) of an $\text{Al}_{71.5}\text{Co}_{14.5}\text{Ni}_{14.5}$ decagonal quasicrystal and arrangements of TM atoms (c, d) on the A and B planes, derived from arrangements of bright dots in (a) and (b). In (b), two kinds of 1.2 nm clusters, indicated by circles of solid and dashed lines, are located at lattice points of rhombic tiling with an edge-length of 2 nm. Most of bright dots in the image can be connected by lines with a length of 0.76 nm, as shown in (a) and (b). Note double pentagonal distributions of bright dots inside of rightward pentagonal frames in (a) and leftward ones in (b), and pentagonal arrangements of bright dots inside of leftward pentagons in (a) and rightward ones in (b).

but other studies of the same decagonal quasicrystal have never touched on the 3.2 nm cluster [15-18]. Therefore, we reexamined the $\text{Al}_{72}\text{Co}_8\text{Ni}_{20}$ decagonal quasicrystal by full use of Cs-corrected STEM with HAADF and ABF techniques [12].

Most of bright dots in the HAADF-STEM images of the $\text{Al}_{72}\text{Co}_8\text{Ni}_{20}$ decagonal quasicrystal can be connected by lines with a length of 0.76 nm, as shown in Figs. 6(a) and 6(b). The structure of this decagonal quasicrystal is formed by two quasiperiodic planes of A and B stacking along the periodic axis [2], and so the bright dots connected by the solid and dashed lines in Figs. 6(a) and 6(b) correspond to TM atoms on

the A and B planes, respectively, in Figs. 6(c) and 6(d), which were derived from the arrangements of bright dots in Figs. 6(a) and 6(b). Also, double pentagonal distributions are observed in rightward pentagonal frames in Figs. 6(a) and in leftward ones in Fig. 6(b), as the similarity to Figs. 3(c), 4(b) and 5(a, b), whereas in leftward pentagons in Fig. 6(a) and rightward ones in Fig. 6(b), a variety of distributions of bright dots, e. g. pentagonal, decagonal and asymmetric distributions of bright dots are observed. Most of bright dots in the variety of distributions can be interpreted by pentagonal frames of an edge-length of 0.47 nm, as indicated by red lines in Figs. 6(c) and 6(d).

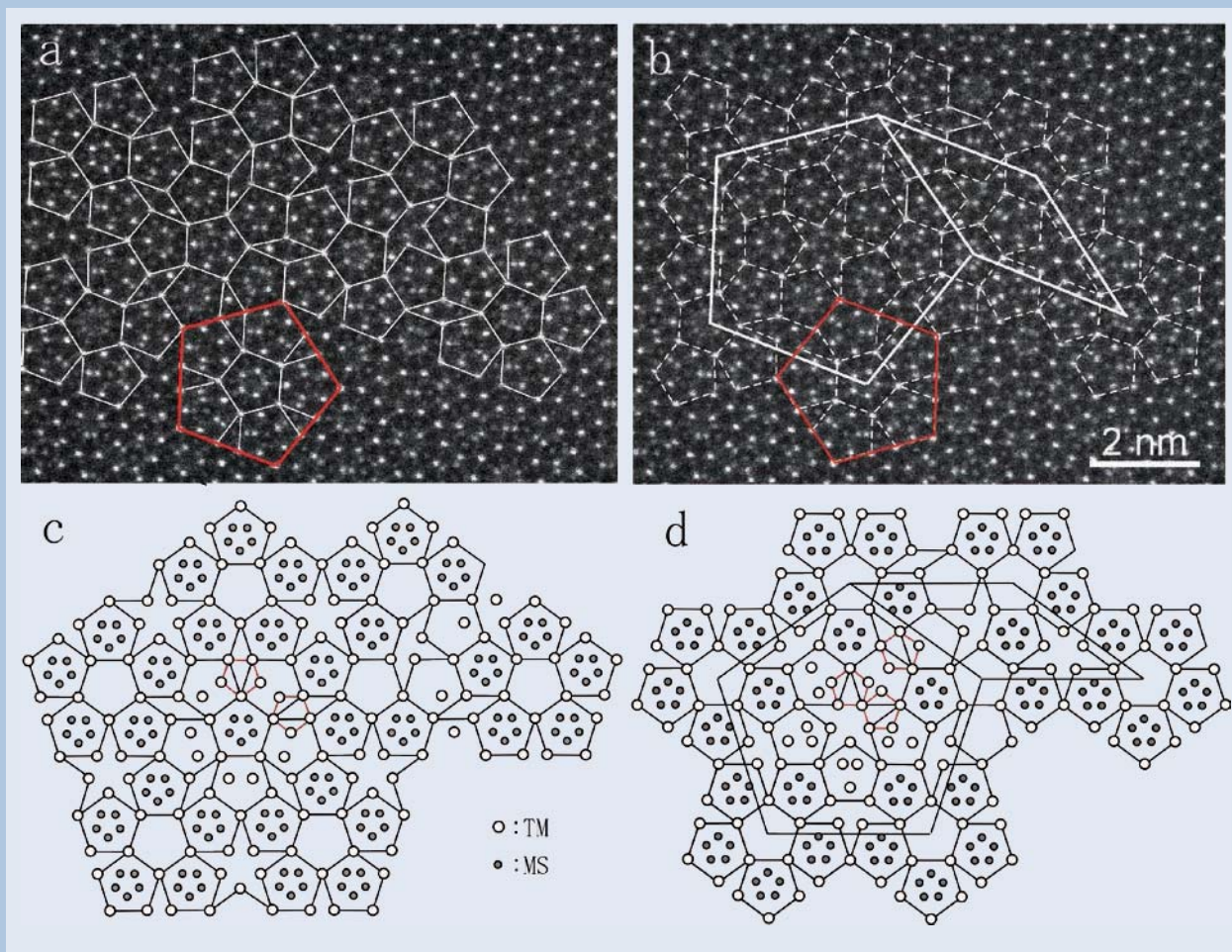


Fig. 6 HAADF-STEM images (a, b) of an $\text{Al}_{72}\text{Co}_8\text{Ni}_{20}$ decagonal quasicrystal, and arrangements of TM atoms (c, d) on the A and B planes, derived from arrangements of bright dots in (a) and (b). Most of bright dots in the image can be connected by lines with a length of 0.76 nm, as shown in (a) and (b). Also, one can see double pentagonal distributions of bright dots inside of rightward pentagons in (a) and leftward ones in (b), but in leftward pentagons in (a) and rightward ones in (b), a variety of distributions of bright dots, e. g. pentagonal, decagonal and asymmetric ones are observed. Note that large clusters with pentagonal symmetry in the pentagonal tilings of (a) and (b) are located at corners of a pentagonal frame with an edge-length of 3.2 nm, as indicated by pentagons of red lines in (a) and (b).

However, no detailed interpretation of these bright dots is mentioned in this paper. In the pentagonal tilings drawn in Figs. 6(a) and 6(b), one can see that large clusters with pentagonal symmetry, indicated by pentagons of red lines, are located at corners of a pentagonal frame with an edge-length of $3.2 (=2\bullet\tau)$ nm.

Figure 7 shows an ABF-STEM image of the $\text{Al}_{72}\text{Co}_8\text{Ni}_{20}$ quasicrystal, which was simultaneously taken with the HAADF-STEM images of Figs. 6(a) and 6(b). In the image, TM and Al atoms are represented as dark dots, but it is hard to distinguish between TM and Al atoms from contrast of the dark dots, because of showing little different darkness. In the image of Fig. 7, one can see small rings formed by ten dark dots encircling with an interval of about 0.13 nm, and almost all of the ring contrasts are arranged with an interval of about 0.66 nm. By a close examination of an arrangement of the ring contrasts, one can recognize definite large clusters, indicated by circles, formed with ten small rings encircling with tenfold rotational symmetry, at corners of a pentagonal frame with an edge-length of 3.2 nm. In contrast with the TM atoms and MSs exactly located at lattice points of a Penrose lattice with an edge-length of 0.25 nm, Al atoms are considered to shift from the lattice points, from the structures of the crystalline approximants of W-(AlCoNi) [13] and $\tau^2\text{-Al}_3\text{Co}$ [9], and it is difficult to determine exact positions of Al atoms from the ABF-STEM image. However, it is worthwhile to discuss the structure including an arrangement of Al atoms in the 3.2 nm cluster from the observed HAADF- and ABF-STEM images. **Figure 8** shows observed HAADF- and ABF-STEM images of the 3.2 nm cluster and its structure models. The arrangement of TM and MSs in Fig. 8(c) can be directly derived from an arrangement of bright dots in Fig. 8(a), and the structure of Fig. 8(d) including an arrangement of Al atoms is derived from the ABF-STEM image of Fig. 8(b), assuming that all Al atoms are located at lattice points in a Penrose lattice with an edge-length of 0.25 nm. As can be seen in Fig. 8(d), the ring contrasts with ten dark dots in the ABF-STEM image of Fig. 8(b) correspond to the projection of five MSs and five Al atoms, which are located on different planes, as indicated by circles in Fig. 8(d). All dark dots in the ABF-STEM image of Fig. 8(b) represent TM atoms, MSs and Al atoms. It should be mentioned here that the present structure model of the 3.2 nm cluster is nearly the same as that in a previous paper except for the existence of MSs [14]. However, the present result shows that the arrangement of TM atoms in a full region including the 3.2 nm clusters and glue regions between the clusters can be expressed as pentagonal tiling with an edge-length of 0.76 nm, and also indicates that all of TM atoms and MSs are located at lattice points of a Penrose lattice with an edge-length of 0.25 nm. That result shows that the structure of the $\text{Al}_{72}\text{Co}_8\text{Ni}_{20}$ decagonal quasicrystal should be characterized as the tiling of TM atoms and MSs with BOO, and consequently the 3.2 nm clusters are formed at well-symmetric positions of the tiling.

Summary

We show an overview of recent structural studies

of Al-TM decagonal quasicrystals by Cs-corrected STEM. Observed Cs-corrected HAADF-STEM images represent individual TM atoms and MSs in decagonal quasicrystals as separated bright dots, and enable us to directly derive arrangements of TM atoms and MSs on quasiperiodic planes stacking along the periodic axis. The results have shown that the structures of Al-TM decagonal quasicrystals should be characterized as BOO arrangements of TM atoms, and consequently disproved previous cluster-based models that have been widely accepted in a long time. It can be said that Cs-corrected STEM gives us innovative development for structural interpretations of decagonal quasicrystals.

References

- [1] S. Ritsch, C. Beeli, H. -U. Nissen, T. Godecke, M. Scheffer and R. Luck: *Philo. Mag. Lett.* **78**, 67-75 (1998).
- [2] K. Hiraga, T. Ohsuna, W. Sun and K. Sugiyama: *Mater. Trans.* **42**, 2354-2367 (2001).
- [3] K. Hiraga: *Advances in imaging and electron physics*, vol. **122**, 1-86 (2002) (Elsevier Science (USA)).
- [4] K. Saitoh, K. Tsuda, M. Tanaka and A. P. Tsai: *Z. Kristallogr.* **215**, 618-626 (2000).
- [5] E. Abe: *JEOL News* **42E**, 12-15 (2007).
- [6] S. Taniguchi and E. Abe: *Philo. Mag.* **88**, 1949-1958 (2008).
- [7] E. Abe: *Scanning Transmission Electron Microscopy, imaging and Analysis (Edited by S. J. Pennycook and P. D. Nellist, Springer New York Dordrecht Heidelberg London)* 583-614.
- [8] A. Yasuhara, K. Saito and K. Hiraga: *Proc. of Aperiodic 2012*, in press.
- [9] K. Sugiyama, A. Yasuhara and K. Hiraga: *Proc. of Aperiodic 2012*, in press.
- [10] K. Yubuta, A. Yasuhara and K. Hiraga: *Proc. of Aperiodic 2012*, in press.
- [11] K. Hiraga and A. Yasuhara: *Mater. Trans.* **54**, 493-497 (2013).
- [12] K. Hiraga and A. Yasuhara: *Mater. Trans.* **54**, 720-724 (2013).
- [13] K. Sugiyama, S. Nishimura and K. Hiraga: *J. Alloys & Comp.* **342**, 65-71 (2002).
- [14] K. Hiraga and T. Ohsuna: *Mater. Trans.* **42**, 509-513 (2001).
- [15] E. Abe, K. Saitoh, H. Takakura, A. P. Tsai, P. J. Steinhardt and H. -C. Jeong: *Phys. Rev. Lett.* **84**, 4609-4612 (2000).
- [16] E. Abe and A. P. Tsai: *JEOL News* **36E**, 18-21 (2001).
- [17] K. Saitoh, T. Yokosawa, M. Tanaka and A. P. Tsai: *Jpn. J. Appl. Phys.* **73**, 1786-1792 (2004).
- [18] K. Saitoh, N. Tanaka, A. P. Tsai and K. Ishizuka: *Philo. Mag.* **87**, 2732-2739 (2007).

Fig. 7 ABF-STEM image simultaneously taken with the HAADF-STEM image of Fig. 6. In the image, small rings formed by ten dark dots encircling with an interval of about 0.13 nm are arranged with an interval of about 0.66 nm. Large clusters formed with ten small rings encircling with tenfold rotational symmetry are located at lattice points of the pentagonal tiling with an edge-length of 3.2 nm. The large clusters correspond to those with pentagonal symmetry in Fig. 6(a) and 6(b).

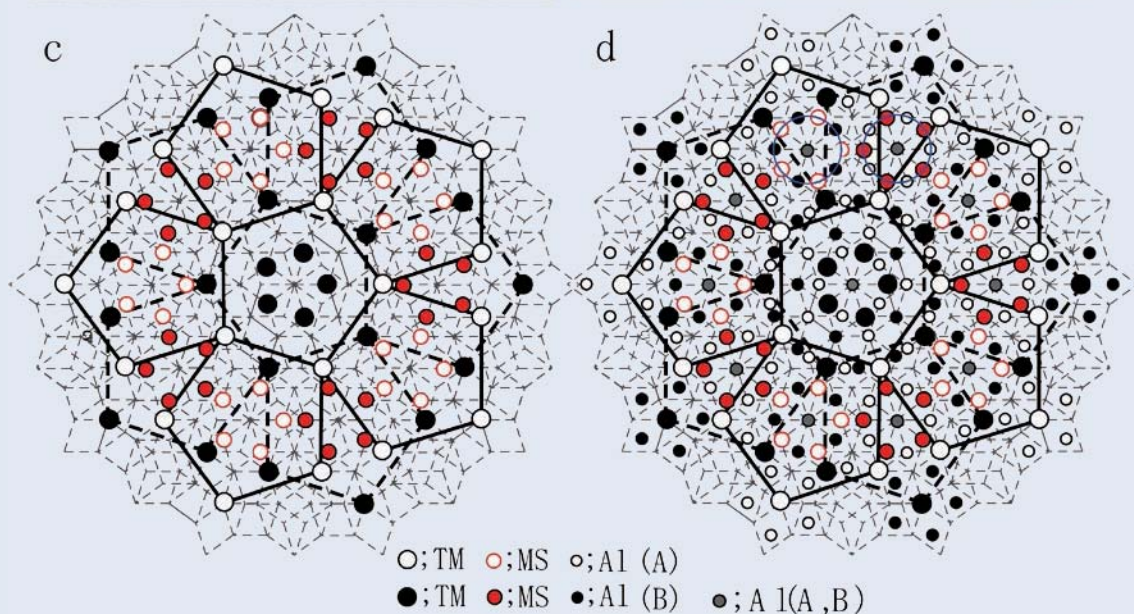
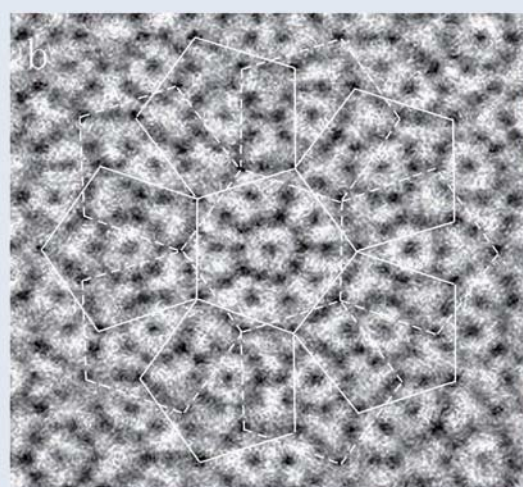
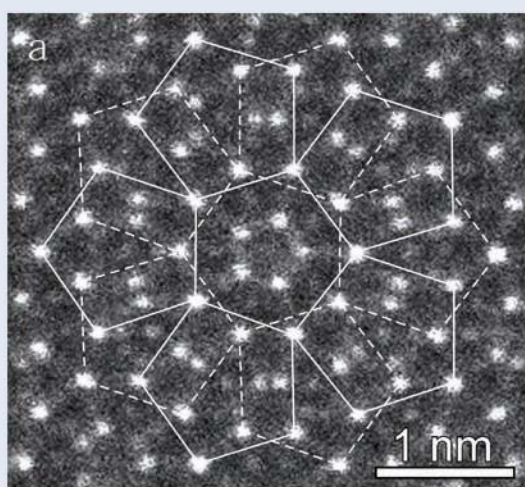
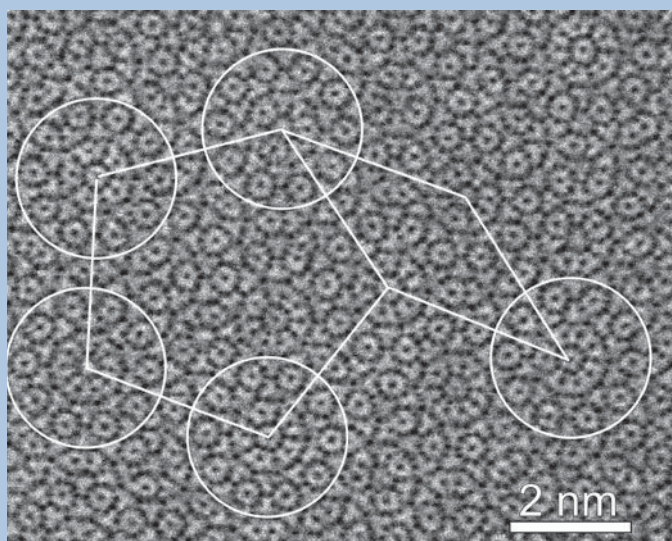


Fig. 8 HAADF (a)- and ABF (b)-STEM images, an arrangement of TM atoms and MSs (c), and a structure model (d) including Al atoms for the 3.2 nm cluster. The model of (c) is directly determined by the arrangement of bright dots in (a), and Al positions in (d) are derived from an arrangement of dark dots in (b), assuming that all Al atoms are located at lattice points in a Penrose lattice with an edge-length of 0.25 nm. The ring contrasts of ten dark dots in (b) correspond to the projection of five MSs and five Al atoms, which are located on different planes, as indicated by circles in (d). The tiling of thin dashed lines in (c) and (d) is a Penrose lattice with an edge-length of 0.25 nm.

Structural Analysis of Nanoparticles Using Scanning Transmission Electron Microscopy

Shinya Maenosono and Derrick Mott

School of Materials Science, Japan Advanced Institute of Science and Technology (JAIST)

The advanced technology of the JEOL JEM-ARM200F Scanning Transmission Electron Microscope (STEM) allowed unprecedented atomic scale analysis of a wide range of structurally complex nanoparticle (NP) systems including FePt@CdSe magnetic-fluorescent core-shell NPs, FePt@Ag magnetic-plasmonic core-shell NPs, (Au@Ag)@Au double-shell NPs, BiSbTe thermoelectric NPs, and ZnSb thermoelectric NPs. The use of a High Angle Annular Dark Field (HAADF) detector and an Energy Dispersive Spectroscopy (EDS) attachment revealed structural details of these NP systems that had not been previously possible. This news review highlights our recent NP structural analysis studies using this powerful instrument.

Introduction

Transmission electron microscopy (TEM) started off as a powerful biology analysis technique. Scientists used TEM instruments to analyze cell components or structures with higher resolution than was possible with optical microscopes. It was soon found however that the field of Materials Science had much to gain from TEM technology. The emerging field of Nanotechnology benefitted greatly because TEM offered a simple, straightforward and definitive way to determine nanoparticle (NP) size and shape by direct visualization. TEM information has since become indispensable to the field of nanotechnology and is virtually a requirement for any research article involving NPs. Over time, the technology has been enhanced. High resolution TEM (HRTEM) allows visualization of the atomic lattice in a crystalline material, further increasing the power and significance of the technique, revealing subtle crystal structural details. However, one disappointing aspect of the traditional TEM technology stems from the fact that the imaging resolution achieved has never approached that theoretically predicted, which originates from challenges in controlling the image forming electron beam in the instrument, level of vacuum, or stability of the high voltage source for the filament. As a result, true atomic resolution images have been elusive. Recently, however, new advances in TEM technology have increased the resolution limit to the subangstrom scale. By using aberration corrected scanning transmission electron microscopy (STEM), which relies on rastering a

focused electron beam over the sample, and a high angle annular dark field (HAADF) detector, which provides enhanced Z contrast, electron microscopy images with an atomic resolution (nominally 0.8 Å) have been achieved. Such ability opens the door to studying the atomic level structure of a wide range of materials, including NPs, whose properties may be strongly dependent on a unique atomic structure.

In our own recent research, we have synthesized various types of NPs including FePt@CdSe magnetic-fluorescent core-shell NPs, FePt@Ag magnetic-plasmonic core-shell NPs, Au@Ag@Au double-shell NPs, BiSbTe thermoelectric NPs, and ZnSb thermoelectric NPs. The physico-chemical properties of these NPs are strongly dependent on size, shape, crystalline structure, and composition. However, it was difficult to directly visualize the atomic structures of the heterostructured and/or multicomponent NPs using traditional TEM or even HRTEM techniques. In March 2010, JAIST installed the JEOL JEM-ARM200F scanning transmission electron microscope to try to address researchers' needs for atomically-resolved structural analysis in various fields. By using the JEM-ARM200F STEM instrument, we have analyzed a wide variety of NPs created in our laboratory. In this article, some examples of the structural analysis studies for these NPs using STEM are demonstrated.

FePt@CdSe magnetic-fluorescent core-shell NPs

Magnetic-fluorescent hybrid materials composed of magnetic NPs and semiconductor quantum dots (QDs) in novel heteronanostructures are intriguing because they can lead to new bioapplications. In the

1-1 Asahidai, Nomi, Ishikawa 923-1292, Japan

E-mail: shinya@jaist.ac.jp

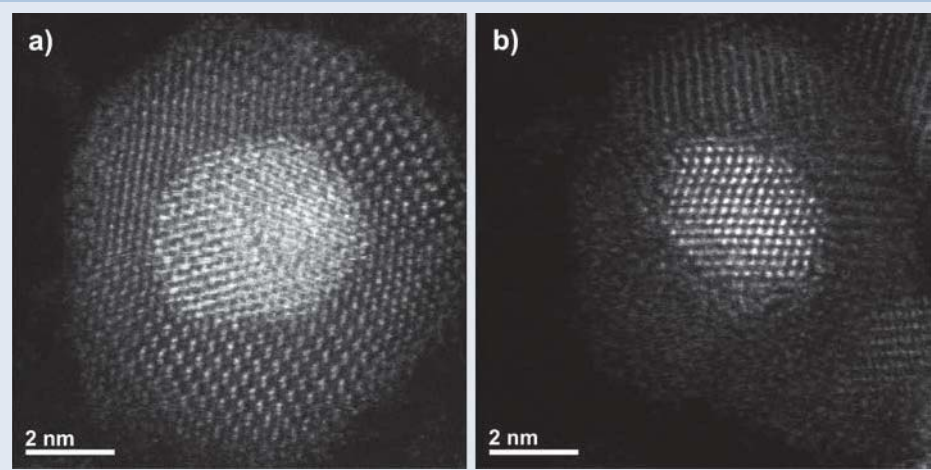


Fig. 1 STEM-HAADF images of two different single NPs in the FePt@CdSe sample. Core size and shell thickness are estimated to be (a) 4.6 nm and 2.3 nm, and (b) 4.1 nm and 2.1 nm, respectively. The results clearly demonstrate the core@shell structure.

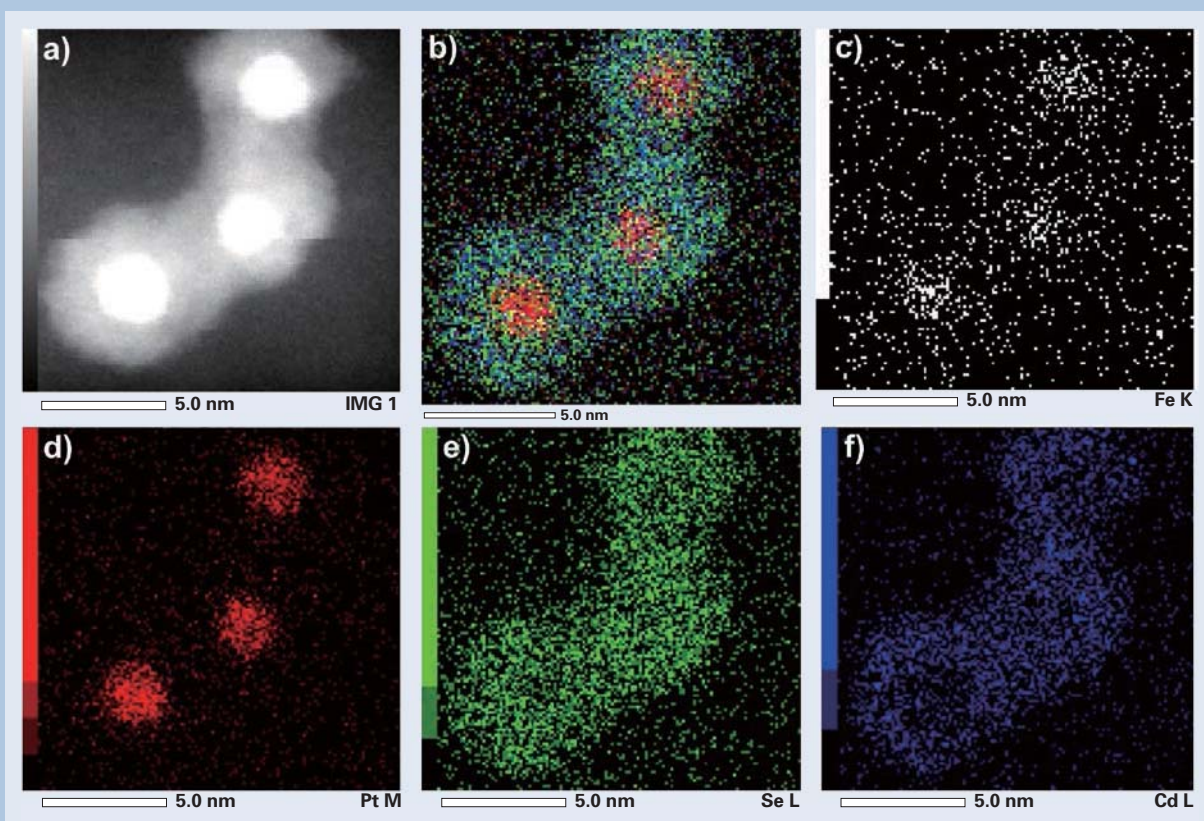


Fig. 2 HAADF-STEM image (a) and EDS elemental mapping images of FePt@CdSe NPs (b-f): Overlay (b) of Fe K edge (c), Pt M edge (d), Se L edge (e), and Cd L edge (f) illustrates the core-shell structure of the FePt@CdSe NPs.

case of the NPs discussed here, the magnetic core particle responds to an external magnetic field allowing protein separation, targeted drug delivery or other magnetic based applications while the QD shell is useful in cell labeling, cell migration tracking, in vivo imaging, etc. The combination of these two materials allows multiplexing of techniques or even new bioanalysis/treatment schemes to be employed. The synthesis of such core@shell structures with uniform structural parameters is challenging, however, requiring careful control of synthetic parameters. In this case, the NPs were created in a multi-step organic based wet chemical approach. The resulting NPs appeared

uniform in traditional TEM analysis, but to gain an understanding of the fine structural properties, we turned to the JEOL JEM-ARM200F instrument [1]. STEM imaging using a HAADF detector and two-dimensional EDS elemental mapping of individual NPs was performed to confirm the FePt@CdSe core@shell structure. **Figure 1** shows the STEM image of a single NP containing relatively heavy elements at the core and lighter elements in the shell (illustrating the enhanced Z contrast offered by a HAADF detector). The result clearly elucidates the FePt@CdSe core-shell structure where the FePt core is more dense than the CdSe shell. **Figure 2** shows the results of the EDS

elemental mapping analysis. The individual elemental maps show the relative positions of the core and shell materials, clearly identifying the core@shell structure visually. This is unambiguous evidence of the FePt@CdSe core-shell structure showing that Fe and Pt are localized in a core area in while Cd and Se are localized in the shell [1].

FePt@Ag magnetic-plasmonic core-shell NPs

Plasmonic (especially Au and Ag) NPs are ideal candidates for various sensing/imaging applications—including chemical/biological sensors, cellular imaging, immunodiagnosis, DNA sequencing, and photothermal therapy—because of their excellent localized surface plasmon resonance (LSPR) and surface enhanced Raman scattering (SERS) properties. Magnetic NPs (especially superparamagnetic NPs) are also promising materials for various applications, including the magnetic separation of chemicals/biomolecules/cells, site-specific drug delivery, magnetic resonance imaging (MRI), magnetic immunodiagnosis, and hyperthermia procedures. The combination of plasmonic and magnetic materials in a single nanostructure has the potential to lead to new applications in biology, such as immunomagnetic separation under plasmonic imaging monitoring, dual mode imaging (MRI and plasmonic imaging), and SERS sensing. FePt NPs are ideal as

a core particle material because of their enhanced saturation magnetization properties, while Ag makes for an enhanced plasmonic shell because of the high optical cross section of the material. We developed a scheme for the synthesis of well-defined FePt@Ag NPs with diameters larger than 10 nm, high SERS activity, high colloidal stability, and good magnetic separation capabilities, with the aim of using these NPs for biological sensing/imaging applications. The structure and composition of the as-synthesized NPs were fully characterized using STEM and two-dimensional EDS elemental mapping to definitively reveal the particle structural parameters [2].

To confirm the core-shell structure, HRTEM and STEM analyses were performed on an individual FePt@Ag NP. **Figure 3A** shows a HRTEM image of an individual FePt@Ag NP. Lattice fringes with d-spacing values of 0.236 and 0.205 nm—which respectively corresponded to the (111) and (200) planes of fcc-phase Ag (JCPDS card no. 01-071-3762)—were clearly identified. **Figure 3B** shows a HAADF-STEM image of an individual FePt@Ag NP. A bright spherical center and a less bright shell can be clearly observed, indicating that heavy Pt atoms were in the core, and light Ag atoms were in the shell. **Figure 3C–F** shows two-dimensional EDS elemental mapping images of a FePt@Ag NP. It was clear that Pt was found in the core area, and Ag was found in the shell area. The spatial resolution of EDS mapping is primarily governed by the degree of penetration and scattering of the electron

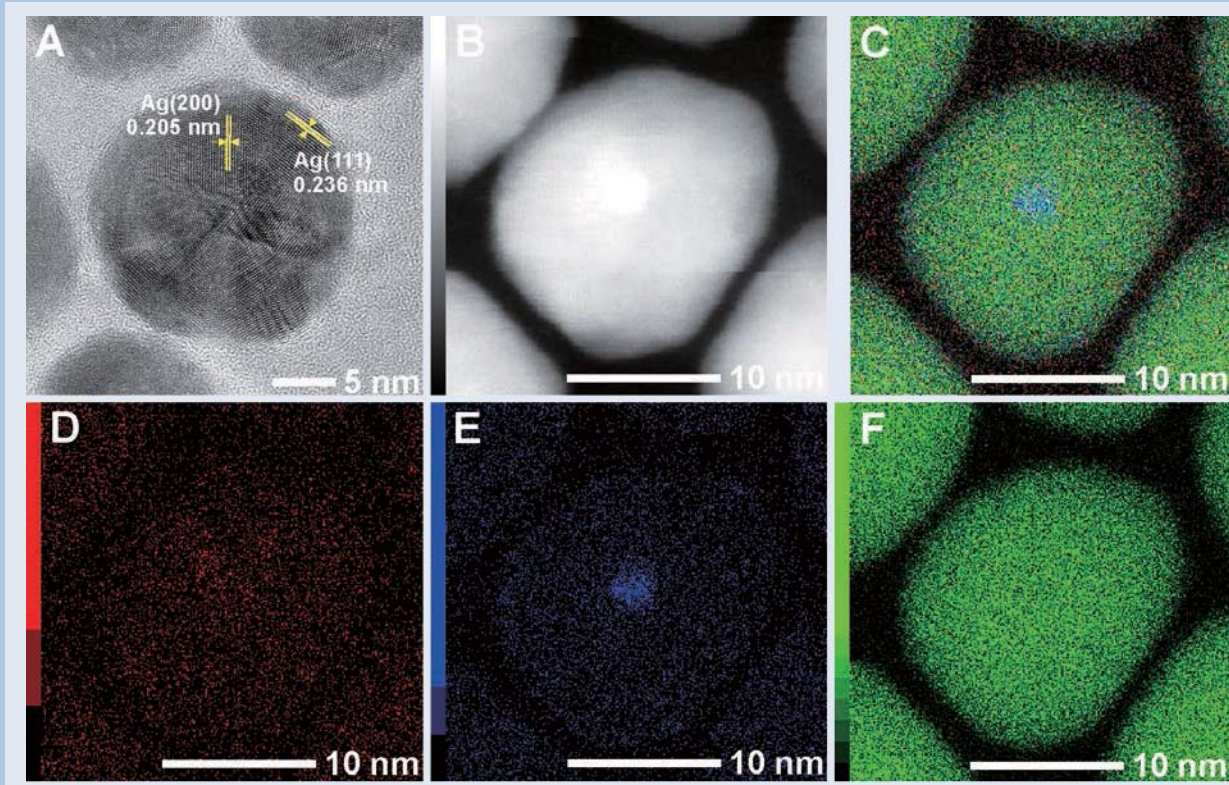


Fig. 3 (A) HRTEM, (B) HAADF-STEM and (C-F) EDS elemental mapping images of an individual FePt@Ag NP: (C) overlay, (D) Fe K edge, (E) Pt M edge, and (F) Ag L edge.

beam in the specimen, which may be highly influenced by the relative size of the materials imaged and the fact that the NPs are 3 dimensional in nature, while the resulting composition map is 2 dimensional (resulting in less resolution at the NP edges). Because of these limitations in the spatial resolution for the elemental mapping technique, the FePt core appears smaller than its actual size (4.5 ± 0.5 nm). In addition, small amounts of Fe and Pt are observed in the shell area, presumably due to background signal accumulation caused by the long measurement time (90 minutes) [2].

(Au@Ag)@Au double-shell NPs

Au and Ag NPs have intriguing optical properties that make them ideal candidates for use as probes in sensing and biodiagnostics applications. These probes optical, stability, and biomolecular reactivity properties are expected to be optimized by coupling the two metals in a core@shell (Ag@Au) structure where the core Ag provides ideal optical properties and the Au shell imparts chemical stability and reactivity with sulfur containing biomolecules. Despite many attempts to synthesize aqueous Ag@Au NPs, few attempts have succeeded in producing monodisperse NPs in terms of size, shape and structure. The challenges associated with synthesizing Ag@Au particles primarily stem from the galvanic replacement reaction that occurs between aqueous Au and metallic Ag during the shell deposition

procedure. In fact, galvanic replacement has been extensively utilized to generate hollow nanostructures including hollow metal particles, or gold nanocages. To synthesize monodispersed Ag@Au NPs the galvanic replacement reaction should be suppressed or eliminated, which is a challenge [3].

Based on our findings that Ag deposited onto a Au core causes a unique charge transfer phenomenon that increases electron density within the Ag shell (yielding a negative Ag oxidation state) which suppresses the galvanic replacement reaction and enhances the stability of the Ag, we further deposited a Au second shell onto the Au@Ag NPs to form defect-free (Au@Ag)@Au double shell NPs. To confirm the formation of the a Au second shell, STEM-HAADF imaging and EDS elemental mapping were carried out for the (Au@Ag)@Au double shell NPs using a JEOL JEM-ARM200F instrument. **Figure 4C** shows the STEM-HAADF image of the (Au@Ag)@Au double shell NPs. Since the heavier Au atoms (atomic number, $Z = 79$) give rise to a brighter image than the lighter Ag atoms ($Z = 47$) in the dark field image, the Au core appears brighter than the Ag first shell. One can see a very bright eggshell-thin layer on the Ag first shell (Fig. 4C). The thickness of the layer is 0.11 nm, which agrees well with the theoretical value (0.15 nm) calculated based on the amount of Au precursor used in the synthesis. This indicates that a thin Au second shell was formed on the Au@Ag NPs. The EDS mapping result (Fig. 4D-F) also clearly indicates

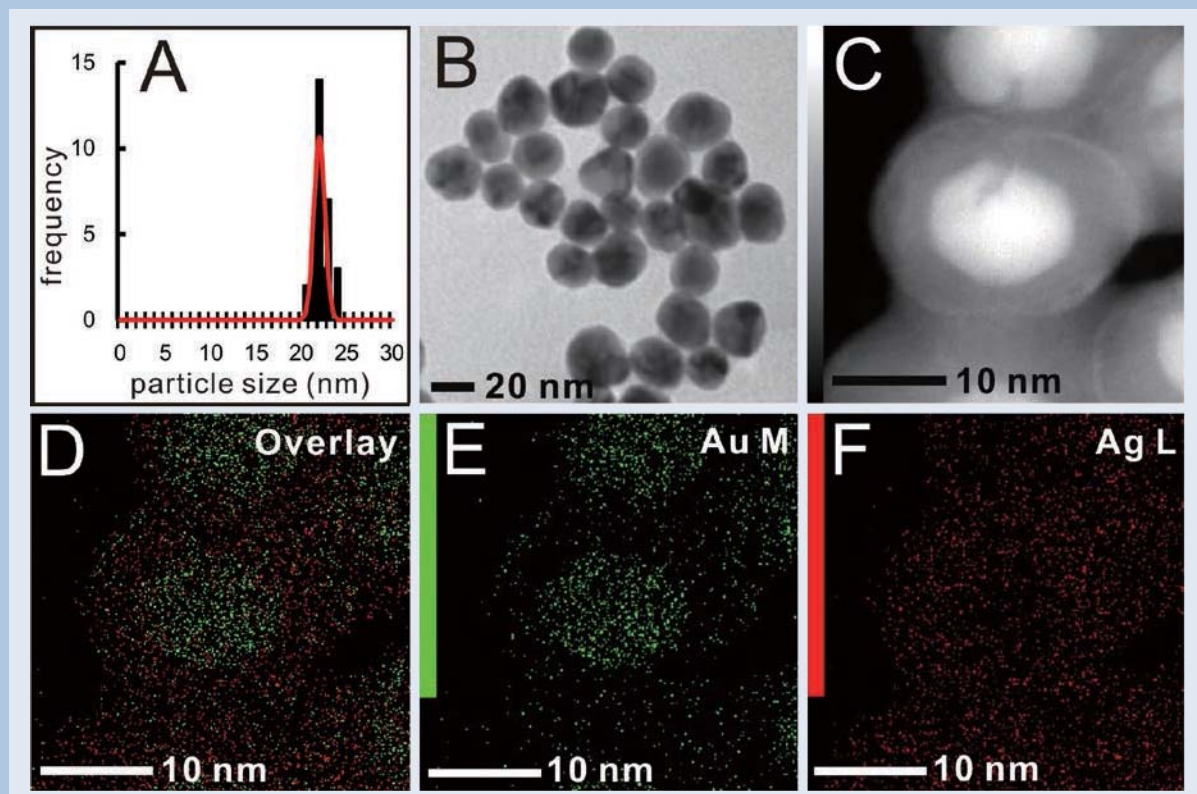


Fig. 4 Size distribution (A) and TEM images (B) of (Au@Ag)@Au double shell NPs. (C) STEM-HAADF image of (Au@Ag)@Au NPs. (D-F) EDS elemental mapping images of (Au@Ag)@Au NPs: Overlay (D) of Au M edge (E) and Ag L edge (F).

that the resulting NPs have a (Au@Ag)@Au double shell structure. While the outermost Au shell is only 1-2 Au atomic layers thick, the inter-diffusion of Au and Ag atoms could occur resulting in a Au-Ag alloy. For this reason, we deposited a thicker Au second shell with a theoretical thickness of 1.2 nm to further probe the characteristics of the second shell. **Figure 5** shows the STEM-HAADF and the EDS mapping images of the double shell NPs. The mean diameter of the resulting NPs is 23.0 ± 1.9 nm, which agrees well with the theoretical value (23.2 nm) calculated based on the amount of Au precursor added. This means that the Ag first shell was not etched away during the deposition of the Au second shell. As can be clearly seen in Fig. 5, the resulting NPs display a double shell structure with defect-free Au second shells [3].

BiSbTe thermoelectric NPs

One interesting area of research now focuses on nanostructured thermoelectric (TE) materials. In this field, the nanoscale particle size leads to enhanced TE efficiency for the overall material, primarily because of enhanced scattering of the heat carrying phonon at the crystal grain interface. Materials such as Bi_2Te_3 or $(\text{Bi}_{0.5}\text{Sb}_{0.5})_2\text{Te}_3$ have been demonstrated to be potentially powerful thermoelectric materials with incorporation of nanostructuring increasing the efficiency even more. However, several factors including the nanoscale particle properties (size, shape),

specific composition, and atomic level structure, dictate the resulting TE efficiency. The atomic structure for the NPs is an especially challenging area; however, by using the STEM-HAADF technique, the atomic structure for this class of material can now be definitively determined [4].

We successfully synthesized TE type NPs composed of Bi, Sb and Te with both wire (NW) and disc (ND) shapes. The synthesis technique was demonstrated to be very versatile with the NP morphology varied by simply changing the characteristics of the organic capping species used in the synthesis. The resulting particles have a uniform morphology; however, they exhibit phase segregation as evidenced by XRD analysis. It was found that the NWs are composed of primarily hexagonal Te and rhombohedral Bi_2Te_3 phases while the NDs are composed of Bi_2Te_3 and Sb_2Te_3 phases. One particular challenge was to determine whether the NPs are composed of a single phase (multiple single particle compositions) or if the single particles are themselves phase segregated. It was our objective to characterize the phase segregated properties of the NPs as well as gain an expanded understanding of the atomic structure for these materials. The JEOL JEM-ARM200F instrument provided the means to investigate these questions [4].

To address the question of whether the NPs are composed of single or multiple phases, EDS-Mapping was performed. This technique allows the visualization of the relative location of the different elements in

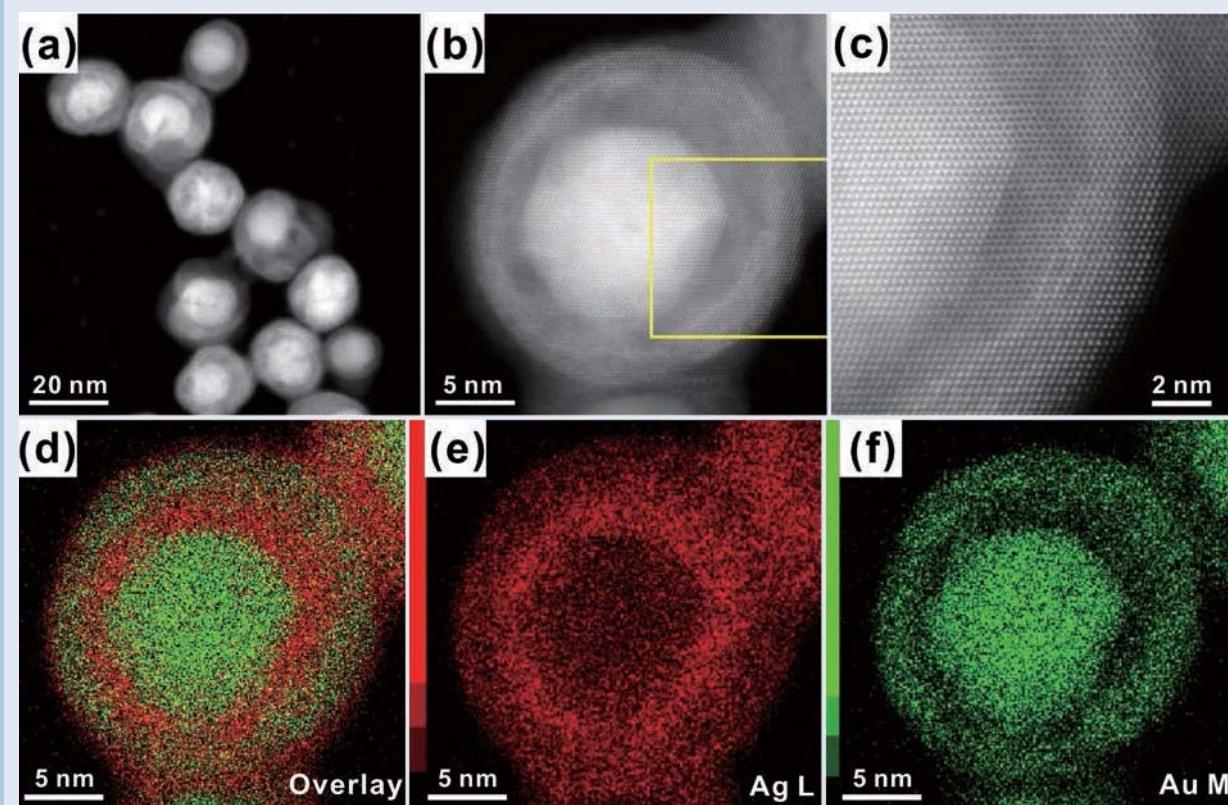


Fig. 5 (a-c) STEM-HAADF images and (d-f) EDS elemental mapping images of (Au@Ag)@Au double shell NPs with a thick Au second shell (1.2 nm): Overlay (d) of Ag L edge (e) and Au M edge (f).

the sample (a 2 dimensional map). The color intensity serves as a tool to judge the relative amount of element present. **Figure 6** shows the EDS-Mapping images for the NWs. In this figure a dark field image, as well as elemental maps for Bi (M line) and Te (L line) are included along with an overlay of the individual maps. Sb was not mapped in this analysis because of the relative instability of this element under the electron beam, which caused a significant decrease in the resolution of the data. The dark field image shows the wire morphology of the particles and serves as a reference for particle location when compared to the elemental maps. The map for Te indicates that Te is present at all locations within the NWs, however for Bi, the composition is not uniform, with Bi existing only at certain isolated areas within the wires. The overlay of the Bi and Te maps further elucidates this. The data indicates that the NWs are composed of a predominantly monometallic Te phase along with segregated areas of Bi_2Te_3 [4].

Figure 7 shows the EDS-Mapping result for a single ND oriented on face. In this analysis the dark field image along with mapping of Bi and Te areas is also shown, in addition to an overlay of the elemental maps. As above, Sb was not mapped because of the instability under the electron beam. The dark field image shows a single disc which may have a non-uniform surface, as indicated by the variation in contrast throughout the disc. As can be observed, there seems to be little inhomogeneity in the Bi and Te compositions (the lower right quadrant in the Te map

may indicate a heightened amount of the metal, which could arise because of a deviation in particle thickness). This result is consistent for particles composed of Bi_2Te_3 , however there were no areas observed that were devoid of bismuth. EDS-Mapping was also performed for the NDs lying on edge, however no inhomogeneity in the composition was observed. In light of these results, the NDs appear to be composed mostly of Bi_2Te_3 , however the location of Sb within the particles could not be discerned because of the instability under the electron beam in this analysis [4].

To more closely study the nanoparticle structure, aberration corrected STEM-HAADF was used. This allows atomic level imaging, the ability to differentiate between different elements in the image, and the ability to definitively identify the atomic structure of the material. **Figure 8** shows a STEM-HAADF image in roughly the center of a typical NW, with the wire running left to right. The white dots in the image represent individual atoms in the NW. The dark line running through the center of the wire is where two crystalline planes in the particle meet (a twin plane). The inset to the image shows the derived expanded unit cell for the material, which has a hexagonal structure. The unit cell c-axis length can be measured (5.93 \AA) providing a good indication that this section of the wire is composed of mono-elemental Te. This is further supported by the fact that each atom appears to have the same degree of contrast, indicating that this section of the particle has a uniform mono-elemental composition. The accompanying schemes in

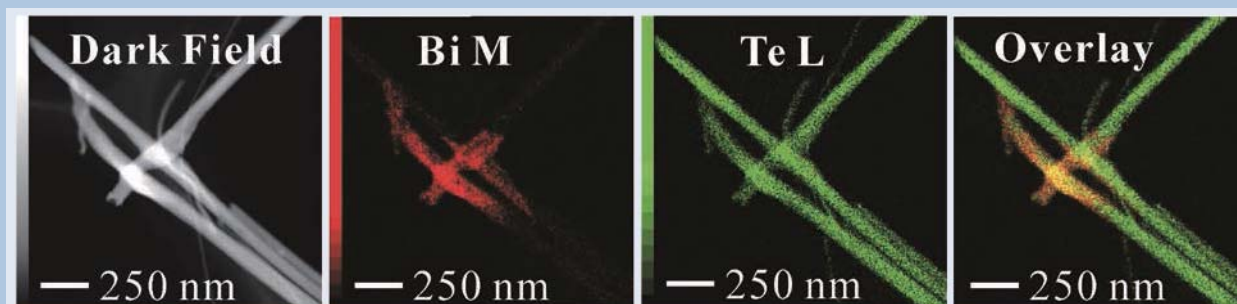


Fig. 6 EDS Mapping of NWs. From left to right, dark field image, Bi map, Te map, and an overlay of the Bi and Te maps.

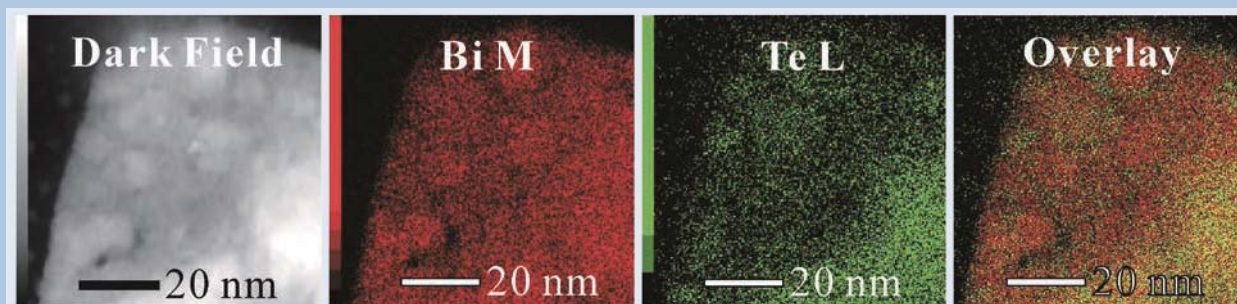


Fig. 7 EDS Mapping of a single ND synthesized with decanethiol. From left to right, dark field image, Bi map, Te map, and an overlay of the Bi and Te maps.

Fig. 8 STEM-HAADF image of (A) a nanowire in a Te monometallic area (1 nm scale bar). The accompanying schemes show (B) the crystal structure for hexagonal Te and (C) the corresponding unit cell derived from the STEM image.

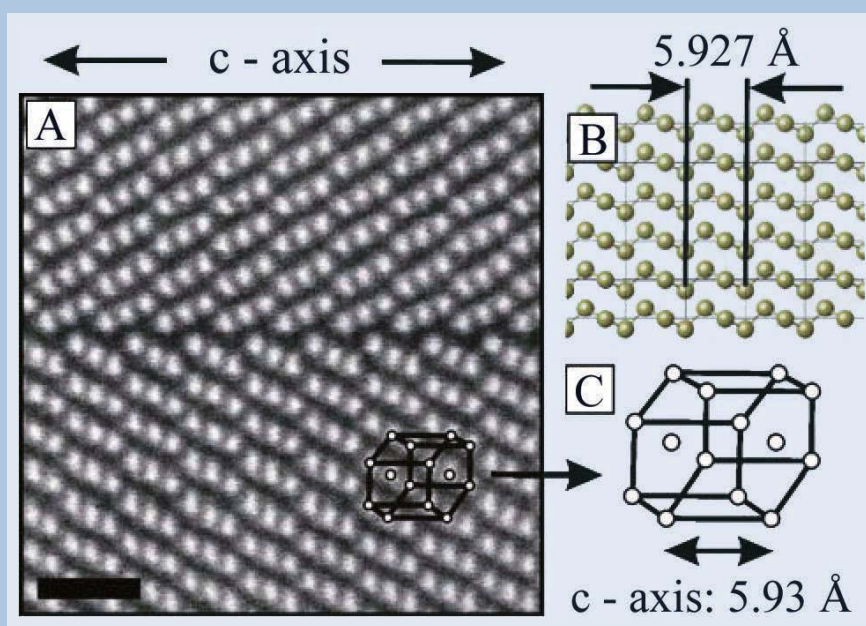


Fig. 8 show the crystal structure for hexagonal Te (top) and the corresponding expanded unit cell derived from the STEM-HAADF image (bottom), along with the corresponding reference and measured c-axis values [5].

Figure 9A shows the STEM-HAADF image of the tip of a single NW. The NW tip appears to have a different atomic structure/composition as compared to the center area of the NW. Figure 9B shows a zoomed in view of the area of the tip indicated by the box in Fig. 9A. In this image two different atomic structures can be observed. On the left side of the image, the Te hexagonal structure can be visualized (the same as in Fig. 8), while on the right hand side of the image, a different atomic structure is observed. While it is difficult to definitively identify the crystal structure in this region of the NW (primarily because the crystal orientation plays a large role in the image obtained), this structure is certainly not hexagonal in nature. The fact that the NW tip is darker than the side walls is likely because the tip is angled away from the viewing plane, and is not a result of Z-contrast in the sample. Figure 9C shows the STEM-HAADF image of a separate NW displaying a clearer image of the more complex crystal structure. Based on the earlier EDS-Mapping experiment, these areas seem to be composed of Bi_2Te_3 with rhombohedral structure. It is especially apparent in Figure 9C that the contrast varies markedly among different atoms in the image, which could arise as a result of Z-contrast (Bi Z = 83, Te Z = 52), or because of the particle structure (the dimmer atoms would be farther from the viewing plane than the bright ones). The rhombohedral structure is further confirmed by comparing the observed atomic lattice to a modeled one. Figure 9D shows a model of the Bi_2Te_3 crystal with rhombohedral structure. The model was aligned to correspond with the orientation of the NW observed in the STEM image (Fig. 9C). The resulting pattern that is formed shows rows of atoms that

form a zigzag pattern, similar to that observed in the STEM image. The bright atoms that are observed in the STEM image (represented by the white circles in the Fig. 9D) may cause increased scattering of the electron beam, decreasing the penetration depth (as a result of particle structure or the identity of these atoms) which could explain why rows of zigzagging atoms are not observed for the bright atoms. Overall, the images indicate that the bulk of the NWs are composed of Te, which has a hexagonal structure, while Bi_2Te_3 with rhombohedral structure seems to have grown from the tips of the wires. The results indicate that the NWs contain 2 phases, and suggest that the phase segregation is a result of the particle growth mechanism, where Te wires formed initially, followed by growth of Bi_2Te_3 at the nanowire tip [5].

For the NDs, **Figure 10** shows the STEM-HAADF image of a single particle on a face. The atomic structure of this particle is much different than that observed for the NWs. In this image, 3 different types of atoms can be observed with different contrast including relatively bright, dim and intermediate contrast. The inset to the image in Fig. 10 represents a top down view of the expanded unit cell for the material where the a-axis value (4.33 Å) and the 101 crystalline plane spacing (3.75 Å) indicates that the material has a rhombohedral structure and is likely composed of Bi_2Te_3 or Sb_2Te_3 . The accompanying schemes in the image show the reference structure for $\text{Bi}_2\text{Te}_3/\text{Sb}_2\text{Te}_3$ as viewed down the c-axis (top) and the measured values for the a-axis and 101 plane spacing (bottom). These values are also consistent with $(\text{Bi}_{0.5}\text{Sb}_{0.5})_2\text{Te}_3$, which could exist as a minor phase in the sample. The difference in contrast could arise as a result of the identity of the atoms in the particle (i.e. Bi, Sb or Te), but in this case it may also be that the contrast arises as a result of the atomic structure. In the rhombohedral structure each crystalline plane is offset from the one above it, resulting in 3 repeating layers (if you view the structure along the c-axis). In this case the top layer would be the brightest, with the middle layer

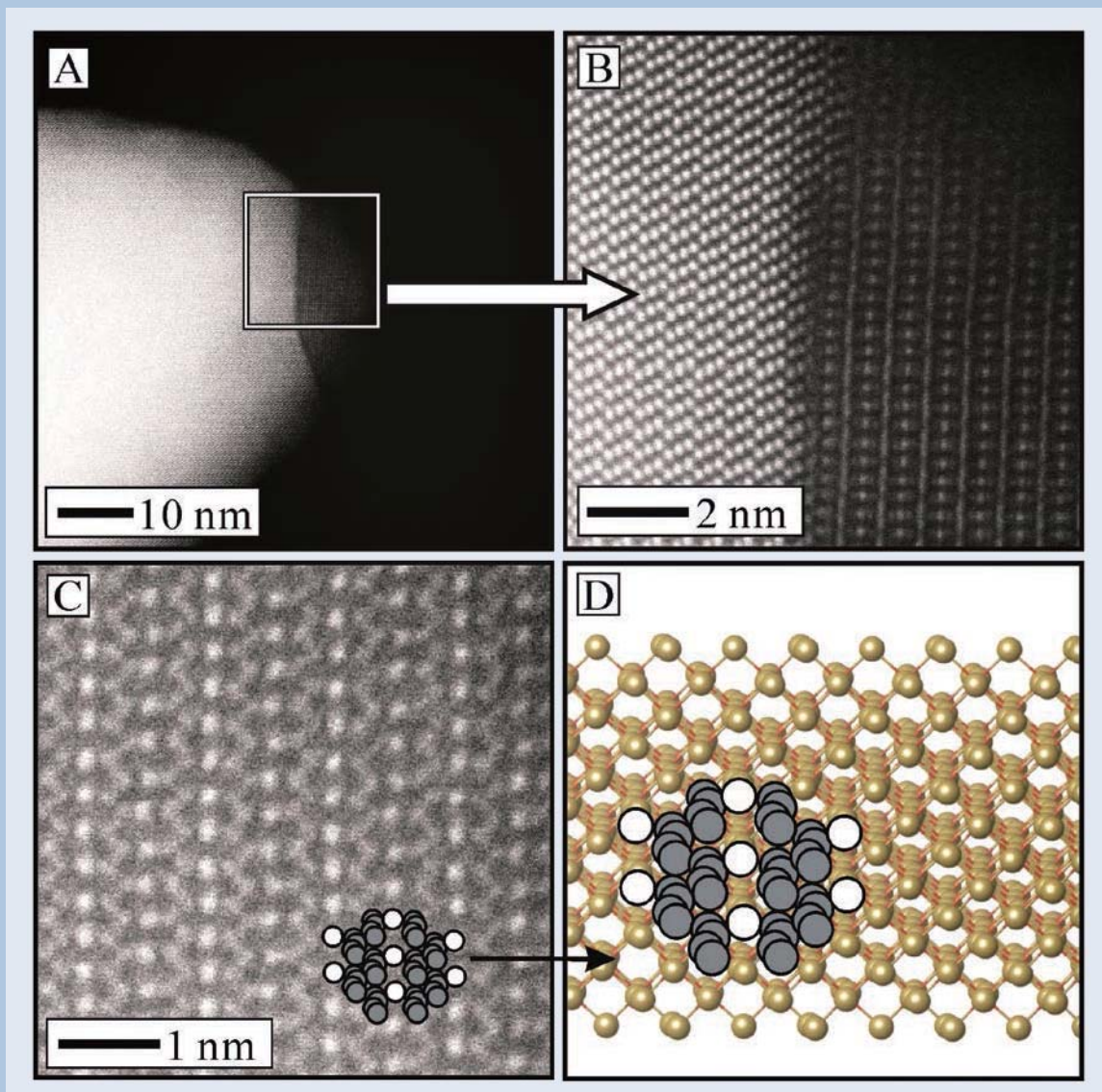


Fig. 9 STEM-HAADF image of (A) a nanowire tip, (B) a magnified view of the tip, (C) an area exhibiting the rhombohedral structure and (D) a scheme illustrating the rhombohedral Bi_2Te_3 structure observed in the sample.

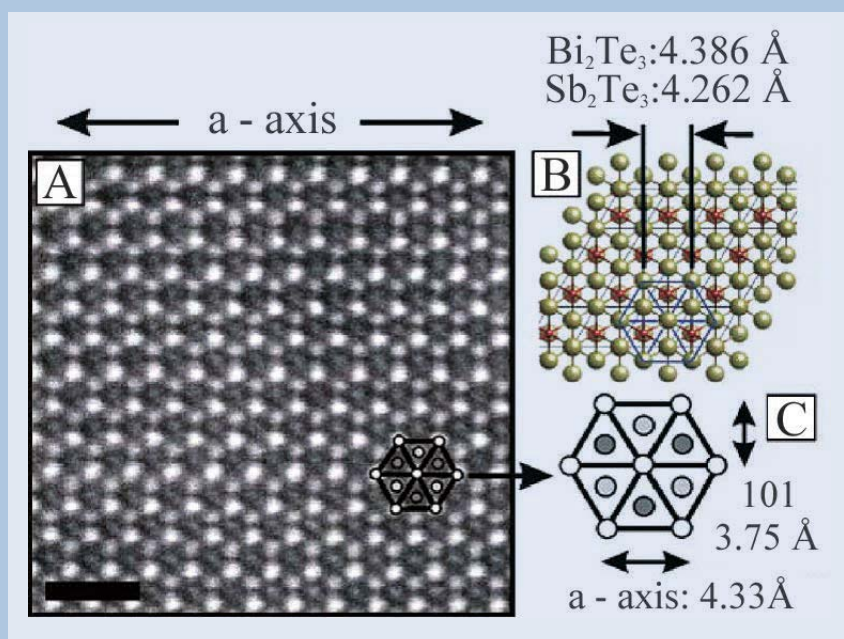


Fig. 10 STEM-HAADF image of (A) a nanodisc on face (1 nm scale bar). The accompanying schemes show (B) the crystal structure for rhombohedral $\text{Bi}_2\text{Te}_3/\text{Sb}_2\text{Te}_3$ and (C) the corresponding unit cell (viewed down the c axis) derived from the STEM image.

being dimmer, and the final layer being the dimmest. It is likely a combination of these two factors that cause the difference in the observed contrast among the different atoms in this sample [5].

ZnSb thermoelectric NPs

Zn-Sb systems (especially β -Zn₄Sb₃ phase) exhibit excellent TE properties because of their remarkably low thermal conductivity (κ) due to the disordered local (PGEC) structure. In addition, Zn-Sb consists of relatively abundant elements, and thus, it has been regarded as a promising candidate for TE energy harvesting. Recently, we succeeded in synthesizing ZnSb NPs via a sequential reduction of metal precursors and subsequent alloying. Figure 11a-c shows TEM images indicating that the resulting as-synthesized NPs are nearly spherical in shape and have a mean size of 21.1 ± 3.4 nm. The mean size and size distribution of NPs were estimated from randomly-selected NPs observed in the TEM images. TEM-EDS analysis on single NPs as well as an ensemble of NPs confirmed that each NP contains both Zn and Sb with an average atomic ratio of Zn:Sb = 47:53. **Figure 11d** shows the HAADF-STEM image. As can be seen, the Z contrast decreases from center to edge suggesting that Zn is rich at the periphery while Sb is rich in the core. The lattice fringes with different d-spacings can be clearly resolved in Figure 11c and d. However, it is difficult to determine which phase these crystal planes belong to because several different phases have lattice

planes with similar d-spacing [6].

To confirm the composition distribution in the Zn-Sb NPs, EDS mapping was carried out for a single Zn-Sb NP (**Figure 12**). Both Zn and Sb are found to be distributed over the entire area of a single NP. The cross-sectional line profile (Figure 12e) confirmed that Sb is rich in the center and Zn content increases at the periphery. Similar results were obtained for other single NPs indicating that this structural feature is typical and uniform [6].

Conclusion

Nanoparticles with progressively more complex atomic structure have become common because of the unique properties these materials possess. Using traditional techniques such as low resolution TEM analysis, the complex structure of new nanoparticles could not be directly observed, leading to a restriction in the technological advancement of complex structure nanomaterials. However, with the advent of the high resolution STEM-HAADF technique, provided in this case by the JEOL JEM-ARM200F instrument, we have successfully studied the complex structure as well as atomic level structure of a series of complex nanoparticles. The analysis technique allowed atomic scale imaging, Z contrast analysis, as well as elemental mapping (with an EDS instrument attachment). The results have provided an unprecedented view of the complex structure of nanoparticles and for the first time, definitive evidence for complex structured materials.

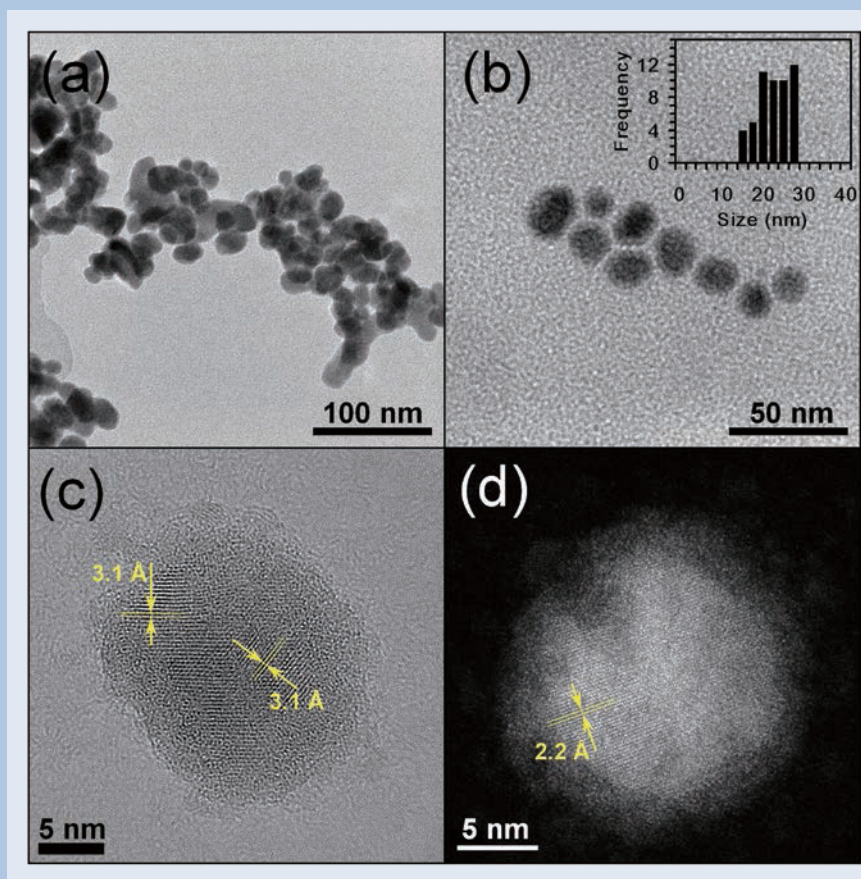


Fig. 11 (a,b) TEM images of Zn-Sb NPs. The inset in (b) shows the size distribution of NPs. (c) HRTEM and (d) STEM-HAADF images of a single Zn-Sb NP.

Acknowledgments

We would like to acknowledge the excellent nanotechnology center facilities and staff for their constant efforts in maintaining and operating advanced instrumentation including the JEOL JEM-ARM200F instrument. We would especially like to thank Mr. Koichi Higashimine for his tireless efforts in assisting us with operating the JEM-ARM200F instrument.

References

- [1] T. T. Trinh, D. Mott, N. T. K. Thanh, S. Maenosono, *RSC Adv.*, **1**, 100 (2011).
- [2] N. T. T. Trinh, T. T. Trinh, K. Higashimine, D. Mott, S. Maenosono, *Plasmonics*, **8**, 1177 (2013).
- [3] D. T. N. Anh, P. Singh, C. Shankar, D. Mott, S. Maenosono, *App. Phys. Lett.*, **99**, 073107 (2011).
- [4] D. Mott, N. T. Mai, N. T. B. Thuy, Y. Maeda, T. P. T. Linh, M. Koyano, S. Maenosono, *Phys. Status Solidi A*, **208**, 52 (2011).
- [5] D. Mott, N. T. Mai, N. T. B. Thuy, T. Sakata, K. Higashimine, M. Koyano, S. Maenosono, *J. Phys. Chem. C*, **115**, 17334 (2011).
- [6] N. T. Mai, D. Mott, K. Higashimine, S. Maenosono, *Chem. Lett.*, **41**, 1529 (2012).

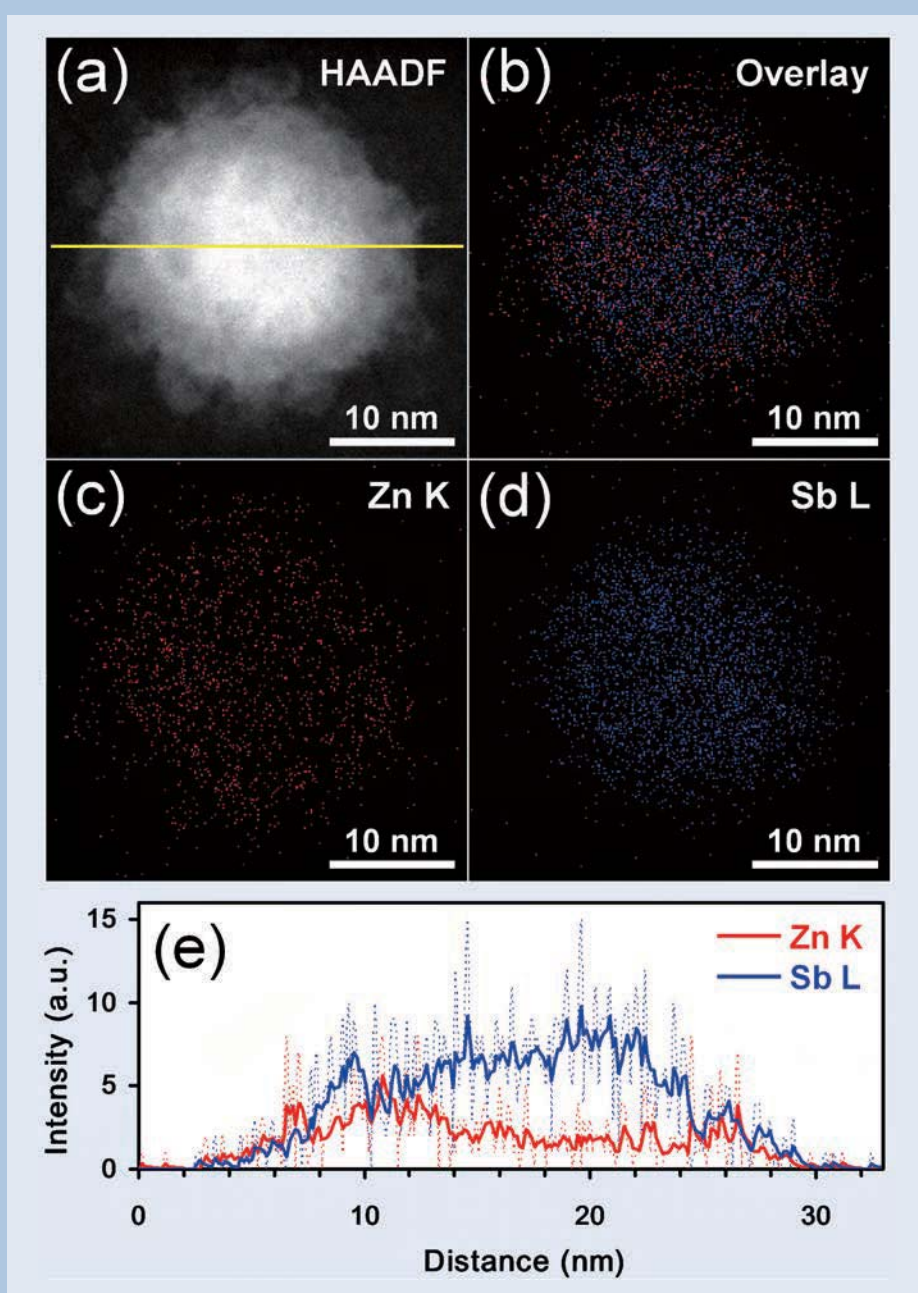


Fig. 12 (a) HAADF-STEM and (b-d) EDS elemental mapping images of a Zn-Sb NP: Overlay (b) of Zn K edge (c) and Sb L edge (d). (e) The EDS line profile at the center of the NP as indicated by a yellow line in (a). Dashed and solid lines represent raw and low-pass-filtered profiles, respectively.

Novel Structural Characterisations of Insulating and Electron Beam Sensitive Materials Employing Low Voltage High Resolution Scanning Electron Microscopy

Osamu Terasaki^{1,2}, HaeSung Cho¹, Minhyung Cho¹, HuYoung Jeong¹, Shunsuke Asahina³, Yusuke Sakuda³, Mituo Suga³, Hiroyoshi Kazumori³, Masato Kudo³, Takeshi Nokuo³, Zheng Liu⁴, Sam M Stevens^{5,6}, Michael W Anderson⁶, Diana Carolina Galeano Nunez⁷, Ferdi Schüth⁷, Tomas Kjellman⁸, Viveka Alfredsson⁸, Lu Han⁹, Shunai Che⁹, Hexiang Deng¹⁰, Omar Yaghi¹⁰, Kanghee Cho¹¹ and Ryong Ryoo^{11,12}

¹ Grad School of EEWS, KAIST

² MMK, EXSELENT, Stockholm Univ

³ JEOL Ltd.

⁴ Nanotube Research Center, AIST

⁵ Private Contributor

⁶ School of Chem, Univ of Manchester

⁷ Max-Planck-Inst für Kohlenforschung, Mülheim

⁸ Dept. Physical Chemistry, Lund Univ

⁹ School of Chem & Chem Eng, Shanghai Jiao Tong Univ

¹⁰ Dept of Chemistry, UCB

¹¹ Center for Nanomaterials and Chemical Reactions, IBS

¹² Dept of Chem, KAIST, Korea

Following our previous appraisal of high resolution scanning electron microscopy (JEOL News 50th Anniversary Issue) we return to assess the increasing information from *nano materials* (mesoporous materials, zeotypes, MOF and core-shell materials) delivered to the microscopist through utilisation of scanning electron microscopes employing lenses made from combinations of both electric and magnetic fields. The current limitations are also discussed in detail along with future improvements.

Introduction

Nano material research, requires observation of surface morphology, fine structures and local elemental distribution of samples. Unlike transmission electron microscopy (*TEM*), scanning transmission microscopy (*STEM*) and atomic force microscopy (*AFM*), scanning electron microscopy (*SEM*) retains a much larger depth of field allowing a greater sense of perspective during characterisation of a material whilst maintaining a high resolution. *SEM* is heavily used in the pursuit of understanding *nano materials* in terms of composition and topographic detail including fine structures since the significant improvement has been made in spatial resolution and detection sensitivities for low voltage electrons in recent years [1].

SEM works by demagnifying an electron beam from source to a small probe, which is scanning upon the surface of a sample, and collecting signals emitted from the sample as a function of the sample position.

Here we discuss the signals, secondary electrons

(*SEs*), backscattered electrons (*BSEs*) and characteristic X-rays through energy dispersive (*EDS*) detector. The probe size on the specimen surface, *d*, essentially determines a spatial resolution. Improvement in the performance of *SEM* requires one to: (i) make *d* as small as possible; (ii) separate *SE* and *BSE* signals as far as possible; (iii) enhance *S/N* ratio of the signals; (iv) reduce electron charge up in poorly conductive samples and the subsequent effect on image quality; (v) reduce surface contamination; and (vi) reduce effects of electron irradiation of the sample and subsequent damage.

In this review article, recent improvements of *SEM*, especially performances of JEOL JSM-7401F/7600F and JSM-7100FTTL/7800F concerning to the above mentioned (i–iii), and their outcomes of nano material observation on the (iv & vi) are described.

Diameter of primary electron (*PE*) on a specimen

The size of electrons source is demagnified through condenser and objective lenses by a magnification factor *M* to a probe at the specimen surface of size *d*. Independent factors such as spherical, chromatic &

¹ Daejeon 305-701, Korea, terasaki@kaist.ac.kr

² SE-10691 Stockholm, terasaki@mmk.su.se

(a) Energy Spectrum of emitted electrons from a sample (b) Classification of various secondary electrons (SEs) and their spatial distribution together with Monte Carlo simulation for Si

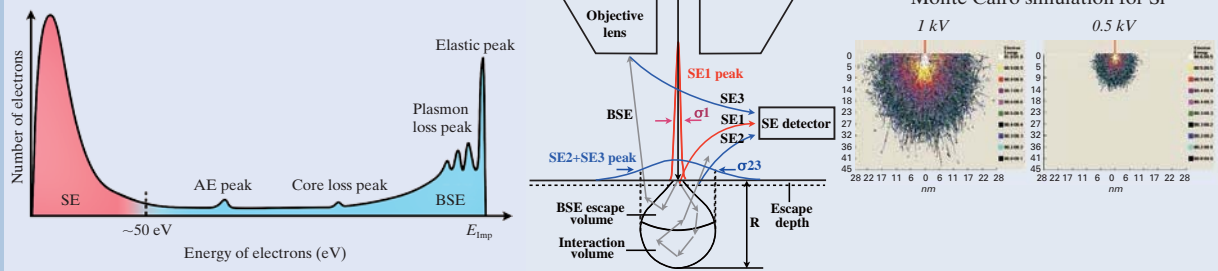


Fig. 1 Schematic diagram of the energy spectrum of emitted electrons from a sample (a), Classification of various secondary electrons (SEs) and their spatial distribution together with Monte Carlo simulation for Si (b). The spatial distribution of SE2 and SE3 is related to the size of BSE escape volume. Spatial distribution of SE1 vs. SE2 and SE3 are schematically shown by red and blue curves, respectively. Full width at half maximums (FWHMs) of SE1 and (SE2 and SE3) are discussed in the papers by Seiler [3] and Cazaux [4]. It is quite clear from Figure 1b that in order to obtain high resolution SEM image irrespective of SEs or BSEs at any landing energies, the best way is to use thin sample with the order of SE escape depth like nano particles on a TEM micro-grid.

diffraction aberrations blur the focus of the probe. The effective size of the probe of primary electrons (PEs) impacting on the surface on a sample, d , is given by the following equation using conventional parameters: [2]

$$d^2 = \sqrt{d_0^2 + d_d^2 + d_s^2 + d_c^2}$$

d_0 , d_d , d_s , and d_c are contributions to the disc of least confusion from source size, diffraction, spherical aberrations, and chromatic aberration, and these are expressed thusly:

$$d_0 = \frac{2}{\pi\alpha} \cdot \sqrt{\frac{I_p}{\beta}}$$

$$d_d = \frac{0.6\lambda}{\alpha}$$

$$d_s = 0.5C_s\alpha^3$$

$$d_c = C_c \frac{\Delta E}{E}\alpha$$

Where: I_p = PE beam current; β = brightness of electron source; α = PE convergence angle at sample position; λ = the wavelength of the PE at the sample; C_s = spherical aberration constant; C_c = chromatic aberration constant; ΔE = energy spread of electron source; and E = landing energy (landing voltage) at the sample, respectively.

Electrons of various types are emitted from the irradiated volume (interaction volume) and their energy spectrum is schematically shown in **Figure 1a**. Emitted electrons are conventionally classified as BSEs or SEs with electron energy larger or smaller than 50 eV, respectively.

Higher spatial resolution is principally achieved by reducing the diameter of a PE beam (d , see Figure 1b), and/or reducing the signal generation volume (the area of the interaction volume where detectable electrons are emitted). Reduction of the impact electron energy (landing energy) onto a specimen, will reduce the signal generation volume region and also limit electron radiation damage and electron charging problems in electrically insulating materials. However, the associated increase in probe size and loss of resolution therefore drives new improvements

of an objective lens both in making the effective probe size d small based on the above equation and enhancing detection sensitivity. Furthermore, emitted electrons containing morphological and compositional information of the sample require separation or superimposed if necessary by selecting energy of signal electrons. Considering these things, reducing diameter of PE on a specimen at low landing energy and energy selections of signal electrons are of extreme importance.

PEs change their directions once impacting with the sample surface through elastic and inelastic scattering inside a specimen. As SEs have kinetic energy smaller than 50 eV, and the associated limited escape depth means only SEs close to the specimen surface are emitted. The escape depth is approximately 5 times the mean free path of SEs. The mean average escape depth is 0.5~1.5 nm for metals and 10~20 nm for insulators. [3] SE1s and SE2s are generated by PEs and BSEs, respectively. SE3 are generated outside the specimen by BSEs hitting a pole piece and/or chamber walls (Figure 1b). Obtaining surface structural information in high resolution requires selection and enhancement of SE1 collection since SE1 has high special information having been emitted near the impact point of PEs, SE2s and SE3s carry information from the interaction volume through BSEs. Unfortunately, SE detectors cannot distinguish SE1s from SE2s and SE3s producing an SE image of SE1 information superimposed with BSEs information of lower resolution. A reduction in the landing energy of PEs, will reduce the signal generation volume of BSEs resulting in SE2 and SE3 electrons of higher spatial resolution. High resolution SE and BSE images can therefore be obtained with low landing energy PEs as well as BSE image.

A combination of magnetic lens and retarding electrostatic field had been used from the early stages of SEM [5]. In 1981, Yau *et al.* investigated an objective lens combining a magnetic field with a retarding electrostatic field to reduce the diameter of the PE, [6] (electromagnetic lens). Combining these fields makes the lens effectively stronger with a comparatively shorter focal length. Therefore, aberrations of the electromagnetic lens are smaller than those of purely

magnetic and purely electrostatic lenses. Various types of electromagnetic lenses have been proposed and realized. [7] The substrate negative bias (also called *sample bias*) with respect to objective lens for conventional purely magnetic lens makes the objective lens an electromagnetic lens, since an electrostatic retarding field is generated between the magnetic lens and the sample, and this field acts as a focusing field for primary electrons. This is especially valuable for low energy *PEs*, since lens effect of electrostatic field is strong for low energy *PEs* and furthermore reduces both *Cs* and *Cc* values. This electrostatic field also acts as an accelerating field for signal electrons from a sample, which is used as a part of detection system as described later.

Using sputtered gold nanoparticles on carbon, the dependence of *SEM* image resolution on specimen bias is shown in **Figure 2** by keeping landing energy constant at 500 eV. It is clearly observed that the resolution of the *SEM* image has been greatly improved with increase of specimen bias from 0 to -5 kV.

Schematic diagram and typical trajectories of *SEs* (blue) and *BSEs* (red) for JSM-7401F/7600F are shown in **Figures 3a-d**, respectively. In the detection system of 7401F/7600F, there are several electrodes to select signal electrons. This detection system is called r-filter. Acceleration electrode (*AE*) acts as energy filter: high energy *BSEs* always go through it, but transmission of low energy *SEs* depends on bias voltage of *AE* (Figure 3b-d). When *AE* is biased in positive, *SEs* can go through it (Mode *SE* (Figure 3b) and Mode *Sb* (Figure 3d)), but when it is negative, *SEs* cannot go through it (Mode *BSE* (Figure 3c)). In Mode *SE*, *SEs* are effectively collected by the electric field produced by middle electrodes (*MEs*) as described in Figure 3b, while *BSEs* hit the reflector electrode (*RE*) and generate *SEs* (*SE3s*), but these *SE3s* are trapped by positively biased *RE* resulting in selective detection of *SEs*. In *BSE* mode (Figure 3c), *SEs* emitted from a sample are reflected by *AE*, while *BSEs* hit the reflector electrode, and generate *SEs* (*SE3s*). These *SE3s* are collected by Secondary Electron Detector (*SED*) thanks to negative bias to *RE* and *MEs*. In Mode *Sb*, combination of these are applied, and *SEs* and *BSEs* are successfully detected (Figure 3d).

Schematic diagram and typical trajectories of an electrons for JSM-7100F TTL/7800F are shown in Figures 3e and f, respectively. Without strong electrostatic field between a magnetic lens and a substrate generated by substrate bias, trajectory of *BSEs* are rather straight, which makes most *BSEs* not going into *SEM* column (Figure 3e). Thus, a conventional high efficiency *BSE* detector (*BED*) should be placed between a substrate and a magnetic lens (Figure 3e), making both the working distance and the focal length long, and degrading the diameter of *PE*. When a bias voltage is applied to the specimen substrate, an electrostatic field is produced between the magnetic lens and substrate (bi-potential lens), allowing the diameter of *PE* to be small even at low landing energy, as described above. In addition, the substrate bias changes trajectory of *BSE*: trajectory is almost parabolic near the substrate, and directions of *BSEs* are modified to upwards, making them go into the *SEM* column (Figure 3f). Furthermore, these *BSEs* are accelerated by the electric field, which makes detection of these *BSEs* easy. These enable detection of *BSEs* inside the column with a shorter working distance and a small diameter of *PE* even at low landing energy of

impact electrons as well as the effect of electromagnetic lens. Thus we have overcome traditional problems in *BSE* image. Since JSM-7800F has energy filter inside *SEM* column, simultaneous detection of *BSE* and *SE* is possible (Figure 3e and f). This simultaneous imaging is especially valuable for electron beam sensitive materials, mixed phases / compounds with characteristic nano-feature and different composition and so on.

Here we describe the recent experimental results obtained by JSM-7401F/7600F and JSM-7100F TTL/7800F with specimen bias (Gentle Beam (GB) mode).

Electron beam damage and fine structures from electron beam sensitive materials (Zeolites, meso-zeolite LTA & MOF)

a) SEM and atomic force microscopy (AFM) images of STA-7 and LTA.

Crystal surfaces of two zeotype crystals, LTA and STA-7, were oriented orthogonally with respect to the electron-optic axis of the *SEM* and irradiated with an electron probe of various doses and energies using JSM-7401F. [8] This produced rectangular areas of contrast, corresponding to the scanned area of interest, when viewed from a lower magnification (**Figure 4c**) that were absent before irradiation (Figure 4b). The rectangular areas were analyzed *ibidem* (in the same place) by atomic force microscopy (*AFM*). Areas with very low electron exposure possess a rectangular contrast in the *SEM* but exhibit a zero height depression as measured by *AFM*. This establishes that contrast from contamination, another contributor to loss of information in a *SEM* image, is still present even at nondestructive electron doses. The depth increased with increasing time of electron exposure and increasing probe current to an eventual maximum depression of just under 20 and 15 nm for STA-7 and LTA, respectively, with the former crystals exhibiting a more rapid collapse (Figure 4a, d, and e). In both materials, the nanometer surface terraces are preserved with no discernible distortion in the irradiated area (Figure 4g-j). Figure 4i and j illustrates how the *AFM* cross section in Figure 4g and h is the result of translation of the surface in a direction orthogonal to the crystal face.

The measured step heights within the damaged area differ by less than 5% (i.e., within the precision limit of the *AFM*) when compared to the step heights outside of the damaged area. The lack of distortion of the crystal surface, when measured by *AFM*, is therefore surprising. This implies that the area of the crystal experiencing crystalline-amorphous (*C-A*) transitions is sufficiently below the surface to leave it geometrically unaltered. *SEs* contribute to topographic contrast in the *SEM* as their escape depth is no more than 10 nm. The majority of impact electrons penetrate much deeper into the interaction volume. The inelastic collisions are responsible for the *C-A* transitions, and because they occur mainly at sufficient depth, the surface remains chemically and structurally intact.

b) Meso LTA (at different impact energies)

In recent years, zeolite crystallization studies were

Dependence of SEM image on specimen bias

Landing voltage = 500 V

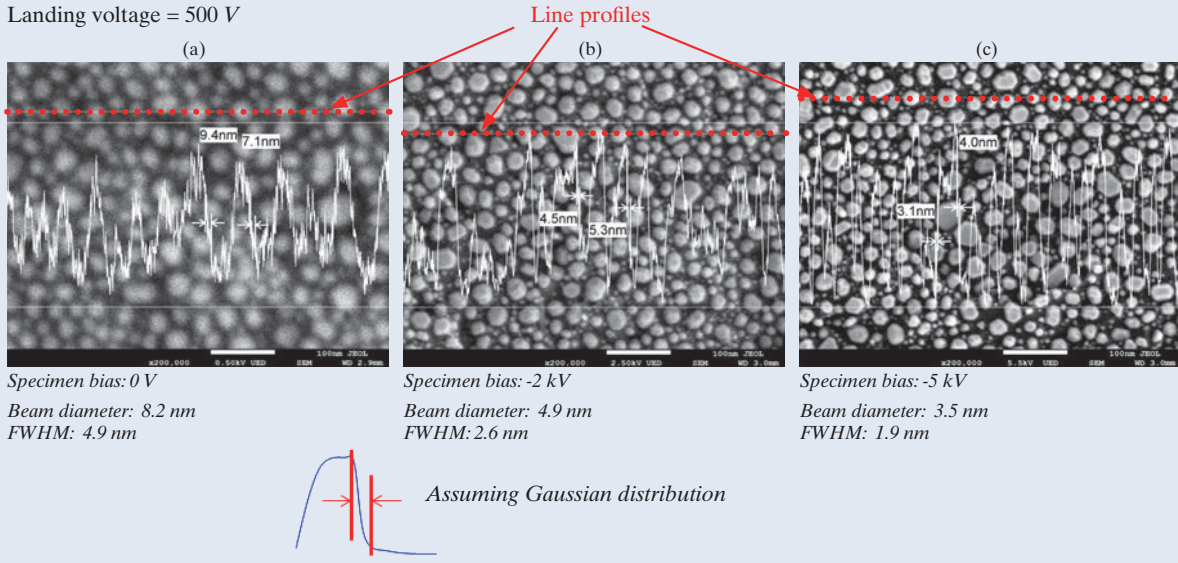


Fig. 2 SEM resolution dependency on substrate bias. With increasing substrate bias from 0V (a) to -5 kV (c), resolution improves. These images are taken using JSM-7800F with GBSH (Gentle Beam Super High resolution) option allowing specimen bias (absolute value) up to -5 kV.

Schematic diagrams and typical trajectories of SEs and BSEs for JSM-7401F/4600F and JSM-7100FTTL/7800F

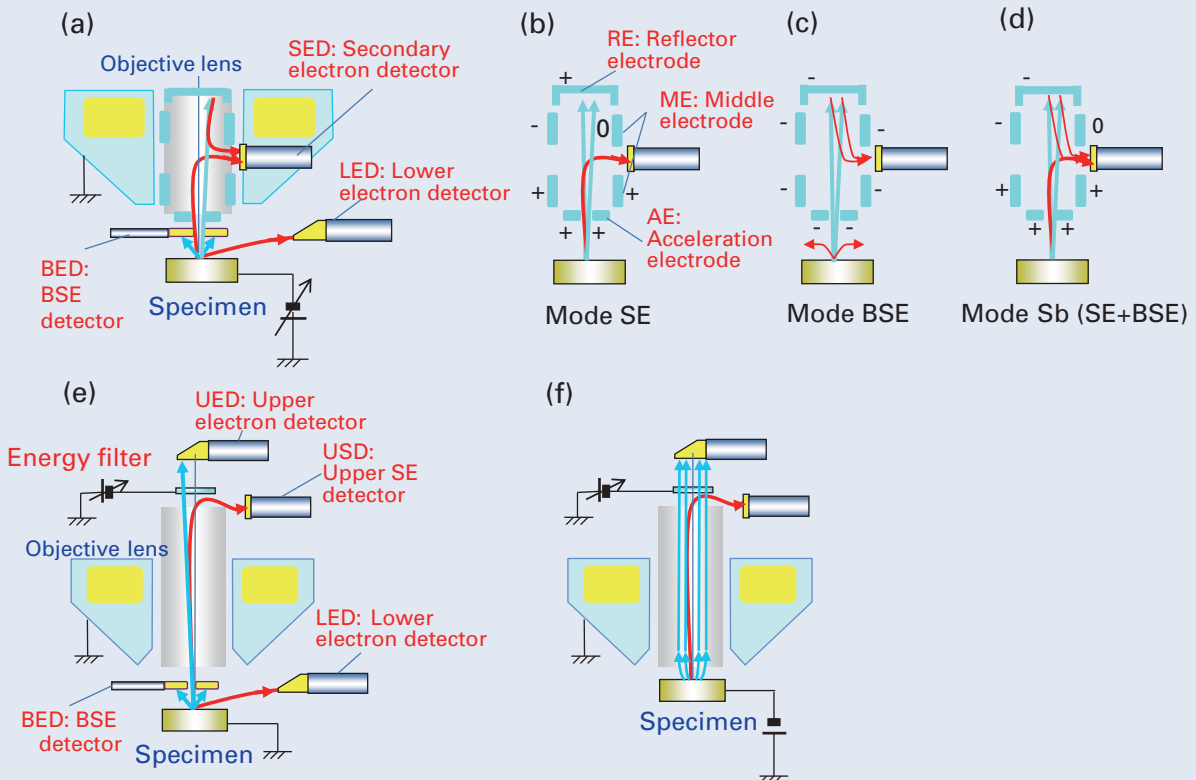


Fig. 3 Schematic diagram and the typical trajectories of SEs and BSEs for JSM-7401F/7600F (a-d) and JSM-7100F/7800F (e, f). SEs and BSEs are selectively detected using electrodes or energy filter.

AFM study of nanoscale e-beam damage under HRSEM observation

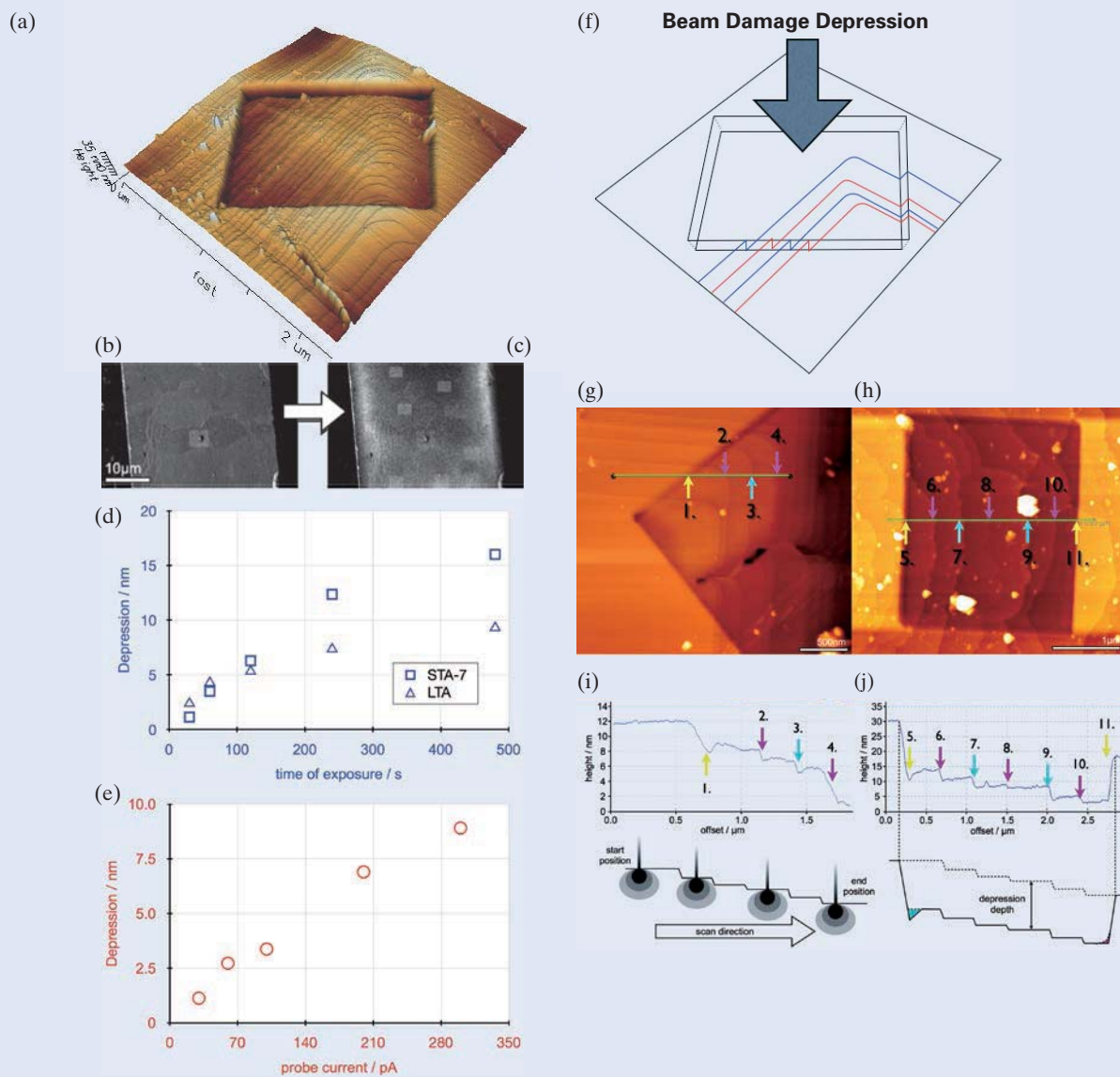


Fig. 4 AFM study of nanoscale e-beam damage under HRSEM observation. AFM image after HRSEM observation (a) and schematic drawing (f). Low magnification SEM image before (b) and after (c) HRSEM observation. Depression of a surface by e-beam damage depending on time of exposure (d) and depending on probe current (e). Depression of a surface depending on various conditions (g-j).

E-beam damage comparison at extreme low voltage on mesoporous LTA

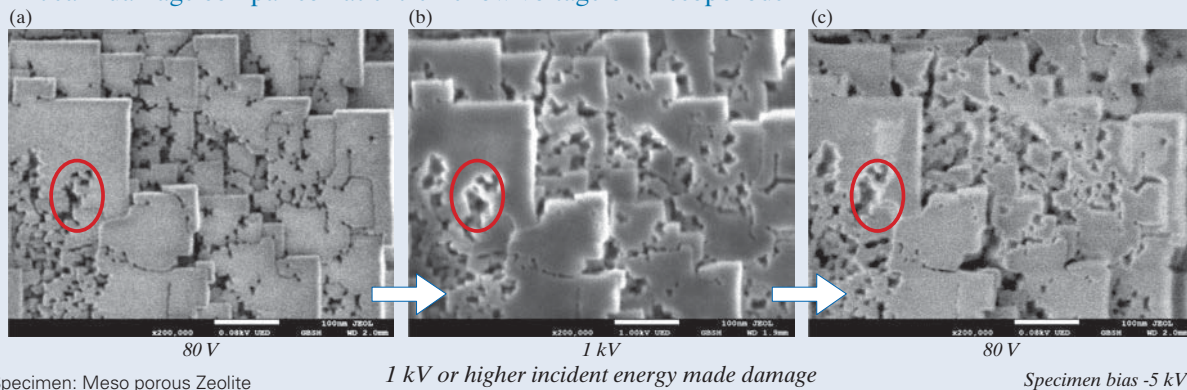


Fig. 5 E-beam damage comparison at extreme low voltage on mesoporous LTA. SEM image taken at extreme low landing voltage of 80 V before observation at 1 kV (a), SEM image taken with landing voltage of 1 kV (b), and SEM image at landing voltage of 80 V after observation at 1 kV. Specimen bias of -5 kV allows high resolution images even at landing voltage of 80 V.

mostly focused on nanocrystalline zeolites with particle diameters less than 50 nm and hierarchically porous, micro-, meso- and macro-porous zeolites. LTA zeolite with mesopores was successfully synthesised by Ryong Ryoo's group under a hydrothermal synthesis condition that contained a quaternary ammonium-type organosilane surfactant and their mesopore architectures were reported previously by *LV-HRSEM* combined with Cross-section polisher (*CP*) sectioning [9]. The *HRSEM* investigation revealed presence of a disordered network of mesoporous channels that penetrated the microporous zeolite crystal. Here we show the effect of electron beam energy on damage at very low landing energies. **Figure 5a, b and c** were taken in sequence with time at landing voltage of 80 V, 1 kV and 80 V, respectively. Especially, the image of 80 V shows less edge effect due to small interaction volume. That is a good feature of low voltage *HRSEM* (*LV-HRSEM*), because it shows fine edges and gives highly accurate measurement of nano porous materials. Moreover, there are damages due to electron beam irradiation as large gap on the Figure 5b, which are indicated with circle. On the other hand, Figure 5a and c show no or less damages by electron beam.

These clearly show the importance of using low landing energy for electron beam sensitive materials.

c) IRMOF-74

Isorecticular series of MOF-74 structures (termed IRMOF-74-I to XI) with pore apertures ranging from 1.4 to 9.8 nm has been successfully synthesised by Omar Yaghi's group [10]. When unit-cell size of crystals become larger, it becomes hard to obtain even unit cell parameters by powder X-ray diffraction (*XRD*) patterns because of serious overlap of reflections and sever damping of intensity with

increase of scattering vectors. Furthermore confirmation of non-existence of surface barrier is becoming important to utilise the pores of materials. **Figure 6a** is schematic drawing of IRMOF-74-VII and **Figure 6b** shows *TEM* image. A JEM-2010F field emission *TEM* equipped with a CEOS post-specimen spherical aberration corrector (Cs corrector) was operated at 120 kV for high-resolution transmission electron microscopy (*HRTEM*) imaging. Since MOF materials are electron beam sensitive, the electron beam damage to the specimen was minimized as much as possible (in this study, the beam density during the observations was from 50 to 130 electrons/(nm²)). A single *HRTEM* image with an exposure time of 2 seconds or a sequence of images (10 frames) was recorded, with a 0.5 second exposure time for each frame and after drift compensation, some frames can be superimposed to increase the signal-to-noise ratio (*S/N*) for display.

Figure 6c was taken from IRMOF-74-VII at landing voltage of electron 300 V (Acceleration voltage = 5.3 kV, the specimen bias = - 5.0 kV, Beam current = 2.0 pA), and showed clearly pores with diameter of ~ 3.5 nm and hexagonal arrangement of them. A substrate bias of -5.0 kV was achieved with newly developed *GBSH* (Gentle Beam Super High resolution) option for JSM-7800F.

As the MOFs and Zeolite research expand more and more to nano scale, utilisation of *EM* method becomes imperative, since *XRD* on crystals of nano size will not be sufficient to characterise their structures any more. So the *EM* method plays important roles in characterisation of Zeolites and MOFs that has at least one dimension fall into nano scale. These include nano particles, nano rods, nano ribbons, nano sheet, nano films, to just name a few. As the resolution of *EM* methods improves, more structural detail can be observed in the crystals of MOFs and Zeolites. The evolution of *EM* technology will

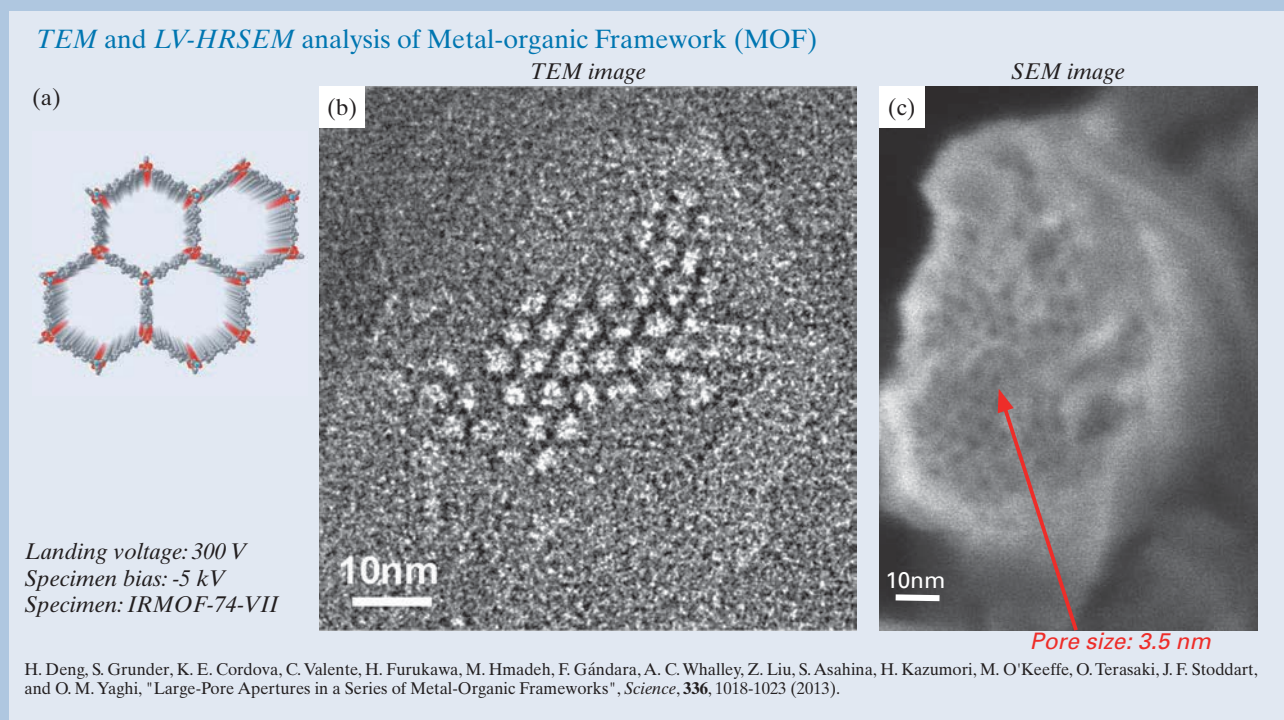


Fig. 6 Analysis of Metal-organic Framework (MOF). Schematic drawing (a), *TEM* image (b), and *SEM* image (c) of MOF. Pores with diameter of 3.5 nm are clearly observed in *TEM* image (b) and *SEM* image (c).

definitely change the way of traditional characterisation of materials where only space average of the crystal lattice counts, but rather by providing direct and real time view of a crystal surface with a few nanometer thickness. In short, *EM* methods are 1. good for nano sized MOF; 2. good for structural details; and 3. provide dynamic information.

Improved LV-HRSEM images

(a) Helical TiO_2

Very recently, chiral TiO_2 nanofibres with electron transition-based optical activity have been synthesised by Shunai Che's group by the transcription of the helical structure of amino acid-derived amphiphile lipid enantiomers through coordination bonding interactions. The as-prepared lipid- TiO_2 hybrid was exclusively composed of right/left-handed double-helical amorphous TiO_2 fibres with $\sim 25 \text{ nm}$ in width and $\sim 100 \text{ nm}$ pitch length along the fibre axis and the fibres possess inner tubular structures with diameter of $\sim 12 \text{ nm}$ along their central axes. The chemical composition and the structure made the *SEM* observation of such material very difficult. To reduce

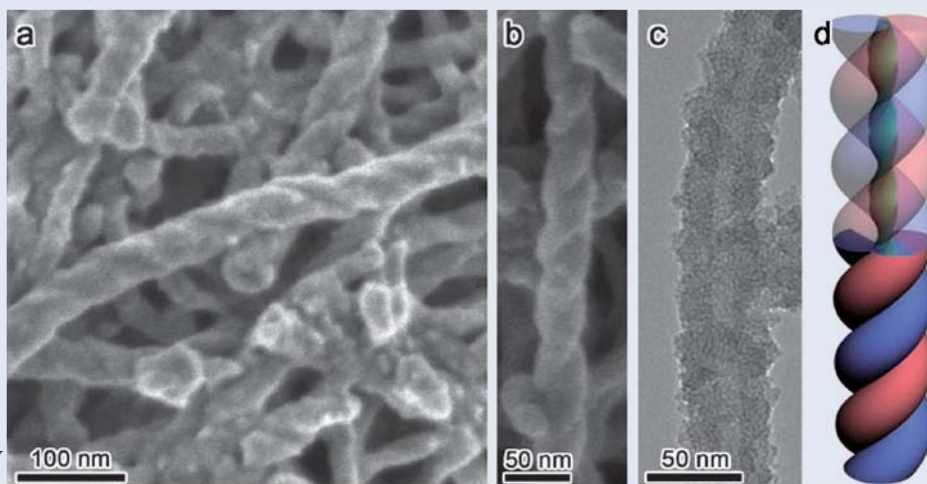
the probe size and the interaction volume to achieve high resolution, 0.5 kV landing voltage with -2.0 kV bias voltage applied to the specimen substrate and a short working distance of 3.0 mm were used and the detail morphology of the fibres were nicely revealed (**Figure 7a** and **b**). The *HRTEM* image and the corresponding model are shown in **Figure 7c** and **d**, respectively.

The as-prepared amorphous hybrids can be converted to crystalline TiO_2 with stacks of anatase nanocrystals with of $\sim 20 \text{ nm}$ size by calcination, which is shown in **Figure 7e**. Compared to as-prepared sample, higher landing voltage of 1.0 kV with -2.0 kV bias voltage and a shorter working distance of 2.6 mm were used. **Figure 7f** shows a *HRTEM* image of an array of nanocrystals exhibits the contrast close to $\langle 111 \rangle$ zone axis of the anatase structure, particularly, the adjacent nanocrystals have a rotational misplaced arrangement, piling up by sharing one of their $\{101\}$ facets while keeping one of the $\langle 111 \rangle$ axis in common, leading to a helical array of nanocrystals with almost parallel $\langle 111 \rangle$ axes (**Figure 7g**). However, it is very difficult to determine the structural relationship of all the nanocrystals due to the overlapping problem and the small crystal size.

TEM and LV-HRSEM analysis of Helical TiO_2

LV-HRSEM
for as synthesised

Landing voltage: 0.5 kV
Specimen bias: -2 kV



LV-HRSEM
for as calcined

Landing voltage: 1 kV
Specimen bias: -2 kV

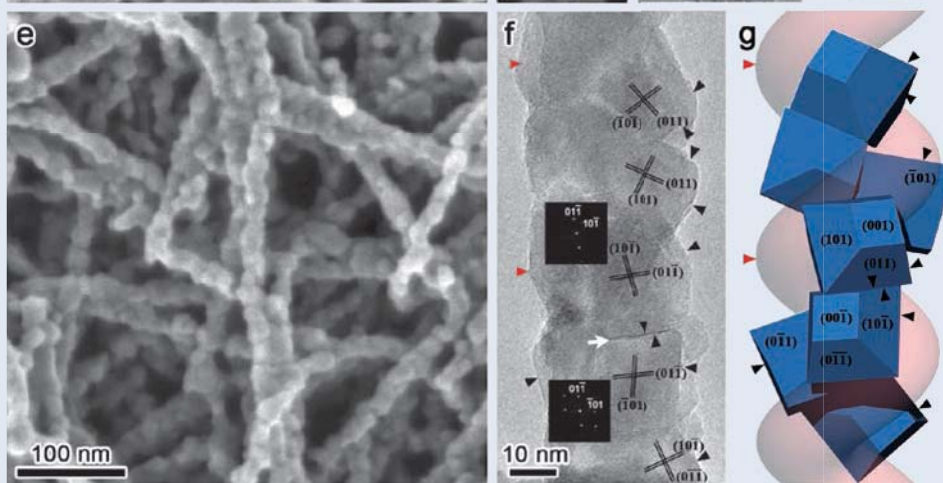


Fig. 7 *LV-HRSEM* images taken with landing voltage of 0.5 kV with the specimen bias of -2.0 kV (**a** & **b**), *HRTEM* image (**c**) taken at 200 kV and the schematic drawing (**d**) of the as-prepared organic lipid- TiO_2 hybrid fibres; The *LV-HRSEM* image taken with landing voltage of 1.0 kV with the specimen bias of -2.0 kV (**e**), *HRTEM* image taken at 200 kV (**f**) and the schematic drawing (**g**) of calcined chiral crystalline TiO_2 .

From these results, we may suggest that the crystallization process is formed locally according to the initially formed double-helical structures while generally retained the double-helical morphology of the as-prepared samples, however, the hollow tubular structures disappeared. Both the amorphous and anatase crystalline helical TiO_2 fibres exhibited optical response to circularly polarized light at the absorption edge around $\sim 350 \text{ nm}$. This was attributed to the semiconductor TiO_2 -based electronic transitions from the valence band to the conduction band under an asymmetric electric field [11].

(b) Porous crystals with different length scales (SBA-15)

Mesoporous silica crystal, SBA-15, has $2d$ -hexagonally arranged primary mesopores (channels) with plane group $p6mm$. The crystal has a highly complex porosity with, in addition to the main mesopores, unordered pores penetrating the amorphous silica wall. These intrawall pores have a broad size distribution, from micropores to small mesopores. As a consequence of the formation sequence, the main mesopores contain to varying degree

“plugs” that may or may not seal the mesopore to the exterior, i.e. the mesopores may not be accessible to chemical reagents or probing gas molecules. Although nitrogen sorption generally provides valuable information on the porous character of mesoporous materials it is only by direct observation that detailed information on the porosity can be unveiled. To be able to understand the growth process, gas adsorption/ desorption processes and to be able to efficiently functionalize the pore walls there is a need to properly characterize these complicated structures, including pore openings and the accessibility. In order to observe *HRSEM* image of electric non-conductive silica mesoporous crystals free from the electron-charging problem, we need to use *LV-HRSEM* by improving its resolving power in low impact energy as mentioned before. [12] *SE* images are taken exactly same area at specimen bias $= -2 \text{ kV}$ and -5 kV keeping both landing voltage 300 V and beam current 5.5 pA , are shown in **Figure 8a** and b. It is clear that resolution and *S/N* are greatly improved by increasing bias voltage. Micropores in channel walls as well as plugs inside channels are observed in Figure 8c. Contaminations on the sample accumulated during observation were successfully removed by Ar-ion

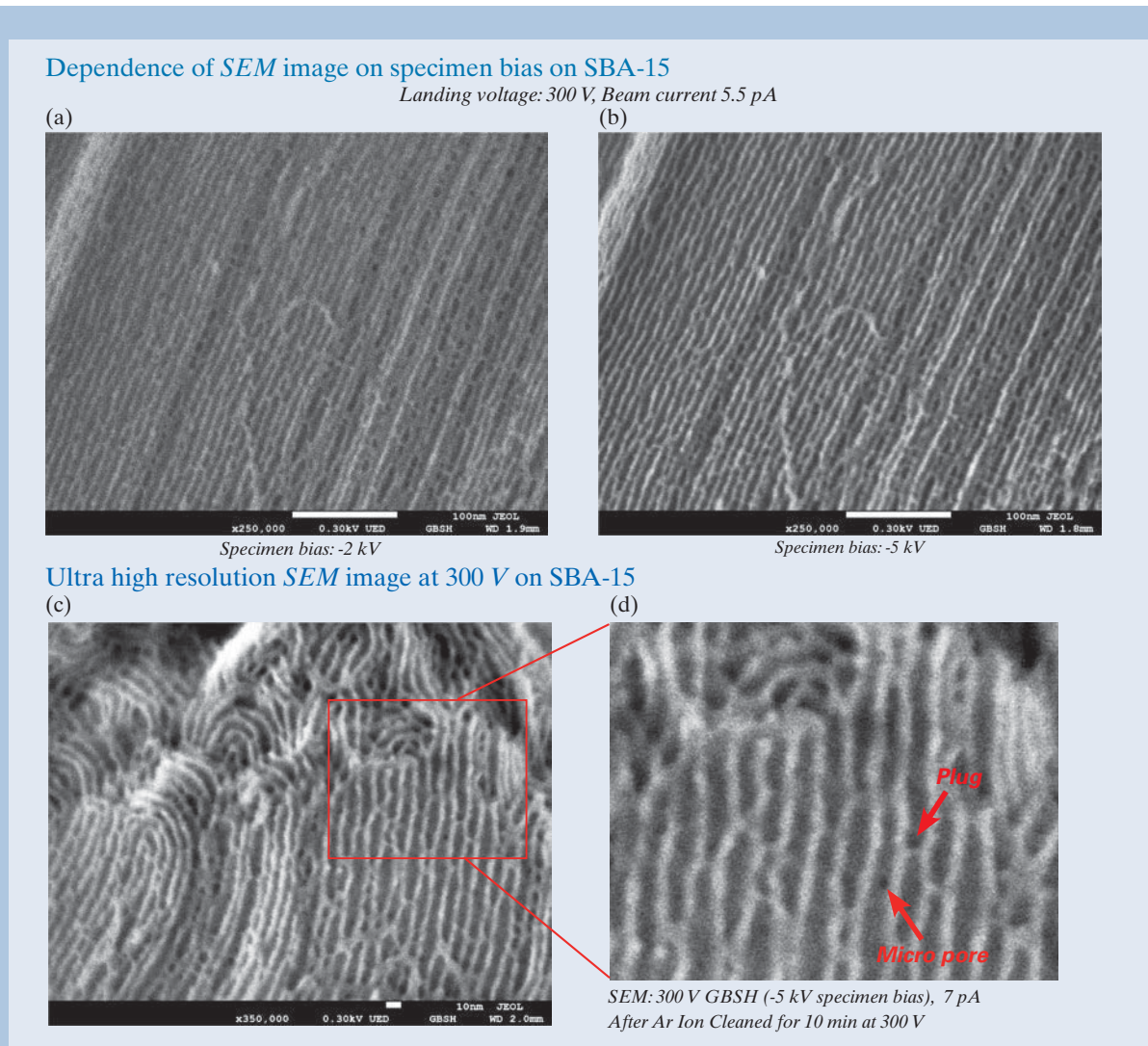


Fig. 8 SEM images of SBA-15 at landing voltage of 300 V. Specimen bias of -2 kV (a) and -5 kV (b-d). Increase of specimen bias voltage (absolute value) improves both resolution and *S/N* of *SE* image of SBA-15 (a, b). Micropores are clearly observed (c, d).

as shown in Figure 8d.

(c) Gold yolk-shell materials, Au@TiO₂, Au@ZrO₂ and Au@C

Gold yolk-shell materials, Au@TiO₂, Au@ZrO₂ and Au@C, have been synthesised through nanocasting of Au nanoparticles in TiO₂, ZrO₂ and Carbon spherical shells with

pores via silica route, that is Au@SiO₂@X (where X=TiO₂, ZrO₂ and Carbon) and SiO₂ core is selectively removed with aqueous NaOH. This structure allows efficient stabilization of the metallic cores at high temperature conditions, while maintaining high catalytic activity through not only intrinsic catalytic activity of gold nanoparticles but also supports. The high structurally and compositionally defined yolk-shell particles make these kinds of material ideally suited by discriminating effects of support and particle-size for

Nano Structural analysis using TEM on Au@TiO₂

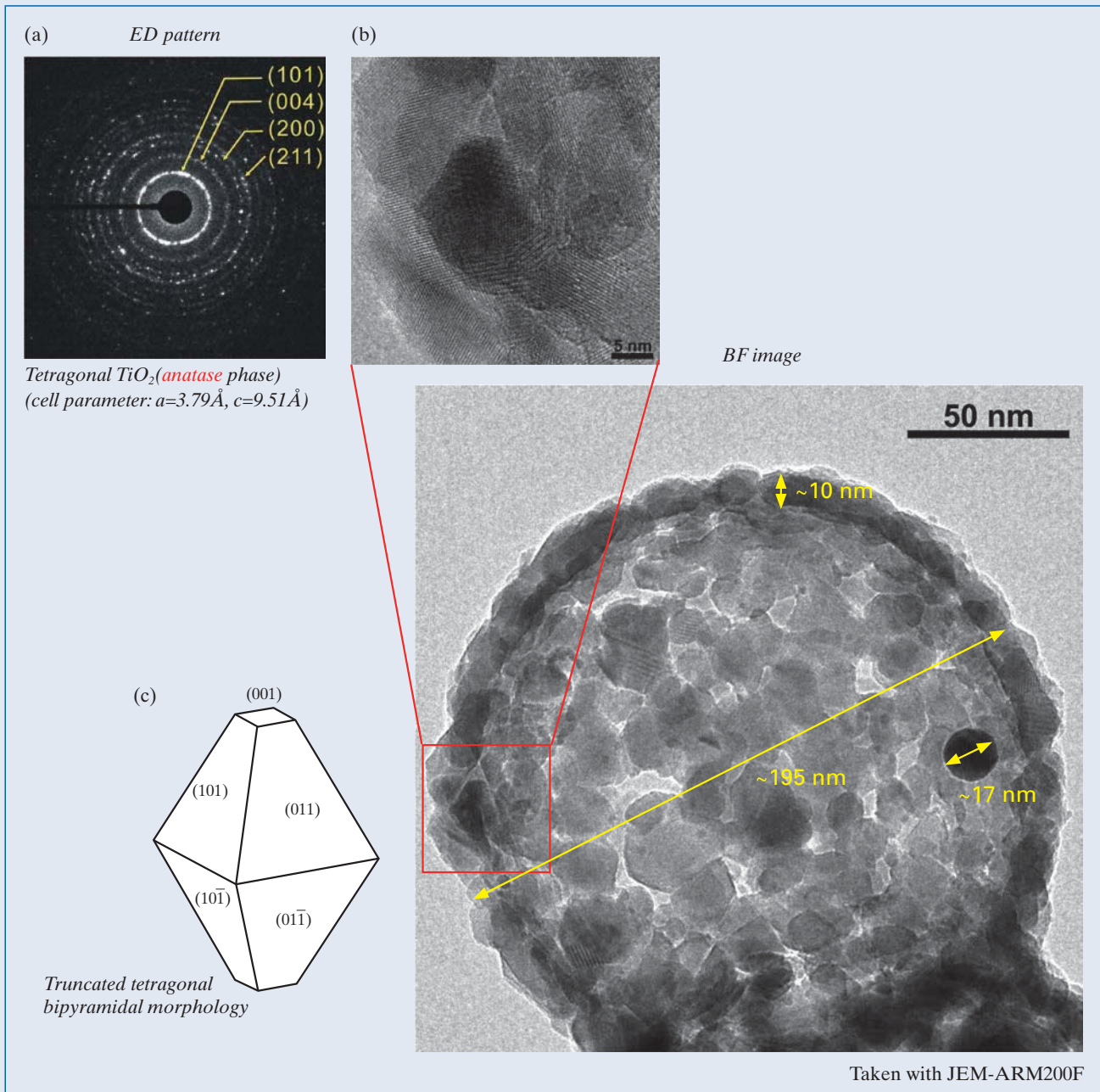


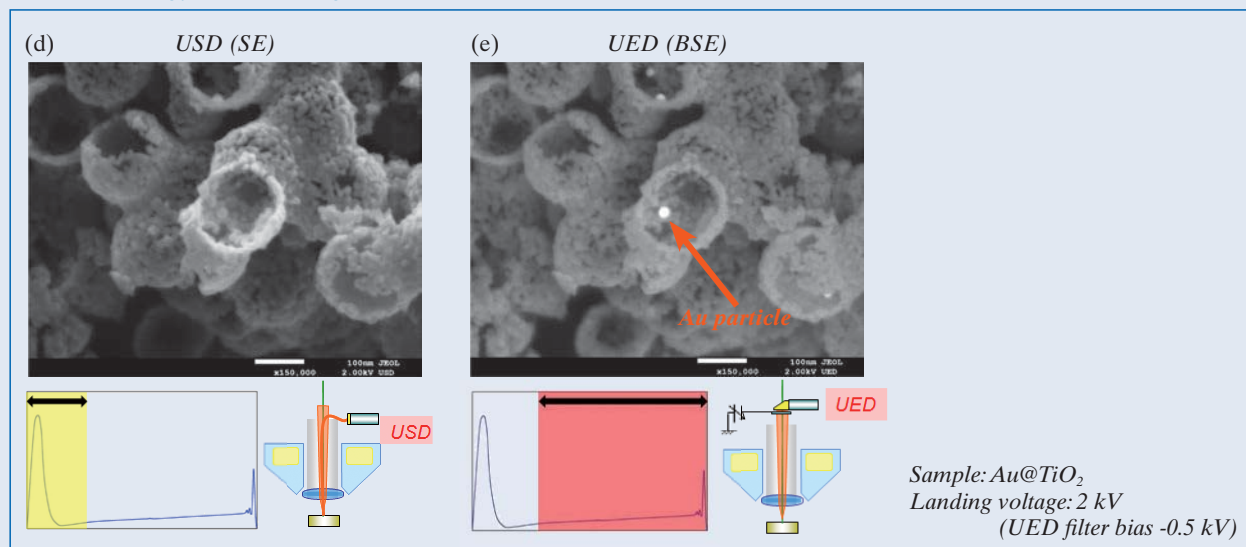
Fig. 9 Au@TiO₂, Nano Structural analysis using TEM on Au@TiO₂ (a-c), electron energy filtered SEM images providing mainly SE (d) and BSE (e) information, improved resolution of BSE with sample bias (f-h).

mechanistic studies in heterogeneous catalysis [13]. Here results only on Au@TiO₂ are shown. Electron diffraction (ED) pattern and high resolution TEM bright field (BF) image taken with JEM-ARM200F are shown in **Figure 9a** and **b**. These show that TiO₂ is anatase structure, TiO₂ crystal sometime shows nice truncated tetragonal bipyramidal morphology, and that gold particle has spherical shape with diameter *ca* 17 nm (multiply twined particles are also found in other york-shells).

Electron energy filtered images are taken from Au@TiO₂ at electron landing voltage= 2 kV. USD and UED collect electrons with low and high energy, corresponding mostly to SEs, and BSEs, respectively, when UED energy filter bias is set at - 500 V. We can obtain images simultaneously by USD and UED, and can confirm that USD gives topological contrast while UED gives Z contrast.

It is confirmed as expected that resolution of BSEs

Electron energy filtered images Au@TiO₂



GB mode improves spatial resolution for LV-BSE

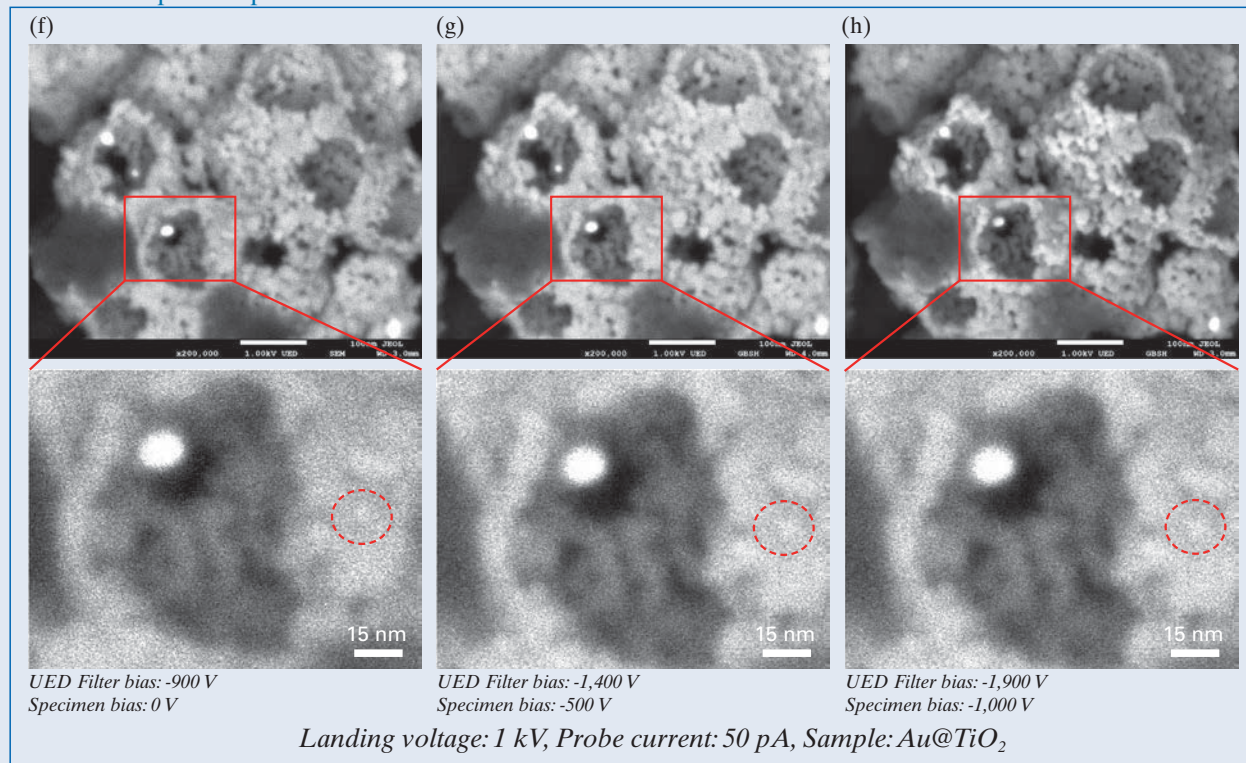


image obtained with *UED* is improved by loading specimen bias keeping landing voltage and beam current constant (1 kV and 50 pA, respectively) Figure 9f-h.

BSE image (Figure 10a) and *EDS* mappings (Figure 10b and c) are shown. Resolution of *EDS* mapping is greatly improved by placing specimen bias from 0 (Figure 10b) to -5 kV (Figure 10c) at landing voltage of 4 kV. Resolution of *EDS* mapping is usually dominated by signal generation volume, but in this case, diameter of *PE* affects resolution.

Conclusion and future progress

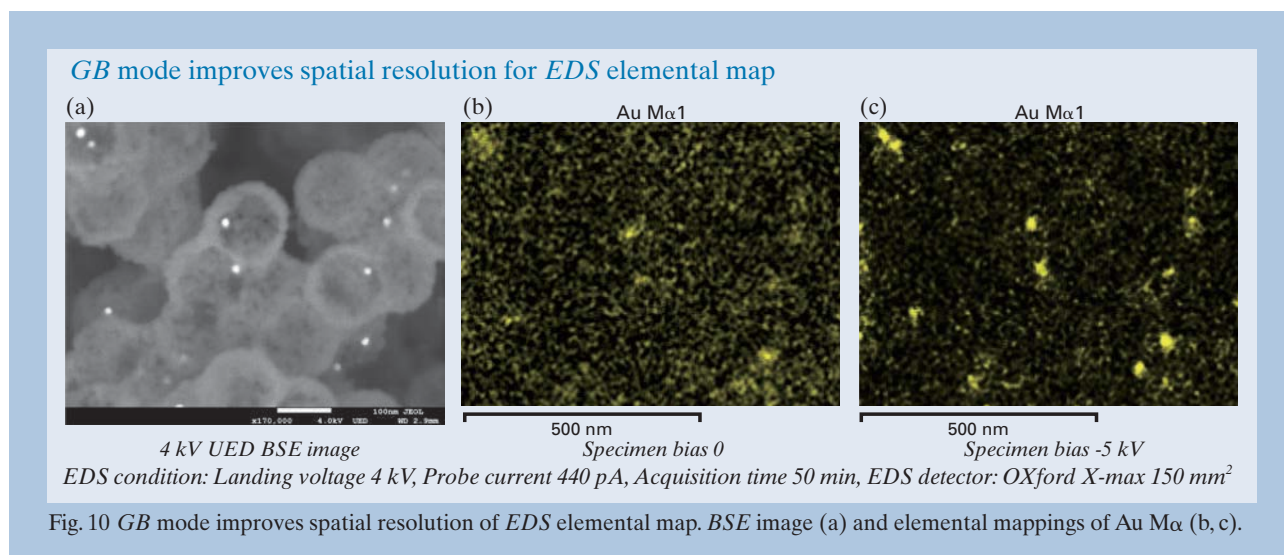
Since our last publication in *JEOL News* [1] on high resolution scanning electron microscopy we have seen limitations broken in the resolution of both topographic and compositional information. Whereas previous breakthroughs were down to computer aided design, this time, that design has been directed towards more optimum combinations of electric and magnetic lenses facilitating further progress. However, there is no direct indication that current configurations and associated conditions and parameters have reached a universally recognised minima. There are many other exciting advances through use of ultra low energy work done, the high energy work done on thin samples and low-loss energy electrons (plasmon-loss).

Acknowledgments

Financial support from VR & Knut Alice Wallenberg Foundation and EXSELENT (Sweden), JST (Japan), WCU (R-31-2008-000-10055-0) and IBS (Korea) are acknowledged.

References

- [1] Stevens et al., *JEOL News* & Liu et al. A review of fine structures of nanoporous materials as evidenced by microscopic methods. *J Electron Microscopy* **vol. 62** pp.109-145 (2013).
- [2] Asahina et al. A new HRSEM approach to observe fine structures of novel nanostructured materials. *Mesoporous and Microporous Materials* **vol. 146** pp. 11-17 (2011).
- [3] Seiler, Secondary electron emission in the scanning electron microscope, *Journal of Applied Physics* **vol. 54** pp. R1-R18 (1983).
- [4] J. Cazaux. About the role of the various types of secondary electrons (SE1; SE2; SE3) on the performance of LVSEM, *Journal of Microscopy* (2004) vol. 214 pp. 341-347.
- [5] Paden and Nixon, Retarding field scanning electron microscopy. *J. of Scientific Instruments* **vol. 1** p.1073 (1968).
- [6] Yau et al. Generation and applications of finely focused beams of low-energy electrons. *Journal of Vacuum Science and Technology* **vol.19** pp.048-1052 (1981).
- [7] Frosien et al. Compound magnetic and electrostatic lenses for low-voltage applications. *International symposium on electron, ion, and photon beams* **vol. 7** pp.1874-1877 (1989); Yonezawa et al. Single pole-piece objective lens with electrostatic bipotential lens for SEM. *Journal of Electron Microscopy* **vol. 51** pp.149-156 (2002); Khurshed, A. Ultimate resolution limits for scanning electron microscope immersion objective lenses. *Optik - International Journal for Light and Electron Optics* **vol. 113** pp.67-77 (2002).
- [8] Stevens et al. Nanoscale Electron Beam Damage Studied by Atomic Force Microscopy. *J. Phys. Chem.* **vol. C113** pp. 18441-18443 (2009).
- [9] Cho et al. Mesopore generation by organosilane surfactant during LTA zeolite crystallization investigated by high-resolution SEM and Monte Carlo simulation. *Solid State Sciences* **vol. 13** pp. 750-756 (2011).
- [10] Deng et al. Large pore apertures in a series of metal-organic frameworks. *Science* **vol. 336** pp. 1018-1023 (2012).
- [11] Liu, S. et al. Synthesis of chiral TiO₂ nanofibre with electron transition-based optical activity. *Nat. Comms.* **vol. 3**, p.1215 (2012).
- [12] Kjellman et al. Independent fine-tuning of the intrawall porosity and primary mesoporosity of SBA-15, *Chem Mat* **vol 25**, pp1989-1997., and Kjellman et al. submitted (2013).
- [13] C. Galeano et al. Yolk-Shell Gold Nanoparticles as Model Materials for Support-Effect Studies in Heterogeneous Catalysis: Au, @C and Au, @ZrO₂ for CO Oxidation as an Example. *Chem. Eur. J.* **vol.17** pp.8434-8439 (2011).



Effects of *l*-menthol on the Thermotropic Characteristics of Intercellular Lipid in the Hairless Rat Stratum Corneum Evaluated by Differential Scanning Calorimetry and Electron Spin Resonance

Yasuko Obata, Hiroshi Watanabe, Daigo Hoshino
and Koza Takayama

Hoshi University

Transdermal absorption enhancers (e.g., *l*-menthol) act on intercellular lipid in the stratum corneum (SC), although the detailed mechanism of action of *l*-menthol on intercellular lipid is unclear. Using differential scanning calorimetry and electron spin resonance (ESR) to evaluate the promoting mechanisms of *l*-menthol, we focused on the effects of *l*-menthol on the microviscosity of intercellular lipid in the SC. Treatment with *l*-menthol significantly decreased the transition temperatures of the microstructure of intercellular lipid in the SC. ESR measurements using two kinds of spin-label reagent, 5- and 16-doxyl stearic acid (5- and 16-DSA) showed that *l*-menthol at physiological temperatures decreased the rotational correlation time (τ) of 5-DSA and that the flexion point shifted to the lower temperature. *l*-Menthol decreased the τ value of 16-DSA at ambient temperature. These data suggest that *l*-menthol reduces the microviscosity of the hydrophobic region in intercellular lipid in the SC, an effect caused by the disruption of the microstructure of intercellular lipid. In conclusion, *l*-menthol fluidizes the polar and hydrophobic region of intercellular lipid in the SC. These data might provide useful information for the development of effective transdermal formulations.

Introduction

The stratum corneum (SC), the outermost layer of the skin, performs a vital function as a barrier against foreign stimuli e.g., viruses, bacteria, ultraviolet light, and drying. The SC structure can be described by the “bricks and mortar” model, in which corneocytes are embedded in a lamellar lipid matrix [1]. The corneocytes correspond to the bricks and lipids act as mortar to fill the intercellular space. Even though it comprises only a small portion of the SC, intercellular lipid plays an important role by providing the barrier function of the skin. The major components of intercellular lipid in the SC are ceramides, cholesterol, free fatty acids and these derivatives of three components [2,3]. Ceramides compose about 50% of the total intercellular lipid mass. Human SC includes 11 structurally heterogeneous types of ceramides, termed ceramide 1 to 11 [4]. Cholesterol comprises about 25% and fatty acids comprise about 10% of the total lipid mass in the SC.

The lipid microstructure and the molecular

arrangement of intercellular lipid in the SC has been investigated using synchrotron X-ray scattering and neutron diffraction [5-7]. Two kinds of lamellar structure are observed by small-angle X-ray scattering and neutron diffraction. One is a short lamellar structure with a repeat distance of about 6 nm, and the other is a long lamellar structure with a repeat distance thought to be about 13 nm [6,8]. Hydrocarbon chain packing is observed by wide-angle X-ray scattering, and a lattice distance of about 0.42 nm and orthorhombic packing with lattice distances of about 0.42 and 0.37 nm have been observed [9]. These microstructures of intercellular lipid in the SC relate to the barrier function of the skin. To improve drug absorption via the skin, it is necessary to disturb gently the microstructures of intercellular lipids in the SC.

The most widely used approach to improve transdermal drug absorption involves chemical absorption enhancers, including the cyclic monoterpenes [10-13]. Although the mechanism responsible for this enhancement effect has not been clarified, the fluidizing effect of cyclic monoterpenes on intercellular lipid in the SC is thought to be a crucial factor [14,15]. We used Fourier transform infrared spectroscopy to observe the conformational disorder of intercellular lipids in the SC induced by treatment

Ebara 2-4-41, Shinagawa, Tokyo 142-8501, Japan

E-mail: obata@hoshi.ac.jp

with *l*-menthol, one of the most commonly used cyclic monoterpenes [16]. Using electron spin resonance (ESR) spectroscopy, Anjos et al. also reported that terpenes, including *l*-menthol, disrupt the hydrogen bond network of the polar head groups in intercellular lipid in the SC [17,18]. Understanding this effect of *l*-menthol at the molecular and structural levels requires further study.

ESR spectroscopy is a useful methodology for evaluating the microviscosity of intercellular lipids in the SC and *l*-menthol-induced changes in intercellular lipid at the molecular level. The ESR spectrum of spin-labeled fatty acids is highly sensitive to the motional properties of the spin-label reagents, permitting one to monitor the changes that occur in intercellular lipid in the SC in response to added drugs [19-21]. The ESR technique provides an efficient tool for distinguishing the fluidizing effect of transdermal absorption enhancers. We used differential scanning calorimetry (DSC) and ESR measurements to investigate the effects of *l*-menthol on the thermotropic behavior of the SC and on the hydrophobic and polar domains of intercellular lipid in the SC.

Experimental

Chemicals

l-Menthol was purchased from Tokyo Chemical Industries Co. Ltd. (Tokyo, Japan). Ethanol and trypsin were purchased from Wako Pure Chemical (Tokyo, Japan). The spin-labeled derivatives of stearic acid, 5- and 16-doxyl stearic acid (5-DSA and 16-DSA), were purchased from Sigma-Aldrich (St. Louis, MO, USA). Other chemicals used were reagent grade.

Preparation of the SC sheet

The hairless rat SC was separated from the excised abdominal region of hairless rats (HWY/Slc, 12 weeks old, Sankyo Labo Service, Tokyo, Japan) by digestion with 0.1% trypsin in phosphate-buffered saline (pH 7.4) at 37 °C for 24 h. The separated SC was rinsed in purified water and dried *in vacuo*. The procedures involving animals and their care complied with the regulations of the Committee on Ethics in the Care and Use of Laboratory Animals of Hoshi University.

DSC measurements

The SC was incubated in purified water or penetration enhancer solution (40% ethanol, 1% *l*-menthol in 40% ethanol) for 2 h at ambient temperature and dried under a stream of nitrogen until it reached an acceptable predetermined weight (125% of the weight before treatment). DSC measurements were performed using a Thermo plus DSC-8230 instrument (Rigaku Co., Tokyo, Japan) with heating scans at the rate of 10 °C/min. The samples were placed in an aluminum pan (Rigaku Co.). The transition temperature was determined as the peak of the endothermic transition profiles.

ESR measurements

The dried SC sheet was incubated in 10 mM spin-

label reagent (5- or 16-DSA) having the nitroxide radical moiety (doxyl) in the 5th or 16th carbon atom of the acyl chain, in 40% ethanol or 1% *l*-menthol in 40% ethanol solution for 2 h at 37 °C. After the spin labeling, the excess spin label was washed out using 40% ethanol solution. The prepared SC sheet was introduced into the capillary tube for the ESR measurements.

ESR measurements were performed using a JES-FA200 spectrometer (JEOL, Tokyo, Japan). ESR measurement conditions were microwave frequency of 9.07 GHz, microwave power of 5.0 mW, modulation width of 1.2×0.1 mT, magnetic field of 325 ± 5 mT, sweep time of 30 s and time constant of 30 ms. The temperature of the SC was controlled from 20 to 70 °C at the rate of about 2.5 °C/min using ES-DVT4. The rotational correlation time τ (ns) was calculated from the obtained ESR spectra based on equation appeared in the reference [22].

Statistical analysis

Each value is expressed as the mean \pm S.D. For group comparisons, a one-way layout analysis of variance (ANOVA) and Student's *t* test were used to analyze the data. *P* values less than 0.05 were considered significant.

Results

Effects of *l*-menthol on the thermotropic behavior of the hairless rat SC

The distinct changes in the thermotropic behavior of the hairless rat SC induced by the treatment with *l*-menthol are shown in **Fig. 1**. The intact SC showed three endothermic phase transitions near 39 °C, 54 °C, and 66 °C (Fig. 1(a)). These endothermic peaks in the profiles were shifted to a lower temperature by treatment with the 40% ethanol and 1% *l*-menthol in 40% ethanol solution. **Fig. 2** shows the phase transition temperatures obtained from the thermograms in Fig. 1. These phase transition temperatures were decreased significantly by the treatment with 1% *l*-menthol in 40% ethanol, from 39 °C, 54 °C, and 66 °C to 35 °C, 48 °C, and 58 °C, respectively. By contrast, treatment with 40% ethanol decreased the phase transition temperature insignificantly.

Effects of *l*-menthol on the microviscosity of intercellular lipid in the SC

The ESR spectra of the spin-label reagent 5-DSA in intercellular lipid in the SC are depicted in **Fig. 3**. The spectra of 5-DSA in intercellular lipid in the SC indicated two distinct peaks derived from the *S* and *W* components. The component *S* decreased markedly as a function of temperature, whereas the effect of temperature on the component *W* was modest. As shown in Fig. 3(b), *l*-menthol strongly affected the component *S* in the spectra of 5-DSA. The component *S* was weakened significantly by treatment with *l*-menthol in 40% ethanol. **Fig. 4** shows the τ values calculated from the ESR spectra of 5-DSA in Fig. 3. Treatment with *l*-menthol markedly decreased the flexion point of the τ value of the SC

Fig. 1 DSC thermograms of the hairless rat SC after treatment with *l*-menthol in 40% ethanol. (a) Purified water as a control, (b) 40% ethanol, and (c) 1.0% *l*-menthol in 40% ethanol were applied to the SC for 2 h at 37 °C.

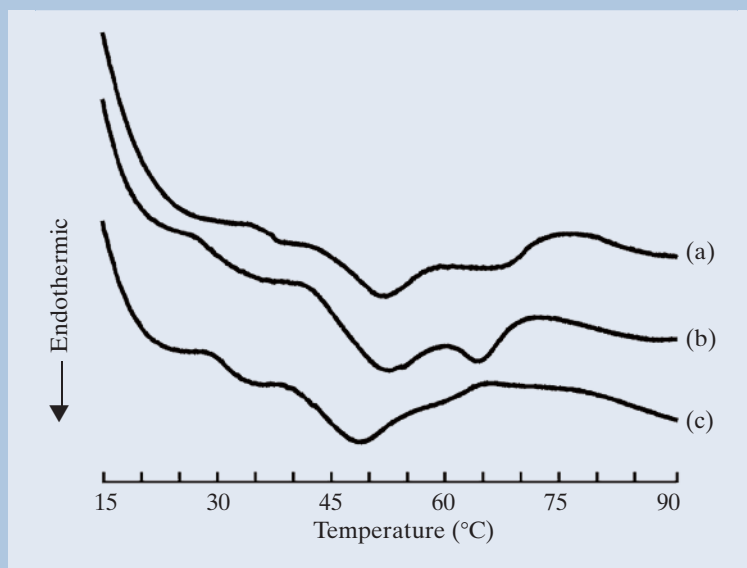


Fig. 2 Changes in the phase transition temperature of the hairless rat SC. The phase transition temperatures were calculated from the DSC curves shown in Fig. 1. Open bars, control, purified water-treated SC; gray bars, 40% ethanol; and black bars, 1.0% *l*-menthol. Ortho, orthorhombic hydrocarbon chain packing; LL, long lamellar structure; SL, short lamellar structure; and H-Hex, high-temperature hexagonal hydrocarbon chain packing. Each column represents the mean \pm S.D. (n=3). * p <0.05 and ** p <0.01 vs. control.

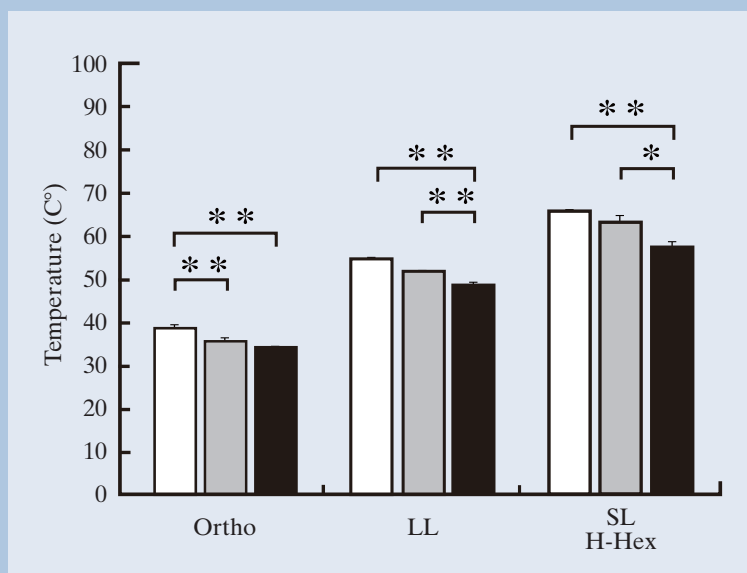


Fig. 3 ESR spectra of 5-DSA in the hairless rat SC after the treatment with *l*-menthol in 40% ethanol. (a) 40% ethanol and (b) 1.0% *l*-menthol in 40% ethanol were applied to the SC for 2 h at 37 °C. The ESR spectra were obtained under thermal control at a rate of about 2.5 °C/min.

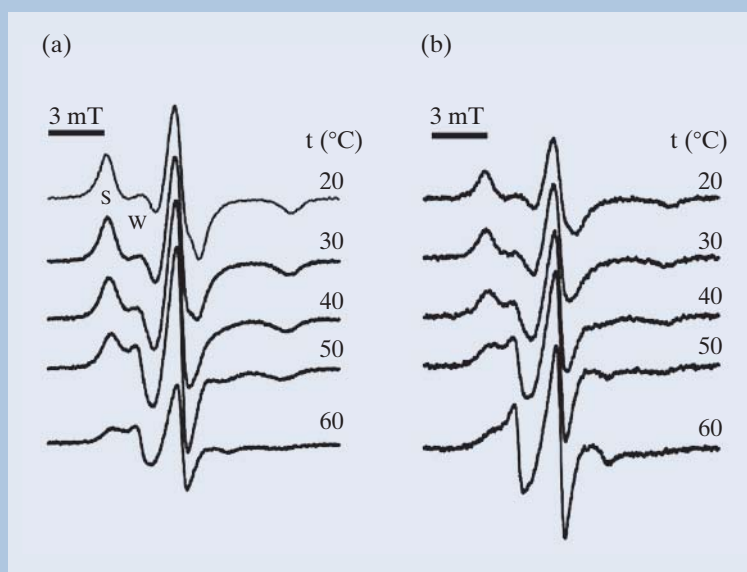


Fig. 4 Effects of *l*-menthol on the fluidity of the hydrophilic region of intercellular lipid in the SC. The rotational correlation times of 5-DSA in the hairless rat SC were calculated from the ESR spectra shown in Fig. 3. (○) Control, 40% ethanol-treated SC and (□) SC treated with 1.0% *l*-menthol in 40% ethanol.

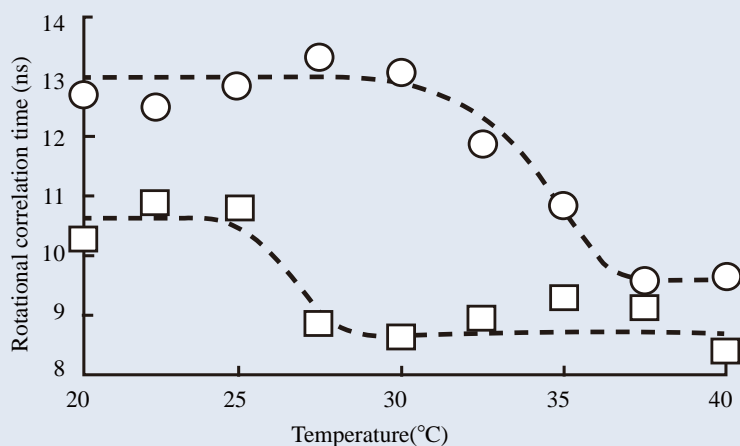


Fig. 5 ESR spectra of 16-DSA in the hairless rat SC after treatment with *l*-menthol in 40% ethanol. (a) 40% ethanol and (b) 1.0% *l*-menthol in 40% ethanol were applied to the SC for 2 h at 37 °C. The ESR spectra were obtained under thermal control at a rate of about 2.5 °C/min.

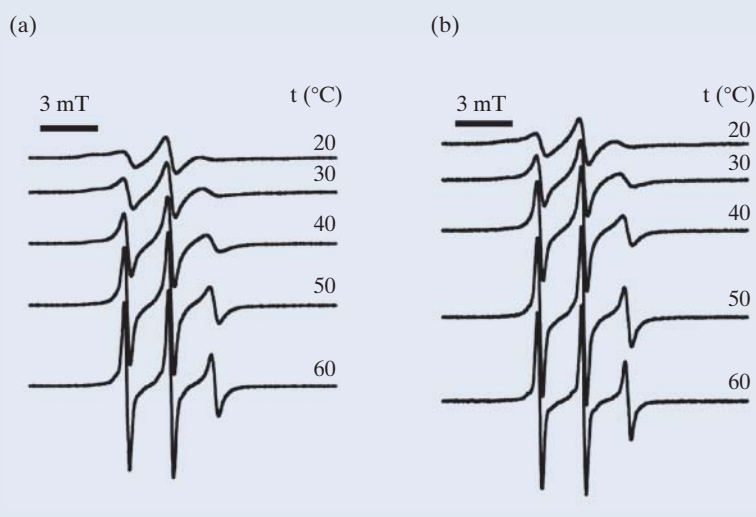
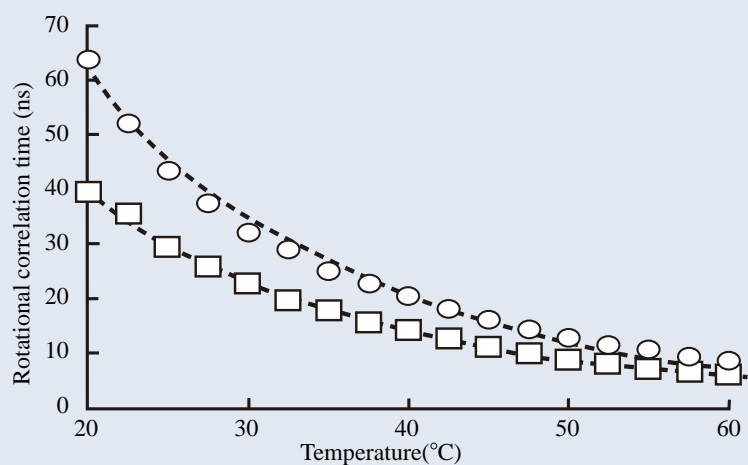


Fig. 6 Effects of *l*-menthol on the fluidity of the hydrophobic region of intercellular lipid in the SC. The rotational correlation times of 16-DSA in the hairless rat SC were calculated from the ESR spectra shown in Fig. 5. (○) Control, 40% ethanol-treated SC and (□) SC treated with 1.0% *l*-menthol in 40% ethanol.



as the temperature decreased from 37.5 °C to 30 °C. The *l*-menthol in 40% ethanol treatment markedly decreased the τ value at room temperature, and the τ value decreased further at lower temperatures.

Figs. 5 and 6 show the effects of *l*-menthol on the ESR spectra and values of the spin-label reagent 16-DSA in intercellular lipid in the hairless rat SC. The ESR spectra of 16-DSA showed isotropic peaks, and these peaks sharpened gradually as a function of temperature. The τ values decreased gradually as the temperature rose from 20 °C to 60 °C. The τ value of 16-DSA was much lower in the 1.0% *l*-menthol-treated SC than in the 40% ethanol-treated SC. With increasing temperature, the τ value converged to that obtained for intercellular lipid in the SC treated with 40% ethanol at 60 °C.

Discussion

The effect of pharmaceutical additives, including transdermal absorption enhancers, on intercellular lipid in the SC is important to the development of effective transdermal drug delivery systems. The interaction between transdermal absorption enhancer molecules and components of intercellular lipid in the SC might be significant. The mechanistic alterations in the microstructure and physicochemical properties of intercellular lipid in the SC may be induced by this interaction. The enhancing effect of the cyclic monoterpenes is related to the lipid fluidity of intercellular lipid in the SC [16, 19]. Therefore, clarifying a drug's permeation route requires the evaluation of the fluidizing effect of the cyclic monoterpenes at the molecular level.

The thermograms of the SC indicated three peaks that were derived from endothermic phase transitions (Fig. 1(a)). Previous results show that these phase transitions reflect changes in intercellular lipid in the SC [23, 24]. A previous study using DSC reported that the phase transition of intercellular lipid in the hairless mouse SC occurred at 39 °C, 51 °C, and 71 °C [23]. The change in

lamellar structure in intercellular lipid is consistent with the phase behavior investigated by synchrotron X-ray scattering in the hairless mouse SC [24]. Intercellular lipid in the SC of the hairless mouse is thought to form a rigid lamellar structure and to comprise hydrocarbon chain packing at temperatures < 39 °C. At 39 °C, the orthorhombic hydrocarbon chain packing disappears and is transposed to high-temperature hexagonal hydrocarbon chain packing at higher temperatures. The disappearance of the long lamellar structure occurred at 51 °C and the structure transferred to a liquid crystalline phase with hexagonal hydrocarbon chain packing. Subsequently, the short lamellar structure melted at 71 °C. It was reported that the thermotropic behavior of the hairless rat SC was similar to that of the hairless mouse [25]. Therefore, the obtained endothermic phase transition at 39 °C represents the disappearance of the orthorhombic hydrocarbon chain packing. Moreover, the phase transitions at 54 °C and 66 °C reflect the phase transitions of long and short lamellar structures, respectively. As shown in Fig. 2, *l*-menthol significantly decreased each phase transition temperature of intercellular lipid in the SC, suggesting that *l*-menthol disturbed and/or fluidized the rigid microstructure of intercellular lipid in the SC. We have previously used synchrotron X-ray scattering to show that *l*-menthol significantly affects the intercellular lipid arrangement of the hairless rat SC [16]. A similar effect was observed in a lipid model system [26]. These reports suggest that the change in intercellular lipid arrangements induced by treatment with *l*-menthol is a crucial factor in its enhancing effect. To correlate these thermotropic behaviors of intercellular lipid in the SC and lipid fluidity, we performed the ESR measurements according to the thermal control.

The spin-label reagents 5- and 16-DSA were used to detect the phase transitions [27, 28]. They reflect only the reorientation motion of the nitroxide radical, which depends greatly on the motional freedom of the alkyl chain to which it is bound (**Fig. 7**). In the case of 5-DSA,

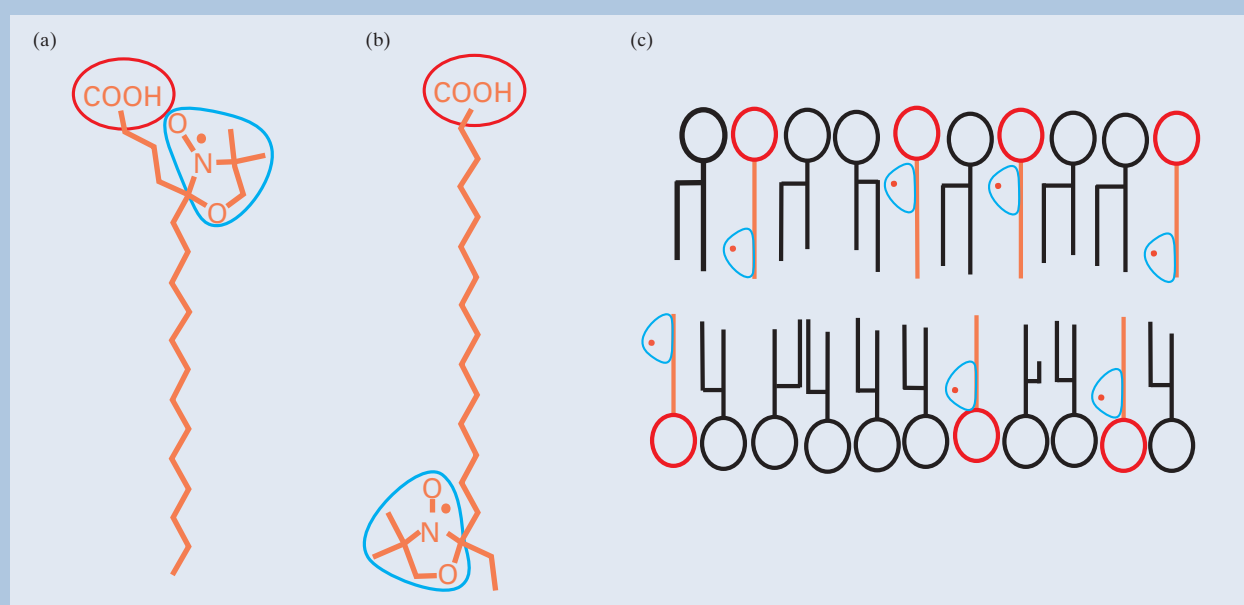


Fig. 7 Chemical structures of 5-doxy stearic acid (5-DSA) (a), 16-doxy stearic acid (16-DSA) (b) and schematic presentation of lipid lamellar in stratum corneum (c).

the doxyl group is located near the carboxyl group, and the nitroxide radical should be accommodated near the head group, which is a polar region of the intercellular lipid lamellar matrix. In 16-DSA, the nitroxide radical is bound to the terminal methylene group, where it reflects the segmental motion of the alkyl chain, a hydrophobic region of the intercellular lipid lamellar matrix. Consequently, the ESR spectra obtained from these spin-label reagents can clarify the effects of *l*-menthol on different regions of intercellular lipid in the SC. The rotational correlation time (τ) is expressed in Eq. (1)[22].

$$\tau = 3.418 \times 10^{-10} \Delta(0) \left[\sqrt{\frac{h(0)}{h(-1)}} - \sqrt{\frac{h(0)}{h(1)}} \right] \dots \dots \dots \text{Eq.(1)}$$

τ is rotational correlation time, $\Delta(0)$ is the peak-to-peak width of the central line in Gauss, $h(m)$ is the peak height of the line belonging to the nuclear quantum number m . τ represents micro viscosity around probes, such as 5- and 16-DSA and also inversely proportional to membrane fluidity.

The τ value of 5-DSA decreased markedly as the temperature increased in 30 °C to 40 °C. This decrease was accompanied by distinct changes in the flexion point, which corresponded to the phase transition of the orthorhombic hydrocarbon chain packing (Fig. 1(a)). This decrease in the τ value of 5-DSA suggested that fluidization of the polar region in the intercellular lamellar was dependent on the phase transition of the orthorhombic hydrocarbon chain packing. Therefore, the polar region of intercellular lipid in the SC was fluidized secondarily by disturbances in the hydrocarbon chain packing. In contrast, the τ value of 16-DSA decreased gradually with increasing temperature, suggesting that the hydrophobic region of intercellular lipid in the SC fluidized gradually as a function of temperature. The conformational state of the hydrocarbon chain in ceramide, the main component of intercellular lipid in the SC, became disordered as a function of temperature. This was accompanied by conformational disorder of the hydrocarbon chain and the transition from the *trans* rotamer to the *gauche* structure, as shown by Raman spectroscopy [29, 30]. This disorganization was accompanied by a loosening of the lateral packing in the hydrocarbon chain packing. This disordering was induced by the loosened hydrogen bond and van der Waals forces of the lipid molecules [31]. These results suggest that the decrease in the τ values of 16-DSA is related to the rotameric transition from the *trans* to the *gauche* structure of the hydrocarbon chain backbone.

l-Menthol reduced the τ values of 5- and 16-DSA in intercellular lipid in the SC at the physiological temperature (Figs. 4 and 6), suggesting that *l*-menthol fluidized the polar and hydrophobic regions of intercellular lipid in the SC. In the experiment with 5-DSA, intercellular lipid in the SC showed a distinct flexion point, and *l*-menthol significantly shifted the flexion point from 35 °C to 27 °C. This flexion point corresponds to the phase transition of the orthorhombic hydrocarbon chain packing of intercellular lipid in the SC. These data suggest that the intermolecular interaction with the orthorhombic hydrocarbon chain packing of intercellular lipid in the SC was weakened by treatment with *l*-menthol at the physical temperature. We suggested previously that *l*-menthol significantly fluidizes the hydrocarbon chain packing

of intercellular lipid in the SC based on our data from synchrotron X-ray scattering [15]. Our current data clarify that the fluidizing effect of *l*-menthol on intercellular lipid in the SC was induced by disturbances in the hydrocarbon chain packing in intercellular lipid model systems comprising ceramide 5, cholesterol, and palmitic acid [26]. These data suggest that fluidization of the polar region of intercellular lipid in the SC was caused by attenuation of the intermolecular interaction of the head groups.

In experiments with the other spin-label reagent, 16-DSA, the τ values were decreased markedly by treatment with *l*-menthol at lower temperatures, suggesting fluidization of the hydrophobic region of intercellular lipid in the SC, which comprises mainly a hydrocarbon backbone of ceramide. *l*-Menthol may affect the rotameric conformation of the hydrocarbon chain of intercellular lipid in the SC by inducing a transition from the *trans* to *gauche* rotamer in the hydrocarbon chains. Another report suggested that *l*-menthol attracts membrane lipids to the center of the membrane, making the interior of the membrane more polar, which would disturb the hydrogen-bonding network in the polar region of intercellular lipid in the SC [30]. Based on their ESR measurement data, Anjos et al. suggested that monoterpenes act mainly at polar head groups where they weaken the inter- and intralamellar hydrogen bonding networks [18]. Therefore, the effect of *l*-menthol on the hydrophobic region might be a subsequent action induced by the disruption of the polar hydrocarbon, hexagonal, and orthorhombic hydrocarbon chain packing. The ESR measurements suggested that the fluidizing effect of *l*-menthol reflects the thermotropic behavior, disturbance of hydrocarbon chain packing, and rotameric disorganization of intercellular lipid in the SC.

Conclusions

ESR is a powerful tool for evaluating the promoting activity of transdermal absorption enhancers and provides insight into the molecular and functional groups in intercellular lipid in the SC. From our results, we concluded that *l*-menthol acts on the polar and hydrophobic regions of intercellular lipid in the SC. A fluidizing effect was induced by changes in the microstructure of intercellular lipid in the SC. The results of this study may provide important knowledge for the development of transdermal formulations.

Acknowledgments

This work was supported by a grant from the Ministry of Education, Culture, Sports, Science and Technology of Japan. We wish to express our gratitude and deepest appreciation to Ms. Yumi Nakai and Dr. Aiko Shimada (JEOL, Tokyo Japan) for their advice and assistance with the ESR measurements.

References

- [1] Elias, P.M., 2005. Stratum corneum defensive functions: an integrated view. *J. Invest. Dermatol.* **125**, 183-200.
- [2] Gray, G.M., Yardly, H.J., 1975. Lipid compositions of cells isolated from pig, human, and rat

- epidermis. *J. Invest. Dermatol.* **16**, 434-440.
- [3] Farwanah, H., Paith, K., Neubert, R.H.H., Wohlrab, J., 2005. Ceramide profiles of the uninvolved skin in atopic dermatitis and psoriasis are comparable to those of healthy skin. *Arch. Dermatol. Res.* **296**, 514-521.
- [4] Masukawa, Y., Narita, H., Sato, H., Naoe, A., Kondo, N., Sugai, Y., Oba, T., Honma, R., Ishikawa, J., Takagi, Y., Kitahara, T., 2009. Comprehensive quantification of ceramide species in human stratum corneum. *J. Lipid Res.* **50**, 1708-1719.
- [5] White, S.H., Mirejocsky, D., King, D.I., 1988. Structure of lamellar lipid domains and corneocyte envelopes of murine stratum corneum. An X-ray diffraction study. *Biochemistry.* **27**, 725-732.
- [6] Bouwstra, J.A., Gooris, D.S., van der Spec, J.A., Lavrijssen, S., Bras, W., 1994. The lipid and protein structure of mouse stratum corneum: a wide and small angle X-ray diffraction study. *Biochem. Biophys. Acta.* **1212**, 183-192.
- [7] Ohta, N., Ban, S., Tanaka, H., Nakata, S., Hatta, I., 2003. Swelling of intercellular lipid lamellar structure with short repeat distance in hairless mouse stratum corneum as studied by X-ray diffraction. *Chem. Phys. Lipids.* **123**, 1-8.
- [8] Charalambopoulou, G.C., Steriotis, T.A., Hauss, T., Stubos, A.K., Kancloupous, N.K., 2004. Structural alterations of fully hydrated human stratum corneum. *Physica B.* e603-e606.
- [9] Bouwstra, J.A., Gooris, G.S., de Vries, M.A.S., van der Spek, J.A., Gras, W., 1992. Structure of human stratum corneum as a function of temperature and hydration: a wide angle X-ray diffraction study. *Int. J. Pharm.* **84**, 205-216.
- [10] Obata, Y., Takayama, K., Maitani, Y., Machida, Y., Nagai, T., 1993. Effect of pretreatment with skin with cyclic monoterpenes on permeation of diclofenac in hairless rat. *Biol. Pharm. Bull.* **16**, 312-314.
- [11] Amit, K.J., Narisatty, S.T., Ramech, P., 2002. Transdermal drug delivery of imipramine hydrochloride. I. Effect of terpenes. *J. Control. Release.* **79**, 93-101.
- [12] Mohammed, A., Abdul, A., Yasumin, S., Asgarm A., 2007. Status of terpenes as skin permeation enhancers. *Drug Discov. Today.* **12**, 1061-1067.
- [13] Obata, Y., Otake, Y., Takayama, K., 2010a. Feasibility of transdermal delivery of prochlorperazine. *Biol. Pharm. Bull.* **33**, 1454-1457.
- [14] Narishetty, S.T.K., Panchagnula, R., 2005. Effect of *l*-menthol and 1,8-cineole on phase behavior and molecular organization of SC lipids and skin permeation of zidovudine. *J. Contr. Rel.* **102**, 59-70.
- [15] Obata, Y., Maruyama, Y., Takayama, K., 2006. The mode of promoting activity of *O*-methylmenthol as a transdermal absorption enhancer. *Pharm. Res.* **23**, 392-400.
- [16] Obata, Y., Utsumi, S., Watanabe, H., Suda, M., Tokudome, Y., Otsuka, M., Takayama, K., 2010b. Infrared spectroscopic study of lipid interaction in stratum corneum treated with transdermal permeation enhancers. *Int. J. Pharm.* **389**, 18-23.
- [17] dos Anjos, J.L.V., Neto, D.S., Alonso, A., 2007. Effect of ethanol/*l*-menthol on the dynamics and partitioning of spin labeled lipids in the stratum corneum. *Eur. J. Pharm. Biopharm.* **67**, 406-412.
- [18] dos Anjos, J.L.V., Alonso, A., 2008. Terpenes increase the partitioning and molecular dynamics of an amphipathic spin label in stratum corneum membranes. *Int. J. Pharm.* **350**, 103-112.
- [19] Alonso, A., Meirelles, N.C., Tabak, M., 2000. Lipid chain dynamics in stratum corneum studies by spin label electron paramagnetic resonance. *Chem. Phys. Lipids.* **104**, 101-111.
- [20] Couto, S.G., Oliveira, M.S., Alonso, A., 2005. Dynamics of proteins and lipids in the stratum corneum: effects of percutaneous permeation enhancers. *Biochim. Biophys. Acta.* **1237**, 6-15.
- [21] Queiros, W.P., Neto, D.S., Alonso, A., 2005. Dynamics and partitioning of spin-labeled stearates into the lipid domain of stratum corneum. *J. Control. Release.* **106**, 374-385.
- [22] Hemminga, M.A., 1975. An ESR spinlabel study of structural and dynamical properties of oriented lecithin-cholesterol multibilayers. *Chem. Phys. Lipids.* **14**, 151-173.
- [23] Hatta, I., Nakanishi, K., Ishikawa, K., 2005. Thermal analysis of stratum corneum of hairless mouse with attention to phase transition to phase near 35 °C. *Thermochim. Acta.* **431**, 94-97.
- [24] Hatta, I., Ohta, N., Inoue, K., Yagi, N., 2006. Coexistence of two domains in intercellular lipid matrix of stratum corneum. *Biochem. Biophys. Acta.* **1758**, 275-279.
- [25] Al-Saidan, S.M., Krishnaiah, Y.S., Chandrasekhar, D.V., Lalla, J.K., Rama, B., Jayaram, B., Bhaskar, P., 2004. Formulation of an HPMC gel drug reservoir system with ethanol-water as a solvent system and limonene as a penetration enhancer for enhancing in vitro transdermal delivery of micorandil. *Skin Pharmacol. Physiol.* **17**, 310-320.
- [26] Watanabe, H., Obata, Y., Onuki, Y., Ishida, K., Takayama, K., 2010. Difference effects of *l*- and *d*-menthol on the ceramide 5/cholesterol/palmitic acid bilayers. *Int. J. Pharm.* **402**, 146-152.
- [27] Shinshick, E.J., McConnell, H.M., 1973. Lateral phase separation in binary mixtures of cholesterol and phospholipids. *Biochem. Biophys. Res. Comm.* **53**, 446-451.
- [28] Alaouie, A.M., Smirnov, A.I., 2006. Ultra-stable temperature control in EPR experiments: thermodynamics of gel-to-liquid phase transition in spin-labeled phospholipid bilayers and bilayer perturbations by spin labels. *J. Magn. Reson.* **182**, 299-238.
- [29] Tfayli, A., Guillard, E., Manfait, M., Baillet-Guffroy, A., 2010. Thermal dependence of Raman descriptors of ceramides. Part I: effect of double bonds in hydrocarbon chains. *Anal. Bioanal. Chem.* **397**, 1281-1296.
- [30] Guillard, E., Tfayli, A., Manfait, M., Baillet-Guffroy, A., 2010. Thermal dependence of Raman descriptors of ceramides. Part II: effect of chains lengths and head group structures. *Anal. Bioanal. Chem.* **399**, 1201-1213.
- [31] Lawson, E.E., Anigbogu, A.N., Williams, A.C., Barry, B.W., Edwards, H.G., 1998. Thermally induced molecular disorder in human stratum corneum lipids compared with model phospholipid system: FT-Raman spectroscopy. *Spectrochim. Acta Mol. Biomol. Spectrosc.* **54A**, 543-558.

Introduction of New Products

Electron Microscope

JEM-1400Plus

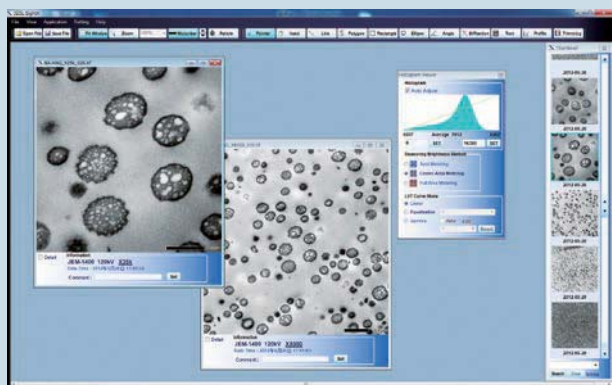
The JEM-1400Plus is a versatile transmission electron microscope (TEM) for a wide range of applications including biology, polymers, nano technology, and advanced materials. It brings a simple operating environment optimized for users' research purpose.

Point resolution : 0.2 nm
Accelerating voltage : 40 to 120 kV
Magnification : $\times 10$ to 1,200,000



Features

- New operation panel and touch panel screen for simple, intuitive operation
- Multi pixel camera (8M pixels) fully integrated in TEM
- SightX Viewer - a software designed to view/edit acquired images on your PC
- Many auto functions - Auto focus, Auto Exposure, and Auto Montage
- Ultra Low MAG mode ($\times 10$) to view grid images for sample navigation



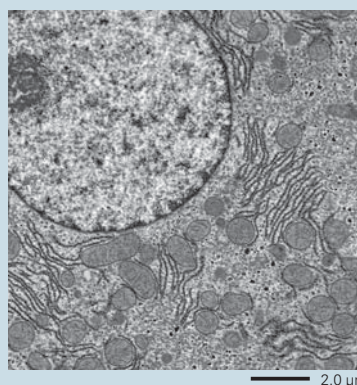
SightX Viewer Remote viewer software

Other functions

- Point & Shoot
- Image accumulation with drift correction
- Metrology tool
- Image file display using thumbnails

A single camera for view area search to data acquisition

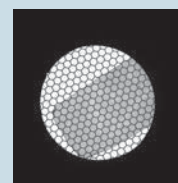
The JEM-1400Plus, featuring a lowest magnification of $\times 10$, uses a single camera for imaging for the entire magnification range from the Ultra Low MAG mode ($\times 10$) to the MAG mode ($\times 1,200,000$). You need not switch cameras for view area search. Auto Montage (standard function) allows you to quickly acquire high quality wide area images. The JEOL CCD camera is available in 1M and 8M pixels.



CCD camera image at $\times 10$

Specimen :
Rat hepatic cells (at 120 kV)

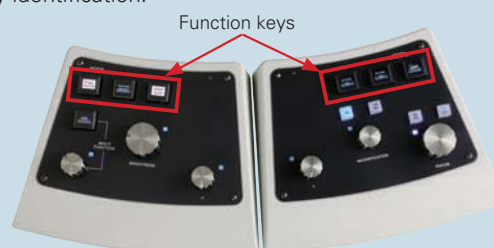
Specimen courtesy of :
Dr. Yoshinori Muranaka,
Hamamatsu University
School of Medicine



CCD camera image (2k \times 2k)

Simple panels

New operation panels feature a simple design. You can assign or edit functions to the organic EL buttons on the panels. The assigned functions emerge on the buttons for easy identification.



Field Emission Scanning Electron Microscope **JSM-7610F**

JSM-7610F is an ultra high resolution Schottky Field Emission Scanning Electron Microscope which has semi-in-lens objective lens.

High power optics can provide high throughput and high performance analysis.

It's also suitable for high spatial resolution analysis.

Furthermore, Gentle Beam mode can reduce the incident electron penetration to the specimen, enabling you to observe its topmost surface by using a few hundred landing energy.

Resolution : 1.0 nm (15 kV), 1.5 nm (1 kV, GB mode)

During analysis 3.0 nm

(15 kV, WD 8 mm, probe current 5 nA)

Accelerating voltage : 0.1 to 30 kV

Magnification : × 25 to 1,000,000



High resolution imaging and high performance analysis by semi-in-lens objective lens

The JSM-7610F combines two proven technologies – an electron column with semi-in-lens objective lens which can provide high resolution imaging by low accelerating voltage and an in-lens Schottky FEG which can provide stable large range of probe currents for all applications (A few pA to more than 200 nA).

The in-lens Schottky FEG is a combination of a Schottky FEG and the first condenser lens and is designed to collect the electrons from the emitter efficiently.

Then the emitter life is extremely long and its warranty period is 3 years.

The topmost surface imaging at low accelerating voltage by Gentle Beam mode (GB)

The Gentle Beam (GB) mode applies a negative voltage to a specimen and decelerates incident electrons just before they irradiate the specimen, thus the resolution is improved at an extremely low accelerating voltage.

Therefore, 7610F is possible to observe a topmost surface by a few hundred eV which were difficult to observe conventionally and nonconductive samples such as ceramics and semiconductor etc.

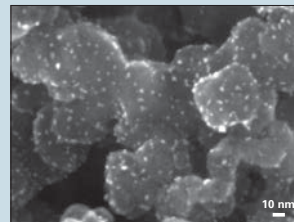
High throughput and high performance analysis by High Power Optics

The High Power Optics produces fine electron probe for both observation and analysis.

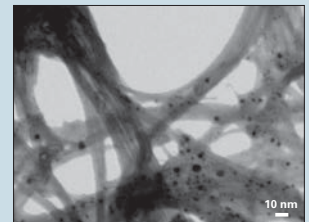
The aperture angle control lens maintains a small probe diameter even at a larger probe current.

Using both techniques, the 7610F is suitable for a wide variety of analysis with EDS, WDS, CL etc.

High spatial resolution analysis by semi-in-lens objective lens

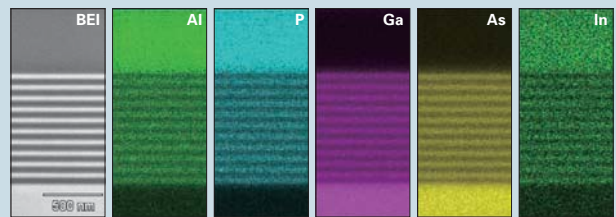


Sample: Pt Catalyst
Accelerating Voltage 15 kV



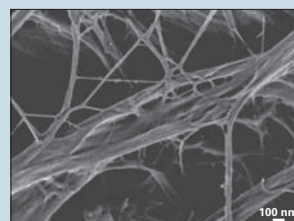
Sample: Carbon Nanotubes
Accelerating Voltage 30 kV

High spatial resolution analysis by semi-in-lens objective lens

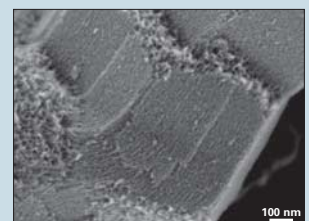


LED cross section (EDS analysis of multilayers below 100 nm)

The topmost surface imaging at ultra low landing energy by Gentle Beam mode (GB)



Sample: filter
Landing energy 500 eV



Sample: Mesoporous Silica
Landing energy 800 eV

Introduction of New Products

Linked Optical & Scanning electron microscope system

miXcroscopy

The same specimen holder can now be used for both the optical microscope and the scanning electron microscope. As a result, by managing the stage information with dedicated software, it is possible for the system to record the locations observed with the optical microscope, and then further magnify the same areas with the scanning electron microscope to observe the fine structures. The observation targets found with the optical microscope can be seamlessly observed with the scanning electron microscope without having to search for the target again. It is now possible to smoothly and easily compare and verify the optical microscope images and scanning electron microscope images.

Features

- Compatible Optical microscope: ECLIPSE LV-N series by Nikon Corporation
- Compatible Scanning electron microscope: JSM-7800F, JSM-7610F, etc. by JEOL Ltd.
- Optical/ Electron microscope linkage software
- Optical/ Electron microscope shared specimen holder
- Observation functions/ Optical microscope: Bright field, Dark field
- Differential interference, Simple polarization, Epifluorescence
- Observation functions/ Electron microscope: Secondary electron images, Backscattered electron images

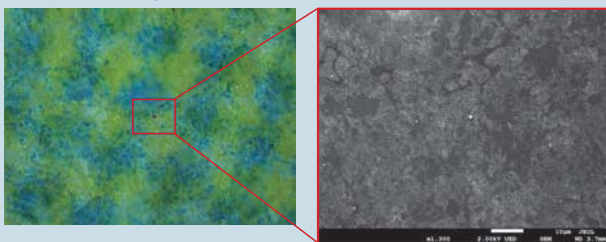


Optical microscope



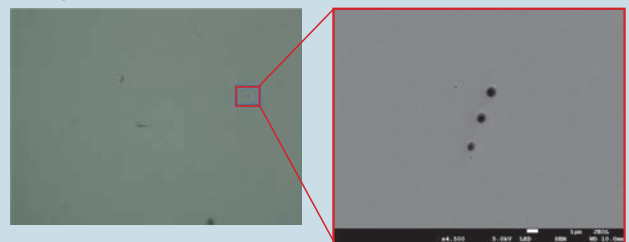
Scanning e lectttrron miicroscope

Pinpoint, high-resolution observation & analysis of the target site



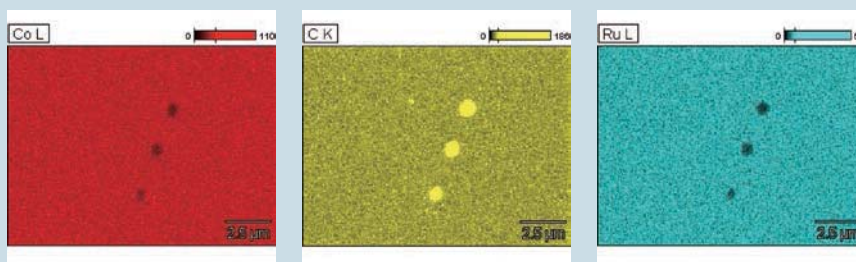
Laser printer printing surface (optical image)

Laser printer printing surface (secondary electron image)



Hard disk (optical image)

Hard disk (secondary electron image)



Hard disk (EDS element map)



50 Year Anniversary 1963 - 2013

It has been 50 years since the first issue of JEOL NEWS was released in 1963. We would like to thank everyone for their support in reaching this milestone.



Certain products in this brochure are controlled under the "Foreign Exchange and Foreign Trade Law" of Japan in compliance with international security export control. JEOL Ltd. must provide the Japanese Government with "End-user's Statement of Assurance" and "End-use Certificate" in order to obtain the export license needed for export from Japan. If the product to be exported is in this category, the end user will be asked to fill in these certificate forms.

JEOL JEOL Ltd.

1-2 Musashino 3-chome Akishima Tokyo 196-8558 Japan Sales Division Telephone:+81-42-528-3381 Facsimile:+81-42-528-3386

<http://www.jeol.com/>

ARGENTINA
COASIN S.A.C.I.yF.
Virrey del Pino 4071,
1430 Buenos Aires
Argentina
Tel. 54-11-4552-3185
Fax. 54-11-4555-3321

AUSTRALIA & NEW ZEALAND
JEOL(AUSTRALASIA) Pty.Ltd.
Suite 1, L2 18 Aquatic Drive
- Frenchs Forest NSW 2086
Australia
Tel. 61-2-9451-3855
Fax. 61-2-9451-3822

AUSTRIA
JEOL (GERMANY) GmbH
Oskar-Von-Miller-Strasse 1a, 85386
Eching, Germany
Tel. 49-8165-77346
Fax. 49-8165-77512

BANGLADESH
A.O. CHOWDHURY SCIENCE & SYNERGY PVT. LTD.
87, Suhrawardy Avenue, Floor 2
Baridhara, Dhaka1212
Bangladesh
Tel. 8802-9862272, 8953450, 8953501
Fax. 8802-9864428

BELGIUM
JEOL (EUROPE) B.V.
Planet II, Gebouw B
Louvainssesteenweg 542,
B-1830 Zaventem
Belgium
Tel.32-2-720-0560
Fax.32-2-720-6134

BRAZIL
JEOL Brasil Instrumentos Cientificos Ltda.
Av. Jabaquara, 2958-5*andar-cj, 52
04046-500 Sao Paulo, SP
Brazil
Tel. 55-11-5070 4000
Fax. 55-11-5070 4010

CANADA
JEOL CANADA, INC.
3275 Premier Rue #8,
St-Hubert, Quebec J3Y 8Y6, Canada
Tel. 1-450-676-8776
Fax. 1-450-676-6694

CHILE
ARQUIMED INNOVATION
Arturo Prat 828,
Santiago, Chile
Tel. 56-2-634-6266
Fax. 56-2-634-4633

CHINA
JEOL(BEIJING) CO., LTD.
Room B1010/1110, Wantong New World Plaza No. 2
Fuchengmenwai Street, Xicheng District,
Beijing 100037, P.R.China
Tel. 86-10-6804-6321
Fax. 86-10-6804-6324

JEOL (BEIJING) CO., LTD., SHANGHAI BRANCH
Room 1505/1506, Nol 300Xi Kang Road,
Jing an Dist., Shanghai, 200040, China
Tel. 86-21-6249-4883/4487/4537/4404
Fax. 86-21-6248-4075

JEOL (BEIJING) CO., LTD., GUANG ZHOU BRANCH
N1601, World Trade Center Building,
#371-375, Huan Shi Road East, Guang Zhou,
Guangdong Prov., 510095, P.R.China
Tel. 86-20-8778-7848
Fax. 86-20-8778-4268

JEOL (BEIJING) CO., LTD., WUHAN BRANCH
Room A2118, Zhongshang Plaza Office Bldg.,
No. 7 Zhongnan Road, Wuhan,
Hubei, 430071, P.R.China
Tel. 86-27-8713-2567
Fax. 86-27-8713-2567

JEOL LTD., (BEIJING) CO., LTD., CHENGDU BRANCH
1807A Zongfu Building,
NO. 35 Zhongtu Road, Chengdu, Sichuan, 610016
P.R. China
Tel. 86-28-86622554
Fax. 86-28-86622564

EGYPT
JEOL SERVICE BUREAU
3rd Fl. Nile Center Bldg., Nawal Street,
Dokki, (Cairo), Egypt
Tel. 20-2-3335-7220
Fax. 20-2-3339-4186

FRANCE
JEOL (EUROPE) SAS
Espace Claude Monet, 1 Allée de Giverny
78290, Croissy-sur-Seine, France
Tel. 33-13015-3737
Fax. 33-13015-3747

GERMANY
JEOL (GERMANY) GmbH
Oskar-Von-Miller-Strasse 1a, 85386
Eching, Germany
Tel. 49-8165-77346
Fax. 49-8165-77512

GREAT BRITAIN & IRELAND
JEOL (U.K.) LTD.
JEOL House, Silver Court, Watchmead,
Welwyn Garden City, Herts AL7 1LT, U.K.
Tel. 44-1707-377117
Fax. 44-1707-373254

GREECE
N. ASTERIAS S.A.
56-58,S. Trikoupi Str. P.O. Box 26140
GR-10022, Athens, Greece
Tel. 30-1-823-5383
Fax. 30-1-823-9567

HONG KONG
FARMING LTD.
Unit No. 1009, 10/F., Prosperity
663 King's Road, North Point, Hong Kong
Tel. 852-2815-7299
Fax. 852-2581-4635

INDIA
JEOL INDIA Pvt. Ltd.
Elegance Tower, Level 2, 212B
Old Mathura Road, Jasola Business District Centre,
Near Apollo Hospital Jasola,
New Delhi 110 025, India
Tel. 91-11-6472-2579
Fax. 91-11-4060-1235

JEOL India Pvt. Ltd. Mumbai Branch
Regus Mumbai
Levels Ground & 1, Trade Centre Bandra Kurla Complex 1108,
Bandra (E) Mumbai, 400051, India
Tel. +91-22-40700700

INDONESIA
PT. TEKNOABindo Penta Perkasa
Komplek Gading Bukit Indah Blok I/11
Jl. Bukit Gading Raya Kelapa Gading Permai,
Jakarta 14240, Indonesia
Tel. 62-21-45847057/58
Fax. 62-21-45842729

ITALY
JEOL (ITALIA) S.p.A.
Centro Direzionale Green Office
Via dei Tulipani, 1
20030 Pieve Emanuele(MI) Italy
Tel. 39-02-9041431
Fax. 39-02-90414343

KOREA
JEOL KOREA LTD.
Dongwoo Bldg. 7F, 1443, Yangjae Daero,
Gangdong-Gu, Seoul, 134-010, Korea
Tel. 82-2-511-5501
Fax. 82-2-511-2635

KUWAIT
Ashraf & CO. Ltd.
P.O.Box 3555 Safat 13036, Kuwait
Tel. 965-1805151
Fax. 965-24335373

MALAYSIA
JEOL(MALAYSIA) SDN.BHD.
508, Block A, Level 5,
Kelana Business Center,
97, Jalan SS 7/2, Kelana Jaya,
47301 Petaling Jaya, Selangor, Malaysia
Tel. 60-3-7492-7722
Fax. 60-3-7492-7723

MEXICO
JEOL DE MEXICO S.A. DE C.V.
Arkansas 11 Piso 2
Colonia Napoles
Delegacion Benito Juarez, C.P. 03810
Mexico D.F., Mexico
Tel. 52-55-211-4511
Fax. 52-55-211-0720

PAKISTAN (Karachi)
ANALYTICAL MEASURING SYSTEM (PVT) LTD.(AMS LTD.)
14-C Main Sehar Commercial Avenue Lane 4,
Khayaban-e-Sehar,
D.H.A-VII, Karachi-75500, Pakistan
Tel. 92-21-35345531/35340747
Fax. 92-21-35345582

PANAMA
PROMED S.A.
Parque Industrial Costa del Este
Urbanizacion Costa del Este
Apartado 0816-01755, Panama, Panama
Tel. 507-3003-3100
Fax. 507-3003-3115

PHILIPPINES
PHILAB INDUSTRIES INC.
7487 Bagtikan Street, SAV Makati,
1203 Metro, Manila Philippines
Tel. 63-2-896-6653
Fax. 63-2-897-7732

PORTUGAL
Izasa Portugal Lda.
R. do Proletariado, 1
2790-138 CARMAXIDE, Portugal
Tel. 351-21-424-73-00
Fax. 351-21-418-60-20

RUSSIA
JEOL (RUS) LLC.
Krasnoprolétaireskaya Street, 16,
Bld. 2, 127473, Moscow,
Russian Federation
Tel. 7-495-748-7791/7792
Fax. 7-495-748-7793

SAUDI ARABIA
ABDULREHMAN ALGOSAIBI G.T.C. (Riyadh)
Algoasabi Building-Old Airport Road
P.O. Box 215, Riyadh-11411, Saudi Arabia
Tel. 966-1-477-7932

SCANDINAVIA
SWEDEN
JEOL (Skandinaviska)AB:
Hammarbacken 6A, Box 716, 191 27 Sollentuna
Sweden
Tel. 46-8-28-2800
Fax. 46-8-29-1647

SERVICE & INFORMATION OFFICE
NORWAY
JEOL (Skandinaviska)AB:
Lorensvangen 23, 0580 Oslo, NORWAY
Tel. 47-2-2-64-7930
Fax. 47-2-2-65-0619

FINLAND
JEOL (Skandinaviska)AB:
Ylakaupinkuja 2, FIN-02360 Espoo, Finland
Tel. 358-9-8129-0350
Fax. 358-9-8129-0351

SINGAPORE
2 Corporation Road
#01-12 Corporation Place
Singapore 618494
Tel. 65-6565-9989
Fax. 65-6565-7552

SOUTH AFRICA
ADI Scientific (Pty) Ltd.
370 Angus Crescent,
Northlands Business Park, 29 Newmarket Road
Northriding, Randburg, Republic of South Africa
Tel. 27-11-462-1363
Fax. 27-11-462-1466

SPAIN
IZASA, S.A.
Argoneses, 18, 28100 Alcobendas,
(Poligono Industrial), Madrid, Spain
Tel. 34-91-663-0500
Fax. 34-91-663-0545

SWITZERLAND
JEOL (GERMANY) GmbH
Oskar-Von-Miller Strasse 1,
85386 Eching, Germany
Tel. 49-8165-77346
Fax. 49-8165-77512

TAIWAN
JIE DONG CO., LTD.
7F, 112, Chung Hsiao East Road,
Section 1, Taipei, Taiwan 10023
Republic of China
Tel. 886-2-2395-2978
Fax. 886-2-2322-4655

For NMR & Mass Spectrometer Products
Widerton Technologies Corp.
No.8-2, No.77, Sec.2, Zhonghua E Rd.,
East Dist., Tainan City 701, Taiwan(R.O.C.)
Tel. 886-6-289-1943
Fax. 886-6-289-1743

(For Mass Spectrometer Products)
Tech Max Technical Co., Ltd.
5F, No.11, Wuquan 2nd Rd., Wugu Dist.,
New Taipei City 248, Taiwan (R.O.C.)
Tel. 886-3-8990-1779
Fax. 886-2-8990-2559

For Semiconductor Products:
JEOL TAIWAN SEMICONDUCTORS LTD.
11F-1, No. 346, Pei-Da Road, Hsin-Chu City 300,
Taiwan, Republic of China
Tel. 886-3-523-8490
Fax. 886-3-523-8503

THAILAND
BECTHAI BANGKOK EQUIPMENT & CHEMICAL CO., Ltd.
300 Phaholyothin Rd. Phayathai, Bangkok 10400,
Thailand
Tel. 66-2-615-2929
Fax. 66-2-615-2350/2351

JEOL ASEAN TECHNICAL CENTER (JATC)
MTEC building room 533
114 Moo9, Thailand Science Park
Paholyothin Rd., Klong 1, Klong Luang,
Pathumthani 12120
THAILAND
Tel. 66-2-564-7738
Fax. 66-2-564-7739

THE NETHERLANDS
JEOL (EUROPE) B.V.
Lireweg 4, NL-2153 PH Nieuw-Vennep,
The Netherlands
Tel. 31-252-823500
Fax. 31-252-823501

TURKEY
TEKSER A.S.
Kaysisdagi, Inonu Mah.Kartal Cad. No:55/3
34755 Alieshir / Istanbul, Turkey
Tel. 90-216-5736470
Fax. 90-216-5736475

UAE
MPS Group Dubai
P.O.Box: 171612,
Rashid Abdulla Al Noami Building
Suite No: 306, Damascus Street,
Al Qusaib-3, Dubai, U.A.E.
Tel. 971-4-2581141
Fax. 971-4-2581151

Gulf Bio Analytical LLC
Office No.902, Sapphire Tower,
Al Itthad Road, Near DNATA Building,
Deira Dubai, UAE
(P.O.Box 28832)
Tel. 971-4250-7300
Fax. 971-4250-7400

JEOL Gulf
c/o Gulf Bio Analytical LLC
Office No.902, Sapphire Tower,
Al Itthad Road, Near Dnata Building,
Deira Dubai, UAE
(P.O.Box 28832)
Tel. 971-4-2579228
Fax. 971-4-2579448

USA
JEOL USA, INC.
11 Dearborn Road, Peabody, MA 01960, U.S.A.
Tel. 1-978-535-5900
Fax. 1-978-536-2205/2206

JEOL USA, INC. WEST OFFICE
5683 Stoneridge Drive Suite #110
Pleasanton, CA 94588, U.S.A.
Tel. 1-925-737-1740
Fax. 1-925-737-1749

VENEZUELA
GOMSA Service and Supply C.A.
Urbanizacion Montalban III
- Residencias Don Andres - Piso 7 - Apartamento 7
Avenida 3, entre calles 7 y 6
Montalban, Caracas, Venezuela
Tel. 58-212-443-4342
Fax. 58-212-443-4342

VIETNAM
TECHNICAL MATERIALS AND RESOURCES
IMPORT-EXPORT JOINT STOCK COMPANY(REXCO)
Hanoi Branch,
No. 13-Lot 12 Truong Yen, Truong Hoa Street,
Gau Giay Dist., Hanoi, Vietnam
Tel. 84-43-562-0516
Fax. 84-43-853-2511